Alma Mater Studiorum · Università di Bologna

Scuola di Scienze

Dipartimento di Fisica e Astronomia

Corso di Laurea Magistrale in Fisica

Study of the $f_0(980)$ resonance production in pp collisions at $\sqrt{s} = 5.02$ TeV with ALICE at the LHC

Supervisor:

Prof. Luisa Cifarelli

Author:

Alessandra Lorenzo

Co-supervisor:

Dr. Francesca Bellini

Academic Year 2016/17

Abstract

Lo scopo della tesi è di effettuare uno studio preliminare sulla produzione di $f_0(980) \rightarrow \pi^+\pi^-$ in collisioni protone-protone ad energia al centro di massa $\sqrt{s} = 5.02$ TeV. I dati utilizzati sono stati raccolti dall'esperimento ALICE durante il Run 2 dell'LHC. L'estrazione del segnale di $f_0(980)$ si è rivelata essere particolarmente complessa a causa del fondo derivante dalle coppie $\pi^+\pi^-$ correlate ma soprattutto dalla sovrapposizione di diverse risonanze nella regione di massa invariante di interesse. L'analisi presentata si concentra sulla strategia seguita per l'estrazione del segnale e sulle procedure di fit utilizzate. I risultati della produzione di $f_0(980)$ sono presentati in funzione dell'impulso trasverso. La natura di $f_0(980)$ rimane ancora elusiva, oltre all'interpretazione ordinaria come mesone ($q\bar{q}$), $f_0(980)$ è stata identificata da alcuni autori come candidato tetraquark o come molecola $K\bar{K}$. Studi in diversi sistemi collisione sono particolarmente interessanti perché possono fornire indicazioni sulla natura di questa particella.

Contents

Introduction

The extremely high energy density reached at the LHC in heavy-ion collisions is such to cause a phase transition towards a state of the deconfined matter predicted on the basis of thermodynamical considerations and QCD calculations: the Quark Gluon Plasma (QGP), a hot and dense state of strongly-interacting matter where quarks and gluons are free. The cooling of the system generates a second phase transition from the QGP to a strongly interacting hadron gas which undergoes rapid expansion, resulting in further cooling down. When inelastic interactions cease, namely at the chemical freeze-out, ratios between particles are fixed, even if they continue to interact elastically or pseudo-elastically. After the kinetic freeze-out also elastic processes stop: particles reach the detectors where they can be identified. Short-lived hadronic resonances are useful probes for the investigation of the late hadronic phase of ultra-relativistic heavy-ion collisions since their lifetimes are of the same order of magnitude as the time span between the chemical and kinetic freeze-out, typically estimated to be about 10 fm/c for central collisions. Recent results by the ALICE Collaboration have shown that the production of resonances with short lifetime, as the K^* (4.5 fm/c), are strongly suppressed in central Pb-Pb collisions, contrary to longer lived particles such as the ϕ-meson ($\tau \sim 45$ fm/c) that leaves the fireball almost unaffected.

The primary goal of this work will be the study of the mesonic resonance $f_0(980) \rightarrow \pi^+\pi^-$ in terms of its production at mid-rapidity ($|y| < 0.5$). The $f_0(980)$ resonance is interesting because due to its large width, thus short lifetime, it is expected to decay during the hadronic phase and can therefore be used as a probe. Furthermore, it has a similar mass as K^* and ϕ but different quark composition, thus its production, if compared to the K^*

and ϕ, might give new insight on the particle production mechanisms. The analysis presented in this thesis has been performed based on a dataset of minimum bias pp collisions at the centre-of-mass energy $\sqrt{s} = 5.02$ TeV, with the ALICE detector at the LHC. The main challenge of this measurement comes from the complexity of the signal extraction procedure due to the large background from correlated $\pi^+\pi^-$ pairs from other resonance decays in the invariant mass window under study, as well as due to the combinatorics from uncorrelated pairs. This analysis provides a feasibility study for the measurement of the $f_0(980)$ production. It has to be noted that the nature of this particle remains elusive. Different interpretation of this resonance including $q\bar{q}$ states, bound states of hadrons such as $K\bar{K}$, and as tetraquark candidate are available. The analysis would also consitute a reference for the measurement in high-multiplicity events (p-Pb, Pb-Pb) as studies in different collision systems are particularly interesting because they can provide information about the nature of this particle.

The aim of the first chapter is to give an overview on the basics of the QGP physics, summarising the main observables from which it is possible to characterise the QGP and the QGP-like effects in small systems. The second chapter is intended as a review of the ALICE experiment, the detector design and the analysis substructure are presented. The third chapter represents the physics motivation of this thesis. More specifically it is dedicated to the discussion of the $f_0(980)$ nature. Both theoretical and experimental aspects are included. The fourth chapter illustrates the study on the f_0 production through the decay channel $\pi^+\pi^-$. The signal extraction is discussed in detail, then the fitting procedure is presented. The raw yields are extracted with an invariant mass analysis and then corrected for the reconstruction efficiency and for detector acceptance. A study of the systematic effects affecting the $f_0(980)$ measurement is presented in the fifth chapter, where the results in terms of p_{T}-dependent and p_{T}-integrated production yield are provided.

Chapter 1

QCD matter at extreme conditions

Soon after the discovery of the atomic nucleus, at the beginning of the 20th Century, the strong interaction has been introduced: the existence of a binding force holding together the nucleons was postulated to ensure nucleus stability. Thanks to deep inelastic scattering experiments much about nuclei structure and properties of strong interaction has been discovered and clarified, but the investigation of dense nuclear matter under extreme conditions is still one of the major research topics of high energy physics.

1.1 QCD: a brief overview

Quantum Chromodynamics (QCD) is the theory of the strong interaction. In the Standard Model, it describes the interaction between quarks using the $SU(3)$ non-Abelian gauge theory of color charge [1]. As a consequence of the non-Abelian nature of the theory, interactions between gauge bosons are permitted. Quarks are characterized not only by spin and electromagnetic charge, but also by a color charge (also carried by gluons) which comes in three varieties usually identified as *red* (r), *green* (g) and *blue* (b). Similarly to the QED case, in which we have positive and negative charge, in QCD anti-quarks have their corresponding anti-colours: *cyan* ($\bar{r}$), *magenta* ($\bar{g}$) and *yellow* ($\bar{b}$) [2].

The Lagrangian density of QCD is given by [3, 4]:

$$\mathscr{L}_{QCD} = \bar{\psi}^i (i\gamma^\mu)(D_\mu)_{ij}\psi^j - m\bar{\psi}^i\psi_i - \frac{1}{4}F^a_{\mu\nu}F^{a\mu\nu} \tag{1.1}$$

where ψ^i represents a quark field with colour index i. Note that the degrees of freedom of the theory are the 3×6 quark fermionic fields: ψ represents, for each flavour, a vector $(\psi_{red};\ \psi_{green};\ \psi_{blue})$ of fermionic fields. γ^μ is a Dirac matrix that expresses the vector nature of the strong interaction (μ is a Lorentz vector index), m is the mass, $F^a_{\mu\nu}$ is the gluon field strenght tensor for a gluon with colour index from $a = 1$ to $a = 8$. D_μ is the covariant derivative in QCD,

$$(D_\mu)_{ij} = \delta_{ij}\partial_\mu - ig_s t^a_{ij} A^a_\mu, \tag{1.2}$$

with g_s the strong coupling. Usually, the strong coupling *constant* is indicated (and calculated) as $\alpha_s = \dfrac{g_s^2}{4\pi}$. A^a_μ is the gluon field with colour index a and t^a_{ij} is proportional to the traceless Hermitian Gell-Mann matrices generators for $SU(3)$. Conventionally, the constant of proportionality is taken to be

$$t^a_{ij} = \frac{1}{2}\lambda^a_{ij} \tag{1.3}$$

where λ^a_{ij} are the Gell-Mann matrices. In Figure 1.1 an example of a quark-gluon interaction is reported.

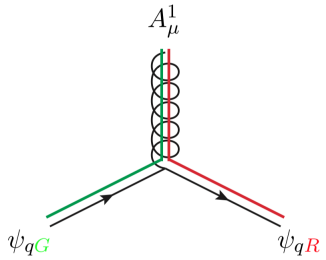

$$\propto\ -\tfrac{i}{2}g_s \quad \bar{\psi}_{qR} \quad \lambda^1 \quad \psi_{qG}$$

$$=\ -\tfrac{i}{2}g_s \quad \begin{pmatrix} 1 & 0 & 0 \end{pmatrix} \quad \begin{pmatrix} 0 & 1 & 0 \\ 1 & 0 & 0 \\ 0 & 0 & 0 \end{pmatrix} \quad \begin{pmatrix} 0 \\ 1 \\ 0 \end{pmatrix}$$

Figure 1.1: Example of qqg vertex in QCD before summing over colours: the two quarks in the states ψ_R and ψ_G interact with a gluon represented by λ^1 [4].

In QED, the intensity of the electromagnetic interaction is given by the QED coupling constant: at small values of transverse momentum, Q^2, it is given by the fine-structure constant $\alpha \approx 1/137$, while at larger values of Q^2 it only increases weakly because of the vacuum polarization. In QCD, the dependence of α_s on Q^2 is given by

$$\alpha_s(Q^2) = \frac{\alpha(\mu^2)}{1 + \frac{33-2n_f}{12/\pi} ln \frac{Q^2}{\mu^2}} \tag{1.4}$$

in which n_f is the number of flavours and μ is the QCD scale parameter of the theory. Note that the values of n_f range between 3 and 6 thus heavy quark flavours only contribute at higher values of Q^2.

Equation 1.4 shows that α_s diverges to infinity at low transferred momenta. This property is known as *confinement*: constituents bound in the hadron, neither quarks nor gluons are observed as free particles. The absence of free colour charges which characterizes QCD can be described considering the static quark-antiquark potential:

$$V(r) = -\frac{4}{3}\frac{\alpha_s}{r} + \kappa r \tag{1.5}$$

which contains a Coulomb-like term and a term that increases linearly with the quark-antiquark distance (r). If we consider two quarks as bound by a color string, κ is the string tension. When trying to separate the quarks by pulling them apart, the second term makes energetically favorable for the gluons to produce a new quark-antiquark pair. Furthermore, eq. 1.4 shows the property of *asymptotic freedom*, which was discovered in 1973 by D. J. Gross, F. Wilczek and H. D. Politzer [5,6]. At high transferred momenta QCD is a free theory: α_s decreases until the quarks behave as quasi-free particles. In contrast to the QED case, in which the observed charge of the electron is smaller at larger distances thanks to the screening caused by vacuum polarization, in QCD there is no intuitive explanation of this property.

In Figure 1.2 a compilation of experimental results in physical processes at different characteristic scales confirms the trend of α_s foreseen by QCD. The coupling is strongly scale-dependent and the constant α_s is said to be *running*.

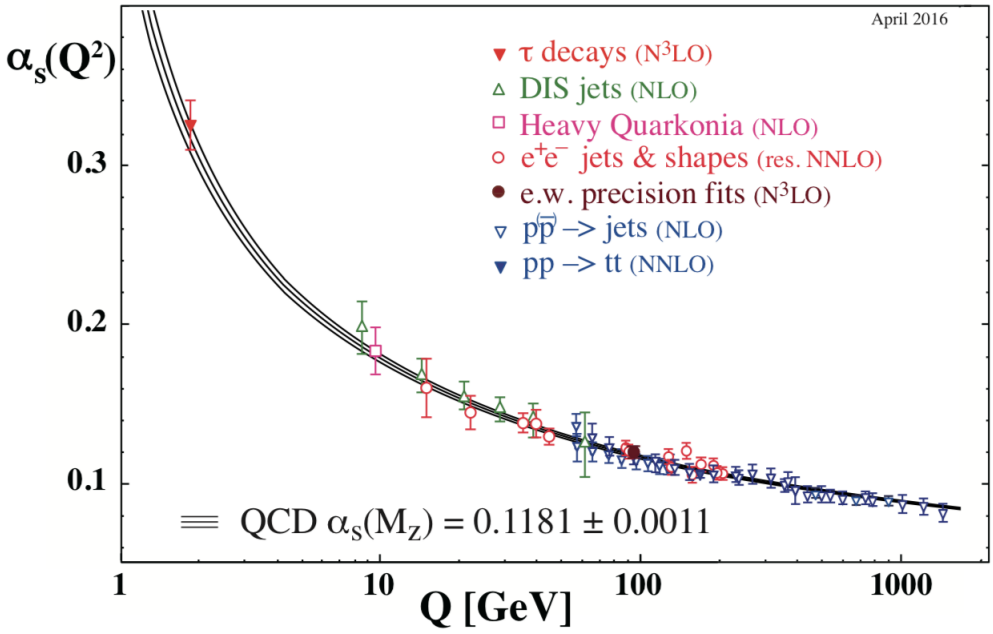

Figure 1.2: Summary of measurements of α_s as a function of the transferred momentum, Q. $\alpha_s(M_Z)$ is the value of the coupling constant at the energy scale of the Z boson mass. The respective degree of QCD perturbation theory used in the extraction of α_s is indicated in brackets (NLO: next-to-leading order; NNLO: next-to-next-to leading order; res. NNLO: NNLO matched with resummed next-to-leading logs; N3LO: next-to-NNLO) [7].

In the limit of the confinement, namely at small Q^2, where the coupling becomes large, a well-established approach to deal with QCD calculations is lattice QCD (l-QCD) [8, 9]. It consists of a discretization of the QCD Lagrangian on a hypercubic space-time lattice with given spacing, which permits to evaluate numerically the Green's functions[1] of the Lagrangian and to extrapolate the resulting observables to the continuum. A convenient way to carry out this discretization is to place the fermionic variables on the sites of the lattice, whereas the gauge fields are treated as 3×3 matrices connecting these sites. In this sense, lattice QCD is a classical four-dimensional statistical physics system [10]. Lattice QCD requires a great computing power to carry on the calculations: the main constraint is the limit imposed by the computing power available. In the limit of asymptotic freedom, namely at high Q^2, the coupling assumes small values, thus the perturbative approach used in quantum field theory can be applicable to QCD calculations. This regime is commonly referred to as perturbative QCD (p-QCD) regime.

Because only colourless objects are observed and also because of the introduction of the colour degree of freedom could lead to a proliferation of states, the colour hypothesis had to be supplemented by the requirement that only colour singlet states can exist in nature. According to the fundamental representation (3×3 unitary matrix), the basic colour singlet states are the colour-anticolour pairs, known as *mesons* ($\sum_i q_i \overline{q}^i$), and the colour-neutral bound states of quarks known as *barions* ($\sum_i \epsilon^{ijk} q_i q_j q_k$, where ϵ^{ijk} is the totally antisymmetric tensor).

The asymptotic state of matter where quarks and gluons are free only weakly bound is called Quark Gluon Plasma (QGP). In the history of the Universe, such a state existed few millionth shortly after the Big Bang, before the expansion and consequent *cooling* of the system caused the partons to recombine in confined hadrons, by going through a *phase transition*.

[1] A Green's function is an integral kernel that can be used to solve differential equations from a large number of families.

1.1.1 The QCD Phase Transition

Thermodynamical information is often provided in the form of a phase diagram. Hadronic matter can be represented defining a temperature T, related to the average kinetic energy of the relevant degrees of freedom of the system, and a baryochemical potential μ_b that indicates the net baryon density of the system and corresponds to the conservation of the baryon number, which is given by the number of baryons minus the number of anti-baryons in the hadronic phase. μ_b actually quantifies the change of the internal energy U of a system caused by the addition of a baryon or anti-baryon. Phase transitions are classified according to the velocity of the free energy to vary around the transition temperature. If the process happens in a discontinuous way in the first derivative of the free energy, the transition is known as *of the first order* (e.g., the case of solid-to-liquid transition) while if the process happens in a discontinuous way in the subsequent derivatives of the free energy, the transition is known as *of the second order*. An example of the latter is the loss of permanent magnetisation in a ferromagnet. If the transition is continuous and there are no sudden changes from a phase to another, a *cross-over* occurs. In Figure 1.3, a simple version of the phase diagram of strongly interacting matter is reported [11]. For low temperature values and $\mu_b \approx 1$ GeV, partons are bound in the ordinary hadronic matter. For large values of the baryochemical potential a phase transition to the deconfined state occurs and the temperature drops, following a curve of constant energy density. Moving towards high temperatures but low μ_b the system undergoes a crossover transition to a deconfined state: due to the increase of the temperature, the average momentum exchange between quarks and gluons increases as well. The constituents are no longer confined in colour singlets, they become a plasma of free coloured partons, the QGP. The critical temperature at which the cross-over from a hadron gas to a QGP occurs is estimated to be $T_c = 156 \pm 9$ MeV [12].

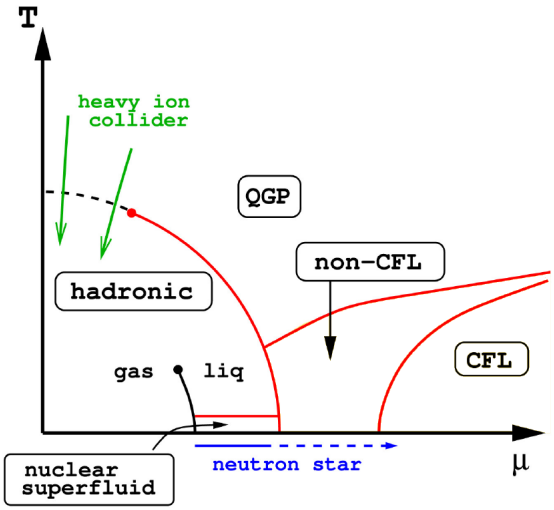

Figure 1.3: Schematic phase diagram of the strongly interacting matter as a function of temperature and baryochemical potential. The Color-Flavour Locked (CFL) phase is the color superconducting phase that occurs at asymptotically large chemical potential from 5 to 10 times the baryochemical potential of ordinary matter, e.g. core of neutron stars. The green arrows denote the regions of the phase diagram that are being explored by the experimental heavy-ion programs at the LHC and RHIC [11].

1.2 Heavy-ion collisions: reconstructing the *Little* Bang

Ultra-relativistic heavy-ion collisions produce *fireballs* made of extraordinarily hot hadronic matter, at initial energy densities that exceed the energy density of atomic nuclei in their ground states by two to three orders of magnitude. Currently they are the only known way to cross the phase boundary between ordinary hadronic matter and QGP in the laboratory. Nowadays there are two main hadron colliders with a heavy-ion programme: the Relativistic Heavy Ion Collider (RHIC) at the Brookhaven National Laboratory (BNL) and the Large Hadron Collider (LHC) at CERN (see Chapter 2). There are also two accelerators at fixed target with dedicated experiments: the Super Proton Syncrotron (SPS) at CERN and the Schwerionensynchrotron (SIS) at the Gesellschaft für Schwerionenforschung (GSI).

The evolution of the heavy-ion *little bangs* has been compared to the *Big Bang* from which our Universe originated (see Figure 1.4). The system from a little or Big Bang undergoes Hubble-like expansion and features a hierarchy of decoupling processes driven by the expansion dynamics. The two systems are different in some other aspects, to start with their expansion rates that differ by about 18 orders of magnitude, and they evolve on different time and distance scales (and by different interactions, consequently). Finally, the little bangs expansion is 3-dimensional and driven by pressure gradients, the Big Bang one is 4-dimensional and controlled by gravity [13].

1.2.1 Space-time evolution

The different stages that characterize the evolution of the system created in heavy-ion collisions can be qualitatively described by the picture formulated by Bjorken [14]. Figure 1.5 summarises in a space-time diagram the current view on the evolution of a heavy-ion collision. While z represents the spatial coordinate along the beam direction, τ is the proper time. Before colliding, the two atomic nuclei travel in the beam line ($\tau < 0$ fm/c) at relativistic energies. At $\tau = 0$ fm/c, the two Lorentz contracted nuclei collide.

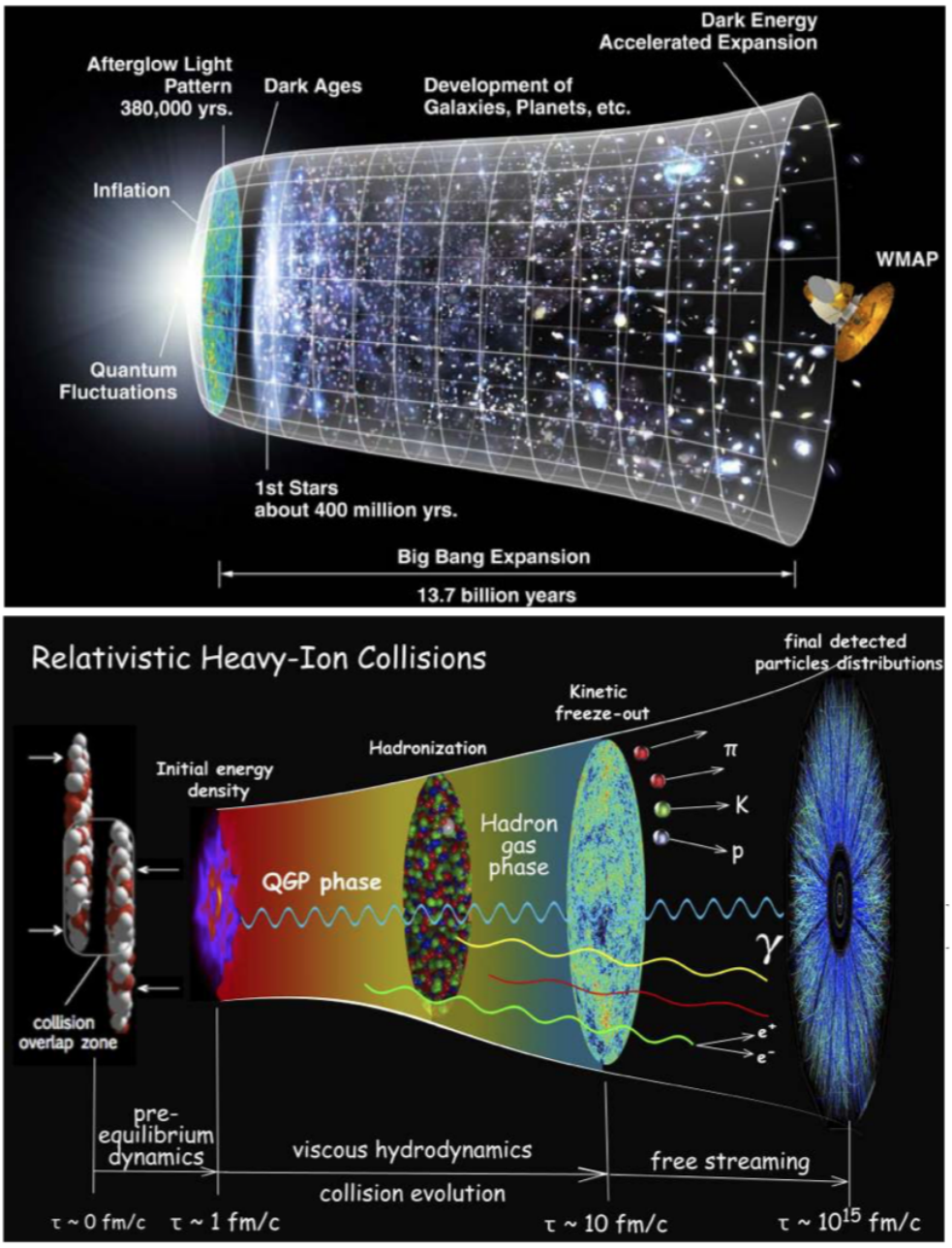

Figure 1.4: Artist's conception of the evolution of the Big Bang (top – credit: NASA) and the Little Bang (bottom – credit: Paul Sorensen and Chun Shen) [13].

If E_{beam} is the beam energy per nucleon and m is the nucleon mass, the Lorentz factor $\gamma = \frac{E_{beam}}{m}$ is $\gamma \sim 110$ at RHIC and $\gamma \sim 3000$ at LHC. Both values refer to accelerators' highest energies.

The remnants of the original nuclei, known as *spectator nucleons*, fly along the beam line while, due to the high energy density of the system in rapid expansion, the *participant nucleons* form a *fireball*. Processes at high momentum transfer, such as the production of highly energetic partons (later fragmenting to jets) and heavy-flavour quarks, occur right after the impact. In the fireball, before the system thermalises, quarks and gluons are present, prompt leptons and photons, which do not interact strongly with quarks and gluons, can be emitted. At $\tau \sim 1$ fm/c the QGP forms and before the energy density drops below the critical value, the matter deconfinement occurs. The QGP, as a strongly interacting fluid, then thermalises, expands and cools down approximately adiabatically. Pressure gradients due to space time asymmetries in the original collision region and fluctuations in the geometry might develop affecting the expanding system. With its expansion the system crosses the phase boundary between Quark Gluon Plasma and ordinary hadronic matter. When the critical temperature between the two phases is reached, the hadronisation starts and the system evolves into an interacting hadron-resonance gas. While expansion and contextual cooling of the system continue, the relative abundances of hadron species can be modified until the particles in the hadron gas are able to interact inelastically. When the inelastic interactions cease (*chemical freeze-out*), the particle abundances are fixed. Although the system reached its final chemical composition, elastic interactions are still present and continue to affect the kinetic properties of the hadrons. Finally, the mean free path of the hadrons becomes too large, elastic collisions stop: the *kinetical freeze-out* is reached and the particle momenta are fixed. For $\tau \sim 10$ fm/c hadrons created in the collision escape the interaction region with no further interaction in a *free-streaming* regime, flying toward the surrounding experimental apparata. Unstable particles, like weakly decaying ones and hadronic resonances, decay and the decay products are free to hit the detector. On the *proper-time* hyperbola $\tau = (t^2 - z^2)^{(1/2)} = \text{constant} \sim 1$ fm/c, the energy density

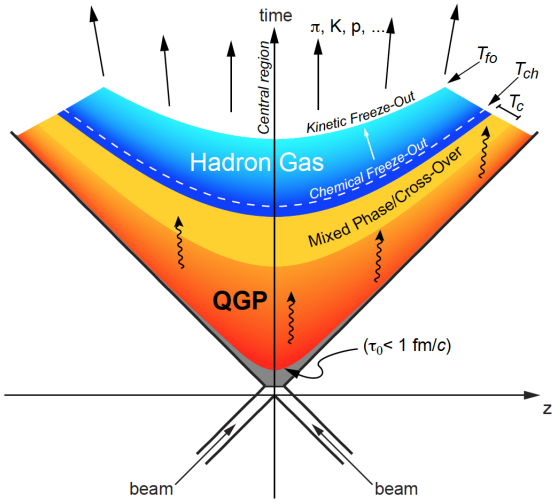

Figure 1.5: Evolution of a central heavy ion collision in a Minkowski-like plane. The z direction is parallel to the beam line. T_c is the critical temperature (see Paragraph 2.1.2) while T_{ch} and T_{fo} respectively indicate the chemical and kinetical freeze-out temperatures.

is $\epsilon \sim 1 - 10$ GeV/fm^3. Natural variables in which the evolution is described are the proper time (τ) and the rapidity (y) which is an important quantity related to Lorentz linear transformation. It is defined as

$$y \equiv \frac{1}{2} \ln \left(\frac{E + p_{\mathrm{L}}}{E - p_{\mathrm{L}}} \right) \tag{1.6}$$

where E and p_z are the first and the fourth components of the four-momentum, respectively. To calculate this quantity momentum and mass of the particle are needed. In the ultra-relativistic scenario, where $m \ll E$, the rapidity converges to the definition of pseudorapidity (η) which is defined as

$$\eta = \frac{|\mathbf{p}| + p_z}{|\mathbf{p}| - p_z} = -ln[tan(\theta/2)] \tag{1.7}$$

where θ is the angle between the particle three-momentum $\mathbf{p}$ and the positive direction of the beam axis.

1.2.2 QGP signatures

In order to study the evolution of the fireball, it is important to identify which experimental observables provide information on the QGP formation. Depending on the phase of the collision in which they are produced, there are two different kinds of probes: signatures created in the very first instants of the collisions, also called *hard probes*, and signatures originated in the QGP phase, also called *soft probes*.

Hard probes

High momentum particles which can be created only at the very early stages of the collisions, provide a tool to inquire into the mechanisms driving the parton propagation and energy loss in the QGP. If a two-nuclei collision (A-A) can be described as the superposition of uncorrelated binary collisions between nucleons, the observed production cross section for hard particles in A-A should be equal to the pp cross section scaled by the average number of binary collisions, $\langle N_{coll} \rangle$. Considering the high average transverse momentum region, the nuclear modification factor is defined as

$$R_{AA} = \frac{1}{\langle N_{coll} \rangle} \frac{d^2N_{AA}/dp_{\mathrm{T}}dy}{d^2N/dp_{\mathrm{T}}dy} \tag{1.8}$$

where $d^2N_{AA}/dp_{\mathrm{T}}dy$ is the yield in A-A collisions, while $d^2N/dp_{\mathrm{T}}dy$ is the yield in pp collisions. It would be expected to be equal to unity. Instead, high-momentum partons tend to lose energy while traversing the hot and dense strongly-interacting plasma, resulting in a suppression of the high transverse momentum component of hadron spectra and jets [15]. Measuring the nuclear modification factor for hadrons and jets makes possible to estimate the energy loss of hard partons and, consequently, explore the properties of the created medium. In Figure 1.6 the R_{AA} measured by the ALICE Collaboration as a function of p_{T} for pions, kaons and protons, for different centrality classes, at $\sqrt{s_{NN}}$ = 2.76 TeV are shown [16]. In central Pb-Pb collisions, a strong deviation from one is observed for values of $p_{\mathrm{T}} > 8$ GeV/c. The suppression evolves with centrality, being stronger in most central Pb-Pb collisions than in peripheral ones. This suggests substantial energy loss for partons that traverse the medium produced in the collision. As one

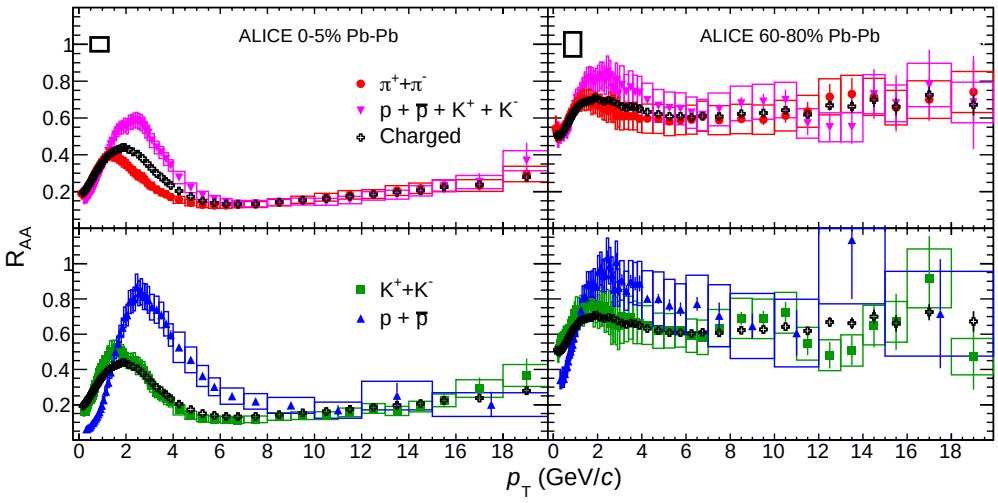

Figure 1.6: Nuclear modification factor (R_{AA}) measured in Pb–Pb collisions at $\sqrt{s_{NN}} = 2.76$ TeV for identified pions, kaons and protons as a function of p_{T} for different centrality classes [16].

can evince from the definition of R_{AA}, measurements of particle production spectra in pp collisions provide an essential reference to compute the R_{AA}.

Jet/parton quenching also refers to the suppression of high momentum particles and jet and to the energy loss of partons traversing the hot deconfined medium. Dijets are physical objects consisting of two back-to-back jets of equal transverse momentum. If the two partons from which the dijets originate are created by a hard scattering in a heavy-ion collision, they interact with the medium losing part of their energy and changing their direction. Consequently, depending on the length of the path of each parton inside the medium, the dijet structure is modified leaving a leading jet (the unquenched one) and a subleading jet (the quenched one). Differences between quenched and unquenched jets can be useful to provide information on the nature of the system after the collision [17].

J/Ψ suppression should provide an unambiguous signature of QGP formation [18]. *Heavy* quarks (c, b and t) can not be produced in the fireball after thermalisation: their masses are larger than the energy scale associated to the QGP temperature hence they

have to be produced by hard processes before the QGP formation. Bound states formed by a charm quark and a charm anti-quark, generally known as *charmonium*, or by a beauty quark and a beauty anti-quark, generally known as *bottomonium*, seem to be suppressed in central heavy-ion collisions because of the *colour screening* (for a more detailed description, see [18]). J/Ψ meson suppression has been the first QGP signature to be experimentally confirmed by the NA50 Collaboration [19].

Hard emission of thermal dileptons and photons is a sort of internal probe since they are produced by the QGP itself. Because of $\alpha_{EM} \ll \alpha_s$ leptons and photons mostly escape the fireball without interacting, thus they carry information on the properties of the early stages of the system and the temperature of the fireball. Unfortunately, for the same reason, it is very difficult to separate thermal dileptons and photons from the abundant hadronic production and from the overwhelming prompt background from $\pi^0 \to \gamma\gamma$ produced during the early hard partons interaction.

Soft probes

Transverse momentum spectra of hadrons of identified particles give important insights about the condition of the medium at kinetic freeze-out. Assuming a Boltzmann–Gibbs distribution for the particle emission, taking into account only the thermal component of the spectra and predicting a common emission temperature (β), the particle spectra for the species i can be modelled as

$$\frac{1}{m_{\mathrm{T}}}\frac{d^2N_i}{dm_{\mathrm{T}}dy} \propto e^{-\beta m_{\mathrm{T}}} \tag{1.9}$$

where $m_{\mathrm{T}} = \sqrt{m_0^2 + p_{\mathrm{T}}^2}$ is the transverse mass. The measured spectra in heavy-ion collisions exhibit a different slope (i.e. temperature) for different particle species. In Figure 1.7 it is possible to see a steeper spectrum slope for pions while for protons the slope of the spectrum is reduced. Data are fitted with a Blast–Wave model. Figure 1.7 shows that most of the particles are produced at low p_{T}: those are light hadrons formed

in the hadronisation of soft partons after the QGP phase. In contrast, the high p_{T} region is dominated by processes with large energy transfer, e.g. jets.

Strangeness enhancement has been predicted long time ago to be a signature of the QGP formation [20]. Unlike up (u) and down (d) quarks, which form ordinary matter, strange (s) quarks are not present as valence quarks in the initial state, but they are sufficiently light to be abundantly created during the collision. The thermal production of strange quarks, allowed by the high temperature of the system ($T_{QGP} \sim 300$ MeV), leads to a strangeness enhancement in the final state. During the phase transition, because of the restoration of chiral simmetry[2], the threshold for the production of a $s\bar{s}$ pair reduces from twice the mass of the constituent strange quark to twice the intrinsic mass of the quarks. Furthermore, because of the recombination mechanism, the deconfined phase can also enhance the production of multi-strange baryons. An enhanced production of hyperons is therefore expected to be a signal of a deconfined phase.

Anisotropic flow concerns the azimuthal distribution of the particles in the plane perpendicular to the beam direction. Right after the nuclei collide the geometrical overlap region, and consequently the initial matter distribution, is anisotropic: the area takes an elliptic shape. If xy is the transverse plane and z the beam axis, the asimmetry can be parametrized using the eccentricity, defined as

$$\epsilon \equiv \frac{\langle y^2 - x^2 \rangle}{\langle x^2 + y^2 \rangle} \tag{1.10}$$

Considering that the matter is strongly interacting, the spatial asymmetry translates into the anisotropy of the final momentum distribution.

$$\epsilon_p \equiv \frac{\langle p_y^2 - p_x^2 \rangle}{\langle p_x^2 + p_y^2 \rangle} \tag{1.11}$$

In order to measure the azimuthal anisotropy, it is useful to look at the Fourier expansion

[2]It is predicted that the spontaneous breaking of chiral-symmetry is restored at temperatures prevailing in the QGP phase. [3]

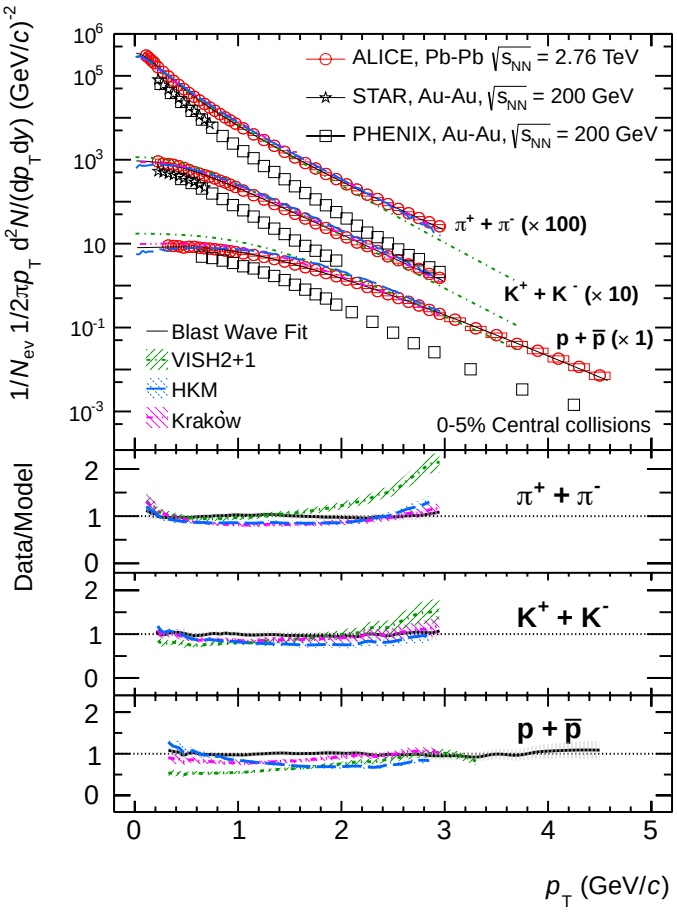

Figure 1.7: Pion, kaon and proton transverse momentum spectra in central (0-5%) Au–Au collisions at $\sqrt{s_{\rm NN}} = 200$ GeV at the RHIC and in Pb–Pb collision at $\sqrt{s_{\rm NN}} = 2.76$ TeV at the LHC. The data are fitted with a Blast–Wave model (lines) and compared with three additional hydrodynamical models predictions (shaded areas). [16].

in the azimuthal angle of the production spectra:

$$\frac{dN}{d\phi} \propto 1 + 2\sum_{n=1}^{\infty} \nu_n cos[n(\phi - \Psi_n)] \tag{1.12}$$

in which the magnitude of the anisotropy is ν_n. The second order coefficient in the Fourier transform of the final state hadron azimuthal distribution (ν_2) is known as *elliptic flow*. If the medium is approximable to an ideal fluid with viscosity $\eta = 0.02$, the parton interactions in the overlap region generate pressure gradients of different magnitudes in different directions. The properties of the medium, such as the shear viscosity over entropy η/s, the bulk viscosity over entropy ξ/s and its lifetime, define how efficiently these initial geometric condition and inhomogeneities are translated in the ν_2 coefficients; thus, the comparison of the experimentally measured ν_2 with theoretical models permits to uncover the characteristics of the medium and its thermodynamic properties.

1.3 QGP-like effects in small systems

Studies in smaller systems provide a benchmark to better understand the development of collision mechanisms and a tool to investigate the nuclear parton density functions. Furthermore, a comparison between p-Pb and pp collision systems allows to test the Glauber model [21] assumption that nucleons, considered to be point like and independent inside the colliding nuclei, are subjected only to hadronic interactions which do not deflect the trajectories of colliding nucleons. In the recent years there has been a surge of interest in collective effects in small systems with high final state multiplicity following the observation of strangeness enhancement from ALICE [22] and the *ridge* and *double-ridge* in long-range particle correlations by ATLAS [23] and CMS [24, 25]. These observations are reminescent of collective effects that in heavy-ion collisions are attributed to the formation and dynamical evolution of the QGP. Small systems unexpectedly become of considerable interest as they open the exciting opportunity of a microscopic understanding of phenomena known from nuclear reactions and the possibility that these are connected to the formation of a deconfined QCD phase at high temperature and energy

density.

Enhanced production of multi-strange hadrons

The ALICE experiment has measured the multiplicity dependence of the production of primary strange (K^0_S, Λ, $\bar{\Lambda}$) and multi-strange (Ξ^-, $\bar{\Xi}^+$, Ω^-, $\bar{\Omega}^+$) hadrons in pp collisions at $\sqrt{s} = 7$ TeV [22]. The ration of strange and multi-strange particles relative to pions (non-strange) increases as a function of $\langle dN_{ch}/d\eta \rangle$ from low multiplicity pp to high multiplicity p–Pb reaching the values observed in Pb–Pb collisions. In small systems quantum numbers conservation laws (i.e. strangeness) have to be applied event-by-event, while in larger systems, which have many degrees of freedom, they can be applied in average. The conservation of quantum numbers reduces the phase space available for particle production. Further studies extending to higher multiplicity in small systems would be useful to demonstrate whether strangeness production saturates. In Figure 1.8 the ratios of the yields of K^0_S, Λ, Ξ and Ω to the pion ($\pi^+ + \pi^-$) yield as a function of $\langle dN_{ch}/d\eta \rangle$ are compared to p–Pb and Pb–Pb results at the LHC.

Two-particle angular correlations

The measurements of two-particle angular correlations performed in pp collisions have shown new behaviors, which are not reproduced by Monte Carlo event generators, that may hint to the presence of collective phenomena. More specifically it is observed that particles coming out of the collision are aligned in their azimuthal angle over a large pseudorapidity gap. This *ridge*-like structure is found to be absent in minimum bias events but emerges as particle multiplicity reaches high values. In Figure 1.9 the distributions of the angular correlation of particle pairs are reported as function of $\Delta\phi$ and $\Delta\eta$ which are the differences in the azimuthal angle (ϕ) and pseudorapidity (η) of the pair. The distributions exhibit a variety of features:

- a narrow peak at $(\Delta\eta, \Delta\phi) \sim (0, 0)$ is due to particles coming from the same high p_{T} process (e.g., jets).

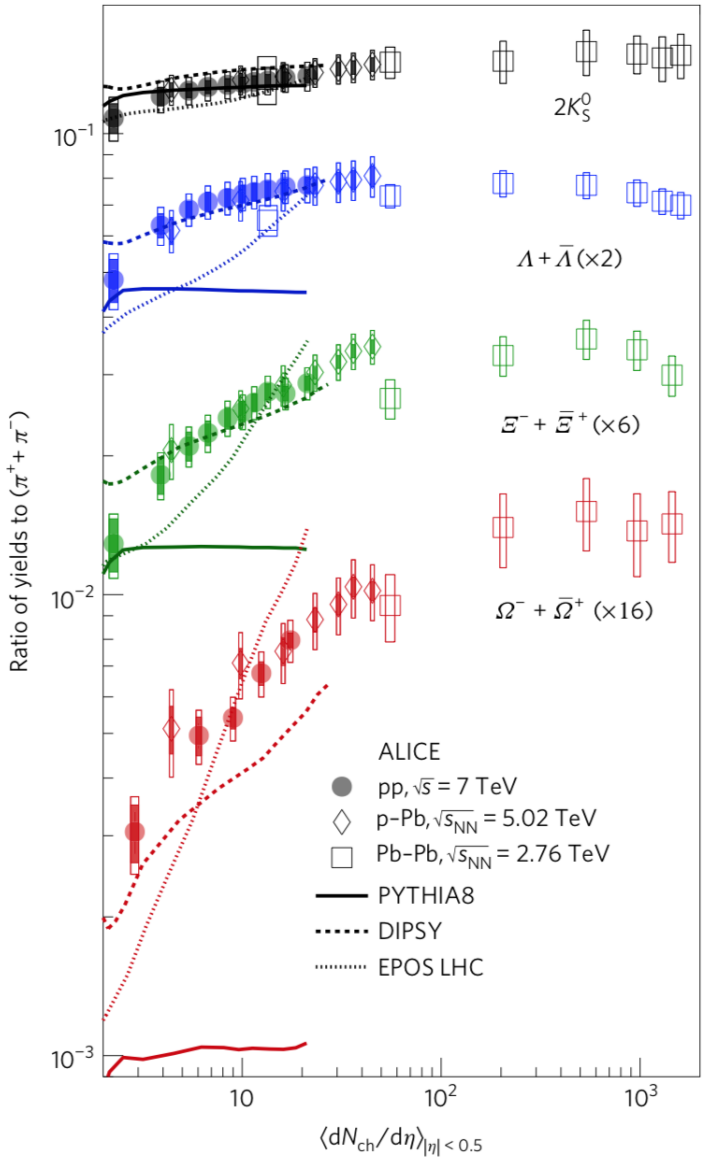

Figure 1.8: p_{T}-integrated yield ratios to pions $(\pi^+ + \pi^-)$ as a function of $\langle dN_{ch}/d\eta \rangle$ measured in $|y| < 0.5$. The error bars show the statistical uncertainty, whereas the empty and dark-shaded boxes show the total systematic uncertainty and the contribution uncorrelated across multiplicity bins, respectively. The values are compared to calculations from MC models and to results obtained in p–Pb and Pb–Pb collisions at the LHC. For Pb–Pb results the ratio $2\Lambda/(\pi^+ + \pi^-)$ is shown [22].

- a Gaussian-like structure at $\Delta\eta \sim 0$ covering all the values of $\Delta\phi$ arises from the decay of lower p_{T} (e.g., soft QCD string fragmentation).

- an elongated *ridge*-like structure at $\Delta\phi \sim \pi$ along the whole range of $\Delta\eta$ caused by recoiling jets (or more generally interpreted as global momentum conservation).

In high-multiplicity pp collisions a double-ridge structure can be recognised: besides the ridge for $\phi = \pi$, a second structure, extending over the entire $\Delta\eta$ range, is visible around $\Delta\phi = 0$. A similar structure of the correlation function is found in p-Pb collisions at $\sqrt{s_{NN}} = 5.02$ TeV [26] and in central Pb-Pb collision at $\sqrt{s_{NN}} = 2.76$ TeV [27], where the collective flow is known to occur.

Multiplicity dependence of the average transverse momentum

The measurement of the average transverse momentum ($\langle p_{\mathrm{T}} \rangle$) distribution versus the charged-particle multiplicity in pp collisions at energies of $\sqrt{s} = 0.9$, 2.76, 7 TeV and in p-Pb collisions at $\sqrt{s_{NN}} = 5.02$ TeV, together with a comparison to Pb-Pb collisions results at $\sqrt{s_{NN}} = 2.76$ TeV, has been performed with the ALICE detector [28].

The average transverse momentum of charged particles increases with multiplicity more steeply in pp and p-Pb collisions than in Pb-Pb. In small systems, the effect is attributed in [28] to multi-parton interactions and to a final-state color reconnection mechanism. In Figure 1.10 the strong increases of $\langle p_{\mathrm{T}} \rangle$ observed at different collision energies are reported. Data are compared to calculations with the Monte Carlo event generators. For pp collisions, calculations with PYTHIA are shown with and without the color reconnection (CR) mechanism. The observed slight dependence on energy is not sufficient to explain the rapid increase of the $\langle p_{\mathrm{T}} \rangle$ with the multiplicity. In contrast, Pb–Pb collisions are only characterized by a moderate increase in $\langle p_{\mathrm{T}} \rangle$ usually attributed to the established presence of radial flow.

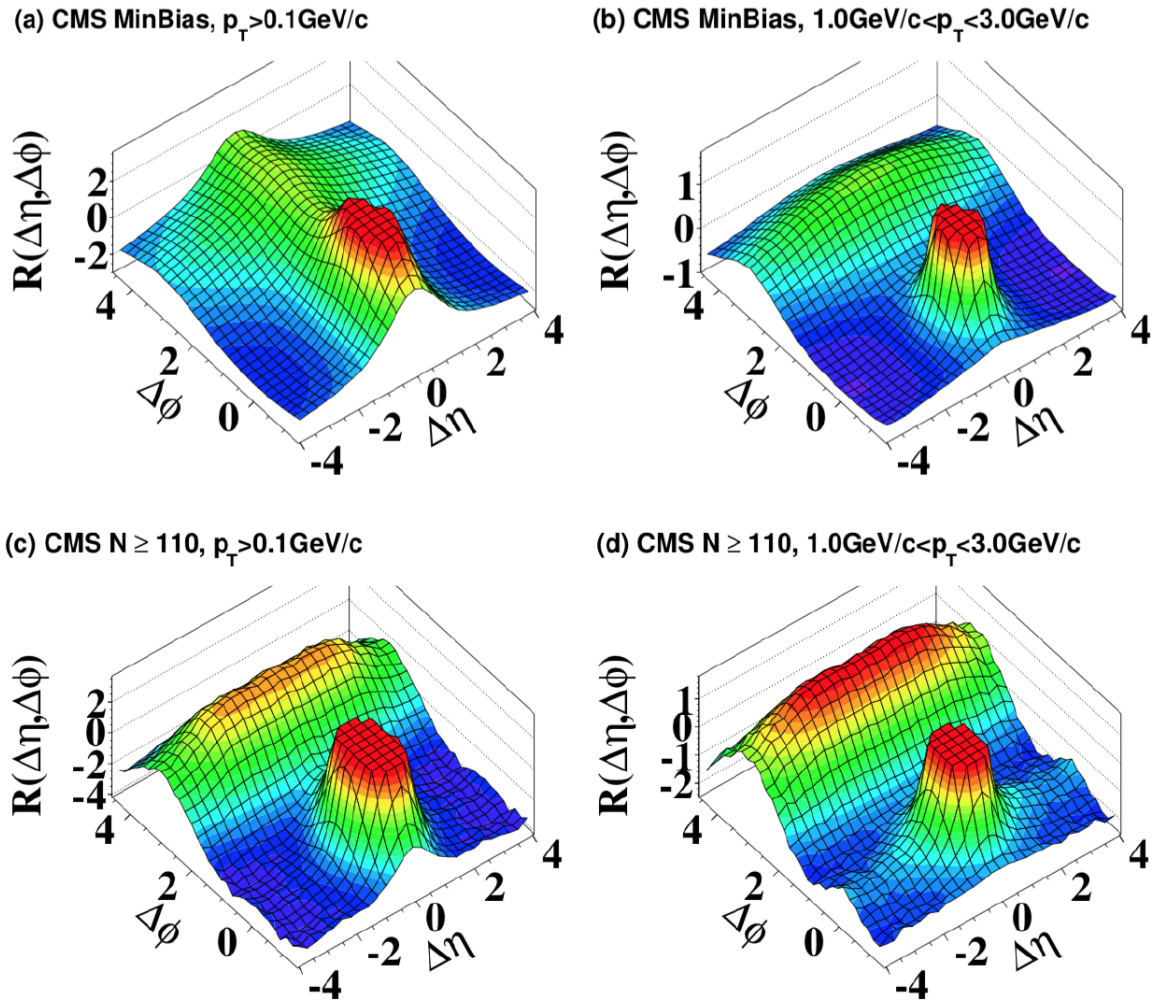

Figure 1.9: 2D dihadron correlation functions for minimum bias pp collisions at $\sqrt{s} = 7$ TeV (a) with $p_{\mathrm{T}} > 0.1$ GeV/c and (b) with $1 < p_{\mathrm{T}} < 3$ GeV/c and for high multiplicity ($N \geq 110$) pp collisions at $\sqrt{s} = 7$ TeV (c) with $p_{\mathrm{T}} > 0.1$ GeV/c and (d) with $1 < p_{\mathrm{T}} < 3$ GeV/c, measured by CMS experiment at LHC. The *ridge* refers to the structure in (d) that has a narrow width around $\Delta\phi = 0$ and extends over the entire $\Delta\eta$ range [25].

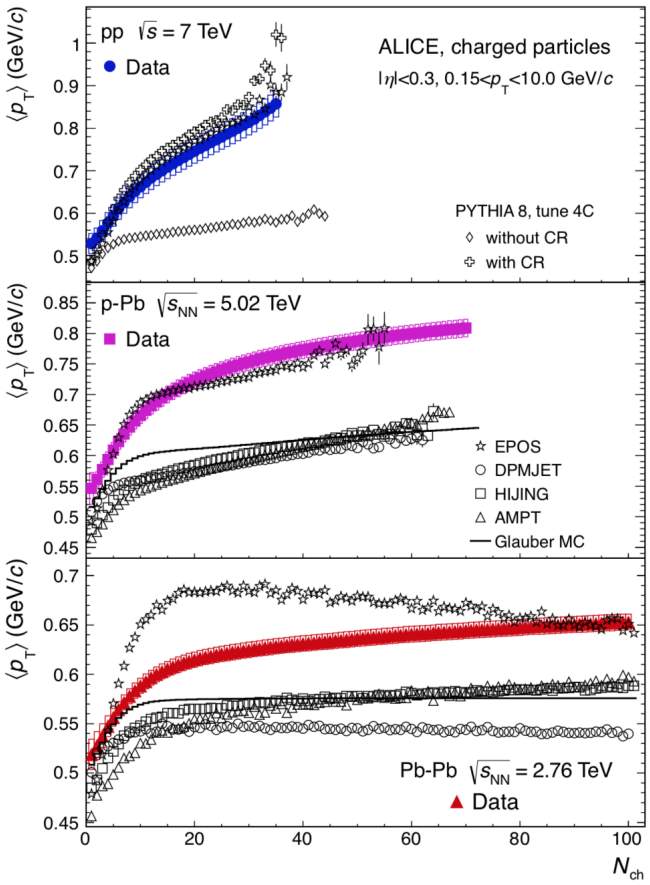

Figure 1.10: Comparison between pp, p–Pb, and Pb–Pb collisions, for $\eta < 0.3$ [28].

J/Ψ production

An enhancement in the production of J/Ψ in the di-lepton channel has been observed comparing high multiplicity with minimum-bias pp collisions at $\sqrt{s} = 7$ TeV [29]. The result could show that pp collisions also exhibit a collective behavior as seen in heavy-ion collisions. In Figure 1.11 an approximately linear increase of the relative J/Ψ yield with the charged particle multiplicity is reported at mid-rapidity ($|y| < 0.9$) and forward rapidity ($2.5 < y < 4$). The increase is similar at forward and mid-rapidity, exhibiting an enhancement relative to minimum bias J/Ψ yield by a factor of about 5 at $2.5 < y < 4$ (8 at $|y| < 0.9$) for events with four times the minimum bias charged particle multiplicity. In 1.12 the prediction by PYTHIA 6.4.25 exhibits a decrease of the J/Ψ multiplicity as a function of the event multiplicity which indicates that hard J/Ψ production is not accompanied by an increase of the total hadronic activity.

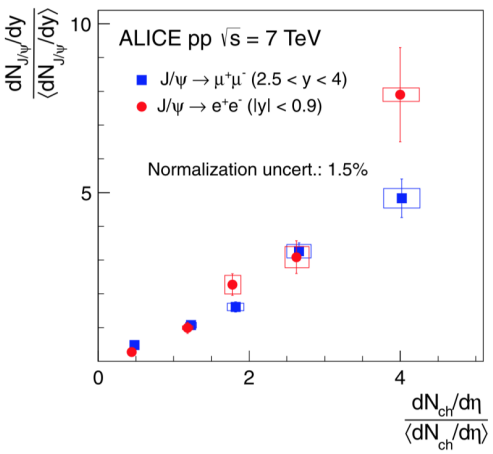

Figure 1.11: Relative J/Ψ yields measured at forward and at mid-rapidity as a function of the relative charged particle density around mid-rapidity with the ALICE experiment.

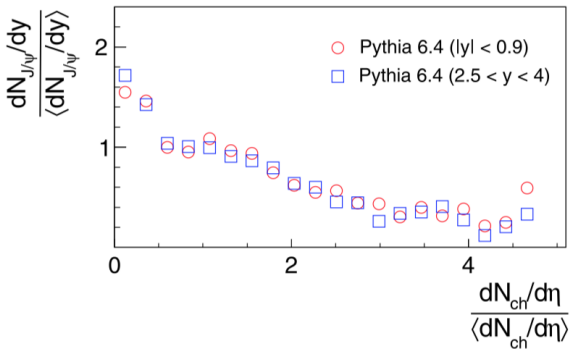

Figure 1.12: Ratio of the multiplicity distributions generated for minimum bias events and events containing J/Ψ from hard scattering [29].

Chapter 2

LHC and ALICE experiment

Over the last sixty years there have been significant developments in the field of elementary particle physics. Besides the technological evolution, there has been a paradigm shift as a result of design and construction of accelerators: particle physicists were *hunters* (of cosmic rays) and became *farmers*. Particles accelerators were invented in the 1930s to provide energetic particles to investigate the structure of the atomic nucleus; nowadays they are machines that use electromagnetic fields to propel charged particles to nearly light speed and to contain them in well-defined beams.

2.1 Accelerating protons and ions at the Large Hadron Collider

The European Organization for Nuclear Research (CERN) was officially founded in 1954, its laboratories are located along the Franco-Swiss border near the city of Geneva. Since then, the CERN's facility has been growing with the addition of many new elements. As shown in Figure 2.1, the Large Hadron Collider (LHC) [30] is the last element of the accelerator complex chain: it is the largest and most powerful particle accelerator in the world, a collider placed 40-170 m underground, in the same tunnel of 27 km circumference originally built for its predecessor, the Large Electron–Positron collider (LEP). It

is designed to provide pp collisions with up to $\sqrt{s} = 14$ TeV centre-of-mass energy at an instantaneous luminosity of $10^{34}\ cm^{-2}s^{-1}$. In addition to protons, the LHC can also collide ion (Pb-Pb, Xe-Xe) and asymmetric (p–Pb) beams. By design, the maximum energy in Pb-Pb collisions is $\sqrt{s} = 5.5$ TeV per nucleon, which will be reached during the 2020-2030 data taking, whereas the maximum energy reached during the first 10 years of operations was 5.02 TeV for Pb ions and 13 TeV for pp.

Protons are extracted from a hydrogen tank by removing the electrons. The first accelerating step is in the LINAC2, where the maximum energy reached by the beam is E_{beam} = 50 MeV. They arrive soon after to the Proton Synchrotron Booster (PSB), where E_{beam} = 1.4 GeV, then to the Proton Synchrotron (PS), where E_{beam} = 25 GeV. Later they reach Super Proton Synchrotron (SPS), where E_{beam} = 450 GeV and, finally, they are injected in the LHC in which they gain their final energy.

Lead ions come from a purified sample of lead heated to high temperature ($\sim 500^{o}$C) and then ionised partially by a stream of electrons. Ions with different charge are created during this step, among them only Pb^{29+} is selected. The first accelerating step is in the LINAC3, where E_{beam} = 4.2 MeV/nucleon. More electrons are stripped by passing the ions through a carbon foil. Only Pb^{54+} is kept to be accumulated and then accelerated in the Low Energy Ion Ring (LEIR), where E_{beam} = 72 MeV/nucleon. Each beam is later transfered to the PS, where E_{beam} = 5.9 GeV/nucleon and, after a second foil to obtain fully stripped Pb^{82+} ions, it arrives to the SPS, where E_{beam} = 177 GeV/nucleon. It is finally injected in the LHC where ions reach their final energy.

Particles are injected in the LHC grouped in bunches which collide in one of the interaction points along the main ring. Four main experiments have been built in correspondence of the LHC interaction points: ALICE [31] , ATLAS [32], CMS [33] and LHCb [34]. LHC started the data taking in 2009 ("Run 1") with its first pp collisions at $\sqrt{s}$ = 900 GeV. During the first operational run the LHC reached $\sqrt{s}$ = 8 TeV. From February 2013 to May 2015 it was switched off for the first long shutdown (LS1). During the second data taking ("Run 2"), the centre-of-mass energies have reached 13 TeV for pp beams and 5.02 TeV per nucleon for Pb–Pb beams. Two short data taking

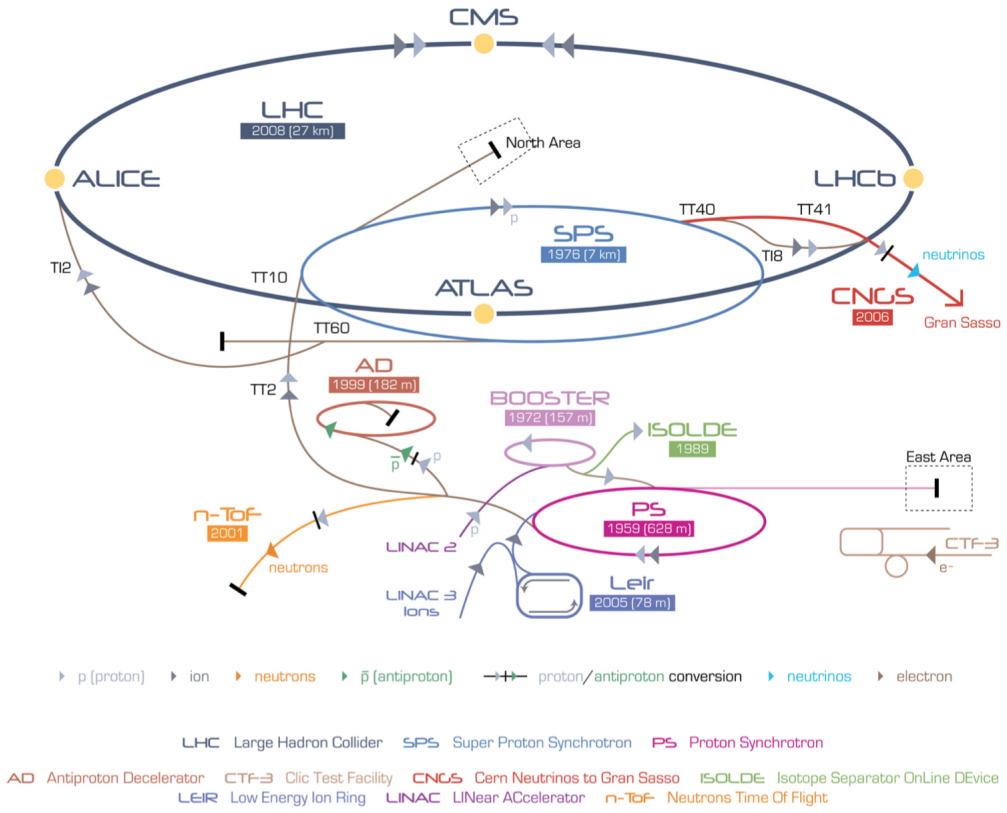

Figure 2.1: Schematic drawing of the CERN accelerator complex [35]. Steps which precede the injection of the beam in the LHC ring are visible following the lines starting from LINAC2 and LINAC3.

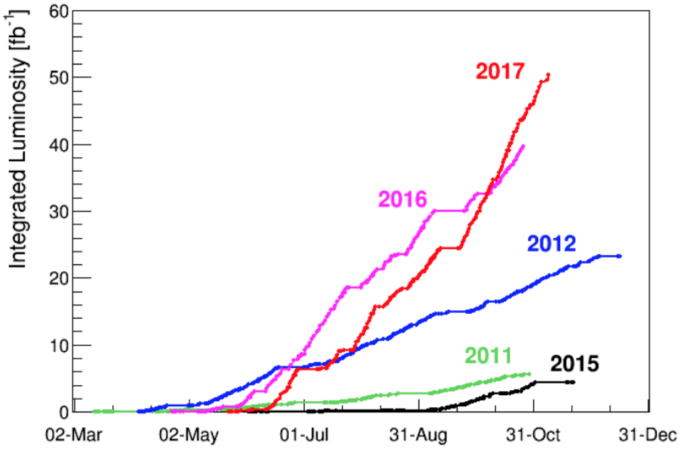

Figure 2.2: Delivered luminosity relative to pp collisions versus time for 2011-2017 [37]. The integrated luminosity is used as a performance index as it is proportional to the total number of events recorded in the detectors.

campaigns have taken place during which pp collided at $\sqrt{s}$ = 5.02 TeV (one of the data sample is used for this work) and in addition p-Pb and Pb-p collisions have been recorded at $\sqrt{s}$ = 5.02 TeV and 8.16 TeV. In October 2017, for the first time, xenon (Xe) nuclei were injected and collided in the LHC at the energy of 5.44 TeV per nucleon pair. Typical proton running conditions in the LHC during operation in Run 1 and Run 2, are shown together with the design parameters in Table 2.1 [36]. As an example of the excellent performance of the LHC, Figure 2.2 shows the luminosity delivered to the experiments during the operational runs [37]. A second long shutdown (LS2) is planned for 2019-2020.

2.2 A Large Ion Collider Experiment

ALICE is a general-purpose detector designed and optimised for the study of heavy-ion collisions. Following its predecessors' footsteps (STAR [38] and PHENIX [39] at RHIC [40]), it was designed with the aim of addressing the physics of strongly interacting matter at extreme values of energy density and temperature which can be formed in

	Design	**2010**	**2011**	**2012**	**2015**	**2016**	**2017**
Beam energy (TeV)	7.0	3.5	3.5	4.0	6.5	6.5	6.5
Protons/bunch (10^{11}p)	1.15	1.0	1.3	1.5	1.1	1.1	1.25
Max. number of bunches	2808	368	1380	1380	2244	2076	2736
Bunch spacing (ns)	25	150	50	50	25	25	25
Half crossing angle [μrad]	143	100	120	146	145	185	185
β^* [m]	0.55	2.0-3.5	1.0-1.5	0.6	0.8	0.4	0.4
Peak lum. (10^{34} $cm^{-2}s^{-1}$)	1.0	0.021	0.35	0.77	0.51	1.1	1.4

Table 2.1: Running conditions during pp data taking compared to design parameters.

ultra-relativistic nucleus-nucleus collisions. ALICE's physics programme also includes collisions with lighter ions to vary energy density and interaction volume, as well as dedicated proton-nucleus runs which provide a baseline for heavy-ion measurements. Proton-proton collisions provide reference data for the heavy-ion programme and address a number of specific QCD topics for which ALICE is complementary to the other LHC experiments.

The ALICE detector was built by a collaboration presently including over 1800 physicists and engineers from 176 institutes in 41 countries. Its overall dimensions are 16x16x26 m^3 with a total weight of approximately 10 000 t. It can track particles down to 100 MeV/c and up to 100 GeV/c and identify them in a wide momentum range. Different detectors are designed to optimize the acceptance and the detection efficiency in a very high track-multiplicity scenario.

The detector apparatus, sketched in Figure 2.3, is composed of three main parts:

- A central barrel which measures hadrons, electrons and photons covering a pseudorapidity region $|\eta| < 0.9$. It includes the Inner Tracking System (ITS), the Time Projection Chamber (TPC), the Transition Radiation Detector (TRD), the Time-of-Flight (TOF), the Ring Imaging Cherenkov (HMPID) and two electromagnetic calorimeters (PHOS and EMCal). The detectors are placed in solenoid that pro-

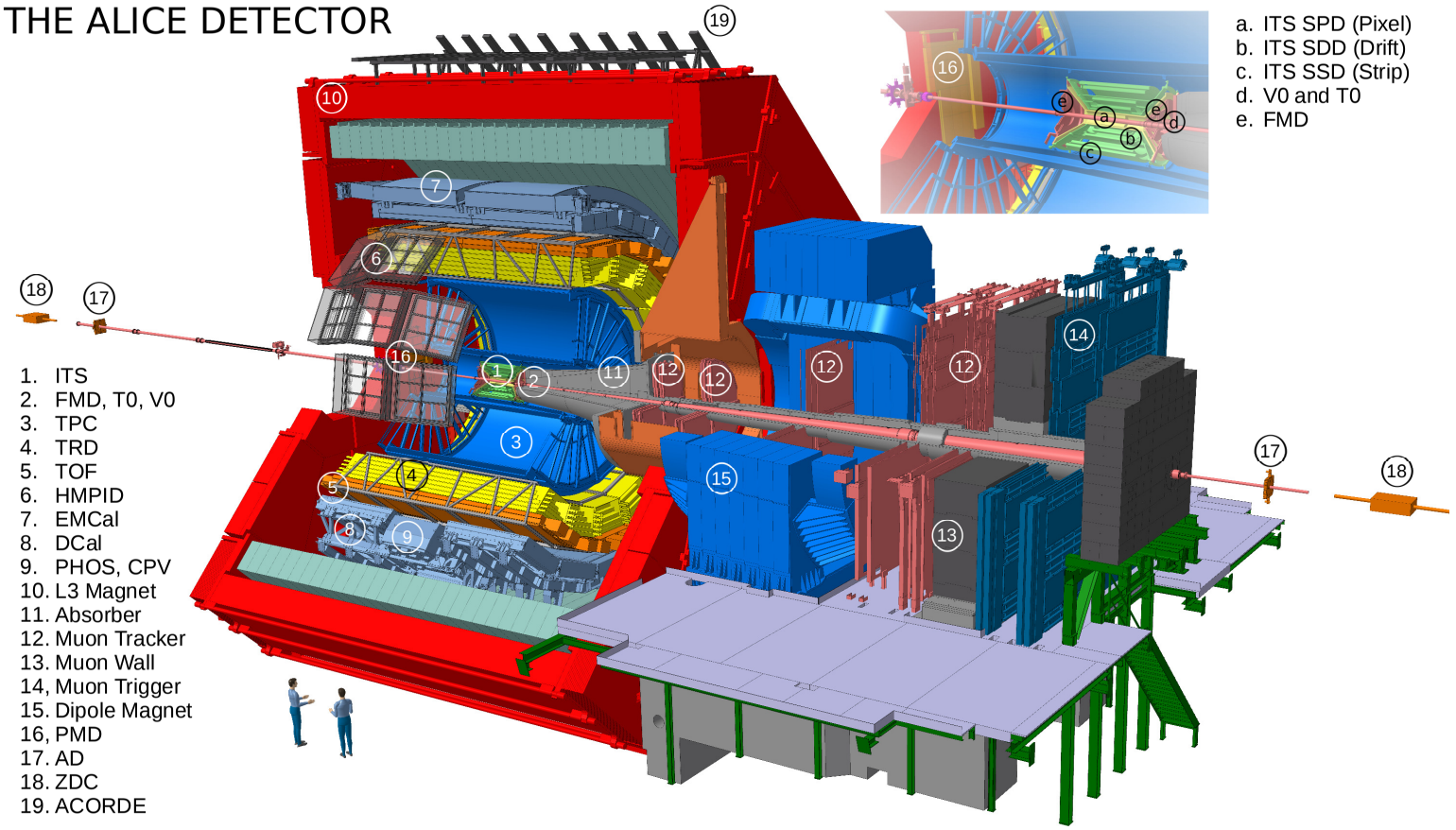

Figure 2.3: The ALICE detector [**?**].

vides a magnetic field of 0.5 T used to bend the trajectories of the particles. From the curvature of the tracks their momentum can be derived.

- A forward muon arm, covering a pseudorapidity region $-4 < |\eta| < -2.5$. It consists of a complex arrangement of absorbers, a large dipole magnet and planes of tracking and triggering chambers.

- Several smaller detectors (ZDC, PMD, FMD, T0, V0 + ACORDE) located at small angles along the beam pipe (forward rapidity region) and used for global event characterization and triggering.

Much about ALICE design and performance has been written. In the following sections a description of the detectors used in the analysis will be provided. For more details on ALICE apparatus see [41], for the performance during Run 1 see [42]. For more details on the ALICE upgrade see [43].

2.2.1 Central detectors

Inner Tracking System

The Inner Tracking System (ITS) significantly contributes to the study of several physics observables, such as multiplicity and particle spectra. Its main tasks are to localize the primary vertex with a resolution better than 100 μm, to reconstruct the secondary vertices from the weak decays of hyperons, D and B mesons, to track and identify particles with low momentum (down to 100 MeV/c), to improve the momentum and angular resolution for particles reconstructed by the TPC. As shown in Figure 2.4, ITS is a six-cilindrical-layer silicon vertex detector (3.9 cm < r < 43.6 cm) placed coaxially around the beam pipe (800 μm thick beryllium cylinder of 3 cm of radius) designed to have large acceptance ($|\eta| < 0.9$), very low material budget to minimize the multiple scattering effect, and high spatial precision and granularity to guarantee very low occupancy in nucleus-nucleus collisions. Because of the decrease of track density from the inside out (from 50 tracks/cm^2 to 1 track/cm^2), Silicon Pixel Detectors (SPD) have been chosen

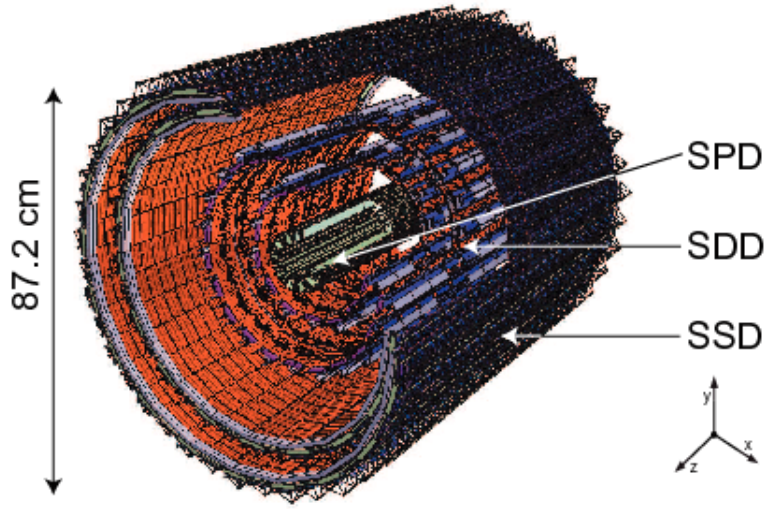

Figure 2.4: Layout of the ITS [44]. The global reference system has indeed its origin in the middle of the ITS, so that the z direction coincides with the beam line.

for the innermost two layers, Silicon Drift Detectors (SDD) for the intermediate two layers. The two outer layers are equipped with double-sided Silicon micro-Strip Detectors (SSD). Since they have analogue redout, the four outer layers can be also used for particle identification via measurement of the ionisation energy loss, $\mathrm{d}E/\mathrm{d}x$, in the non-relativistic region. The characteristics of the six ITS layers, together with the beam pipe, are reported in Table 2.2.

After the upgrade planned for the LS2, the ITS will improve the impact parameter resolution (by a factor 3 and 6 in r and z direction, respectively), the tracking efficiency, the transverse momentum resolution and the readout capabilities [45]. The improvement of the impact parameter resolution will be possible by placing the first ITS layer at 22.4 mm from the beam line (instead of 39 mm) as well as by reducing the total material budget per layer: the usage of Monolithic Active Pixel Sensors and the optimization of front-end electronics can reduce it for the three innermost layers. Both the impact parameter at high p_{T} and the transverse momentum resolution will be improved by increasing the detector segmentation. Finally the tracking efficiency and the p_{T} resolution will be further improved by increasing the number of detector layers from six to seven.

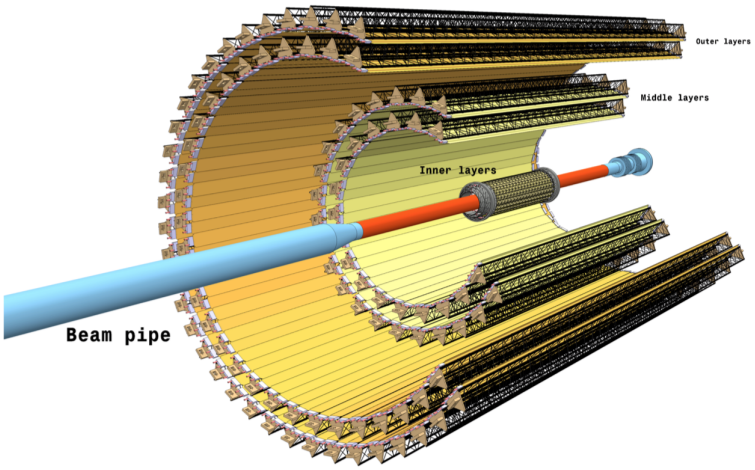

Figure 2.5: Layout of the new ITS consisting of 3 inner and 4 outer barrel layers [44].

In Figure 2.5 the layout of the 7-layer barrel geometry based on CMOS Pixel Sensors is shown. The ITS readout system will be composed of 192 electronic boards (Read-out Units) located 5 m from the detector. No analogue readout will provide $\mathrm{d}E/\mathrm{d}x$ measurements for particle identification in ITS, but PID will be performed in TPC.

Time Projection Chamber

The Time Projection Chamber (TPC) is the main tracking detector of the central barrel. It is optimised to provide charged particle momentum measurements with good two-track separation, particle identification via $\mathrm{d}E/\mathrm{d}x$ and vertex determination. In Figure 2.6 a schematic view of the ALICE TPC is shown. Particles produced in the collision traverse the TPC volume producing free electrons by ionisation which drift in an electric field generated by a central cathod and anods placed at the endcaps where they are detected by Multi-Wire Proportional Chambers (MWPCs). The acceptance is $|\eta| < 0.9$ for tracks that traverse entirely the TPC. For tracks with reduced track length and, hence, reduced momentum resolution, an acceptance up to about $|\eta| < 1.5$ is accessible. The total ALICE TPC active volume has an inner radius of about 85 cm (constrained by the maximum acceptable hit density), an outer radius of about 250 cm (constrained by

Layer/Type	**r [cm]**	**± z [cm]**	**Modules**	**Active area[m²]**
Beam pipe	2.94	-	-	-
1/pixel	3.9	14.1	80	0.07
2/pixel	7.6	14.1	160	0.14
3/drift	15.0	22.2	84	0.42
4/drift	23.9	29.7	176	0.89
5/strip	38.0	43.1	748	2.20
6/strip	43.0	48.9	950	2.80

Table 2.2: Characteristics of the six ITS layers and the beam pipe.

the requirement to achieve a $\mathrm{d}E/\mathrm{d}x$ resolution better than 5-7%) and a total length along the beam direction of 500 cm. During the LHC Run 1, the TPC was filled with a gas mixture composed of Ne and CO_2 (90-10), while during the LHC Run 2 it was changed to a mixture of Ar and CO_2 (88-12). The addition of 5% N_2 has also been successfully tried out. Note that the choice of the gas mixture is crucial for the detector performance. It is governed by several factors: low working voltage, high gain, good proportionality and high rate capability. Since they require the lowest electric field to form the avalanche, noble gases are usually chosen in order to optimise drift velocity and to ensure multiple scattering and secondary particle production. To absorb photons originating from ionization processes a certain amount of an inorganic gas, e.g. CO_2, is added to the noble gas allowing to maximise the detector gain [46]. The field cage is operated at high voltage gradients of about 400 V/cm, with a high voltage of 100 kV at the central electrode.

In Pb-Pb runs the TPC can be operated at central collision rates of up to 8 kHz. Due to typical drift velocities of electrons (about 2.7 cm/μs) which lead to maximum drift time of 88 μs, ALICE can not afford high interaction rates and therefore the luminosity in proton-proton collisions has been reduced by displacing the proton beams or using main-satellite collisions. In order to conduct the envisaged physics programme with

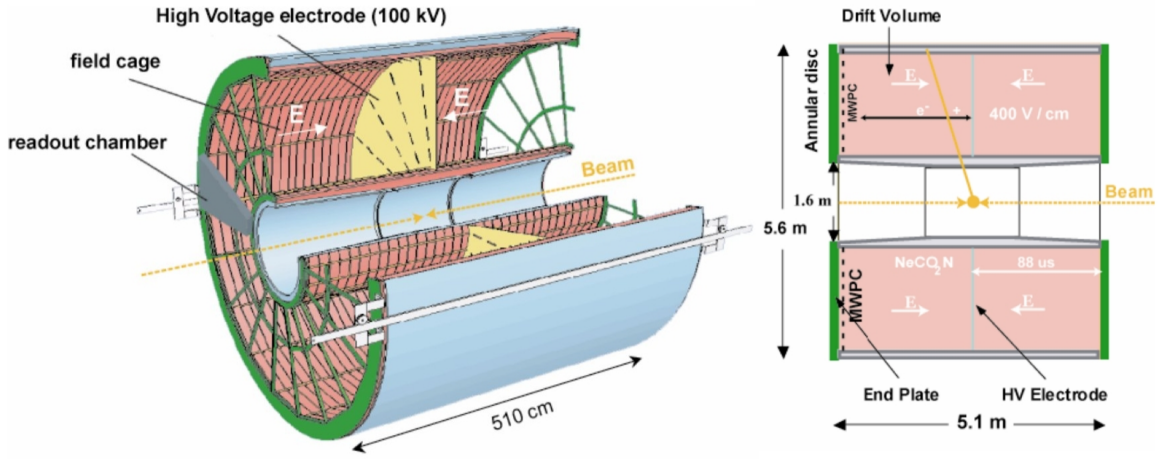

Figure 2.6: 3D schematic view of the ALICE TPC (left) and some details concerning the field cage (right) [44].

optimal precision and exploit the full LHC luminosity, the TPC will be upgraded for the LHC Run 3 scheduled for 2020-2022 and Run 4 scheduled for 2026-2029. This upgrade is intended primarily to overcome the rate limitation of the present system, which arises from the gated operation of the MWPC-based readout chambers [47]. The proposed new scheme therefore entails replacement of the existing MWPC-based readout chambers by a multi-stage Gas Electron Multiplier (GEM) system. GEMs feature intrinsic ion blocking without additional gating and exhibit excellent rate capabilities, therefore they enable the TPC to operate in a continuous, ungated readout mode at collision rates of 50 kHz. The TPC upgrade allows the increase of the readout rate by about two orders of magnitude as compared to the present system. This implies also the replacement of the front-end electronics, while the existing field cage as well as most of the services of the present TPC will remain.

Time-Of-Flight Detector

The Time-Of-Flight (TOF) detector provides identification of charged particles in the momentum range from 0.3-0.5 GeV/c to 3.5 GeV/c, via the measurement of the time

of flight which is combined with the information about tracks momenta from TPC. Especially, it allows a 3σ K/π and K/p separation below p $\sim$ 2.5 GeV/c and up to p $\sim$ 4 GeV/c, respectively [48]. The TOF, sketched in Figure 2.7, is located in the central barrel and covers an area of 140 m^2 at a radius close to 4 m (internal radius: 3.7 m) for an overall logitudinal length of 7.45 m. It covers the central pseudorapidity region ($|\eta| < 0.9$) and the full azimuthal angle. TOF is based on Multi-gap Resistive-Plate Chambers (MRPCs) with intrinsic time resolution of $\sim$ 50 ps. The key aspect is that the electric field is at the same time high and uniform over the whole sensitive gaseous volume of the detector. Any ionization produced by a traversing charged particle immediately starts a gas avalanche process which enables to catch signals on the pick-up electrodes. The basic unit of the TOF is a 5 gaps/stack MRPC strip, 122 cm long and 13 cm wide, with an active area of 120 x 7.4 cm^2. The strips are placed in gas-tight modules which are positioned transversely to the beam direction. The detector has a modular structure corresponding to 18 sectors in ϕ and to 5 modules per sector along the z direction. Every module of the TOF consists of a group of MRPC strips (15 in the central, 19 in the intermediate and external modules) closed inside a box that supports the external front-end electronics. The complete TOF system is composed of 1638 MRPC strips. Each strip is segmented in 92 pads, each of which is read out by a channel, for a total of 157 248 read out channels in the whole TOF.

During the LHC Runs 3 and 4, the foreseen operation of the TOF detector at Pb-Pb collision rates of 50 kHz (made possible by the upgrade of the TPC) defines new running conditions in terms of charged particle flux in the MRPCs as well as new requirements on data rates in the readout electronics. MRPCs showed that this rate can be easily sustained, therefore for the ALICE upgrade programme the focus will be to further increase the readout rate capability for both Pb-Pb and pp interactions, while the detector will not be upgraded. For a more detailed discussion of the rate limitations of the current TOF redout electronics, see [43].

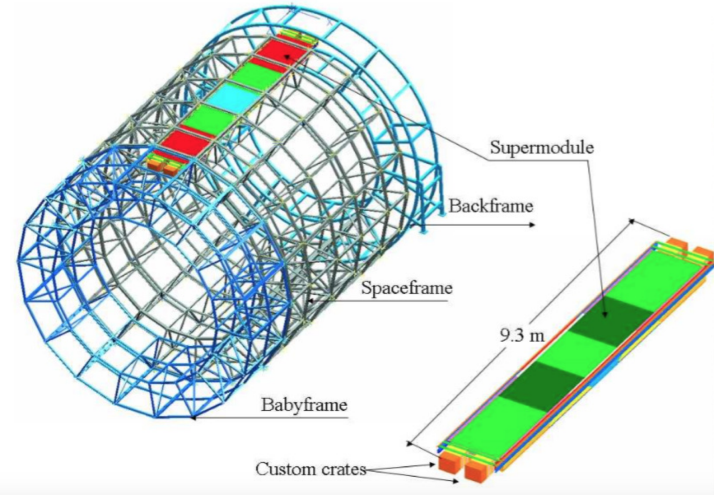

Figure 2.7: Schematic view of the modular structure of ALICE TOF with a drawing of a supermodule [44].

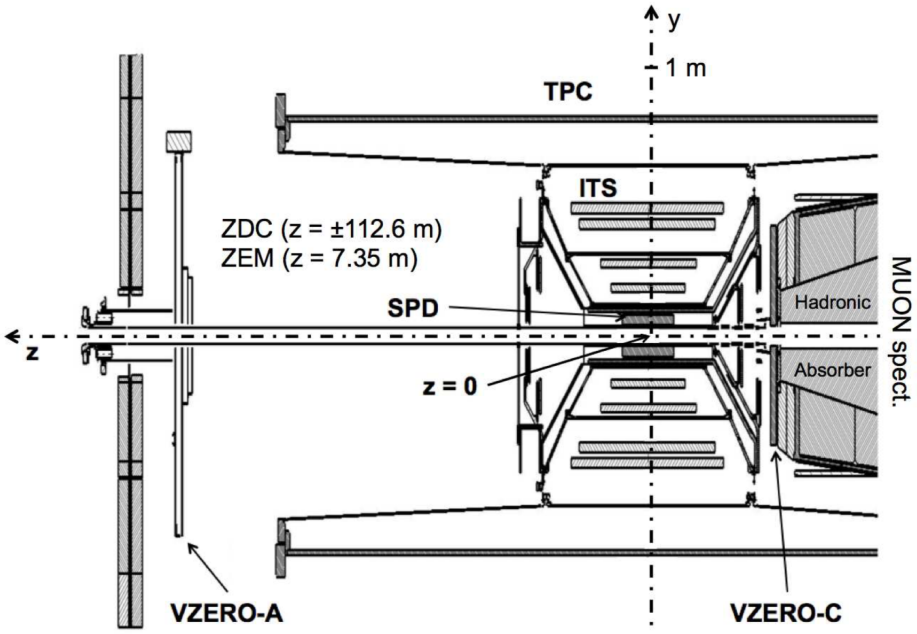

Figure 2.8: Position of the two VZERO arrays within the general layout of the ALICE experiment [49].

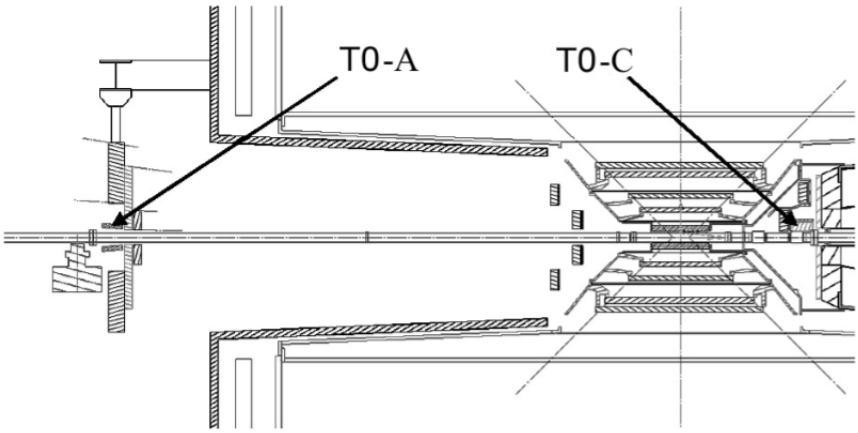

Figure 2.9: The layout of the T0 detector arrays inside ALICE [50].

2.2.2 Forward detectors

V0 - The V0 detector consists of two arrays of plastic scintillator counters, called V0C and V0A, which are located on each side of the ALICE ITS detector. The V0C is located at 90 cm from the interaction point on the muon spectrometer side, covering the pseudo-rapidity range -3.7 $< \eta <$ -1.7, while the V0A is located at 340 cm on the opposite side, covering the pseudo-rapidity range 2.8 $< \eta <$ 5.1. The detectors are segmented in 64 elementary counters and distributed in 8 rings. The position of the two VZERO arrays inside ALICE is shown in Figure 2.8.
The V0 detector is used for the minimum bias trigger selection in Pb-Pb and pp collisions and for the rejection (offline) of beam-gas interactions through the measurement of the time difference between signals in V0C and V0A. In addition, it is used for selecting centrality classes in nucleus-nucleus collisions and multiplicity classes in p-Pb and pp, since the signal amplitude measured in V0 detectors is proportional to the particle multiplicity. V0 shows a resolution of better than 1 ns [49].

T0 - The start time for the measurement of time of flight can be determined with several methods, one of which is using the time-zero given by the T0 detector [50]. This

timing signal is independent of the position of the vertex and corresponds to the real time of the collision (plus a fixed time delay). T0 consists of two arrays (T0A and T0C) of Cherenkov counters, 12 per array, located at 375 cm and -72.7 cm from the nominal interaction point, respectively. Its layout is shown in Figure 2.9. It is a detector based on Quartz Cherenkov technology: for each counter there is a fine-mesh photomultiplier tube, optically coupled to a quartz radiator. The pseudorapidity coverages are -3.28 $< \eta <$ -2.97 and 4.61 $< \eta <$4.92, respectively. T0 is also used to measure the vertex position (with a precision $\pm$1.5 cm) for each interaction and to provide a level 0 trigger. T0 provides a start time resolution of better than 50 ps. Regarding the ALICE upgrade, the goal is to have a single detector system able to provide all the required functionality [43].

2.3 From collisions to data analysis

2.3.1 The ALICE trigger and data acquisition

The task of ALICE Trigger, Data AcQuisition (DAQ) and High-Level Trigger (HLT) systems is to collect data from individual detectors, build the event, select the interesting events for physics analysis. Due to the variety of physics observables ALICE is studying with different beam conditions, a large number of trigger classes are used to select the events of interest. In figure 2.10 a schematic representation of the online architecture structure is reported. In the following a brief description of each component is provided.

The ALICE Central Trigger Processor (CTP) is designed to respect the restrictions imposed by the bandwidth of the DAQ and the HLT. A 3–level trigger system has been deployed in ALICE to comply with the different readout times and trigger latencies of the large variety of detectors of the experimental apparatus. The fast part of the trigger is split in two levels: a Level 0 (L0) signal (L0 delay = 1.2 μs) and a Level 1 (L1) signal (L0 to L1 delay = 6.5 μs). L0 and L1 are complementary because the first is too fast to receive all the trigger inputs. CTP decisions are taken in 100 ns, the rest of the L0 latency comes from the generation time of the trigger signals and cable delays. In order to verify that the event can be recorded, a final level of trigger (Level 2, L2) waits for the

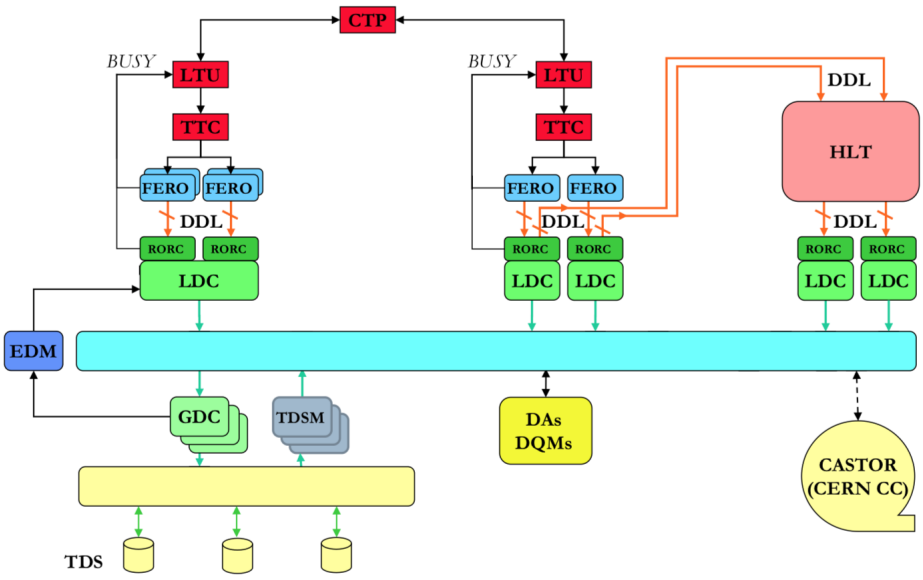

Figure 2.10: Schematic view of the ALICE online structure [51].

end of the past-future protection interval. The latter is a security tool designed to ensure that the events are not contaminated by pile-up, considering the maximum time over which two signals from two different collisions could overlap (88 μs). Trigger conditions can be defined by a logic involving three states of the inputs (asserted, negated, not relevant), coupled by ANDs. The definition of an *interaction*, the basis of the minimum bias trigger, needs an OR of different detector inputs, owing to lower trigger efficiencies in pp interactions because of lower multiplicities. For instance, for the analysis presented in this thesis, events selected with a minimum bias trigger were used. The minimum bias trigger was in that case defined as the OR of a V0A and V0C, namely requiring a hit in one of the two scintillator arrays.

ALICE DAQ has two main architectural features:

- *All the detectors are interfaced to the ALICE-standard Detector Data Links (DDLs).* More specifically, the CTP communicates with each detector via a 6 units VME Local Trigger Unit (LTU) linked to a Timing, Trigger and Control (TTC) system. The Front-End Read-Out (FERO) electronics of the detectors is directly interfaced

to the DDLs, hence data produced by the detectors are injected on the DDLs with a uniform protocol.

- *The event builder is based upon an event-building network.* After DDLs there are DAQ Redout Receiver Cards (D-ROCK) which essentially are PCI-X based electronic modules. They are hosted by the front-end machines, called Local Data Concentrators (LDCs): the event fragments originated by the various D-ROCKs are logically assembled into sub-events in the LDCs, whose role is to ship them to a farm of machines called Global Data Collectors (GDCs) where the whole events are built. The event-building network does not have a decision-making role, but it is a standard communication network supporting the TCP/IP protocol.

For more details on ALICE DAQ, see [41].

The HLT consists of a PC farm of up to 1000 multi-processors computers: data processing is carried out by parallel software components on the nodes of the computing cluster. Since the DAQ archiving rate is about 1GB/s (much lower compared to the data rate for all ALICE detectors which can easily reach up to 25GB/s after a trigger selection), it is necessary to filter relevant events with an on-line process and to reduce the event size without loss of physics information. The raw data of all ALICE detectors are received via 454 DDLs. Before the event reconstruction, which is done for each detector individually, data are clustered. The next step after the reconstruction is the combination of the processed and calibrated information of all detectors with the aim of selecting events or regions of interest, based on run-specific physics selection criteria. Selected data, finally subjected to complex data compression algorithms, are objectified and then recorded in the Transient Data Storage (TDS) before being sent to CERN Advanced STOrage Manager (CASTOR) via the offline infrastructure. Sub-samples of data are processed online by dedicated Detector Algorithms (DAs) and Data Quality Monitoring (DQM) modules in order to provide quality assurance checks and perform basic calibration, to be followed by the full offline procedures.

2.3.2 Offline computing

Such a complex experiment needs the development of a sophisticated framework for data processing. The ALICE offline framework (AliRoot, Figure 2.11) is an object-oriented software based on the ROOT framework [52]. AliRoot gives the user the flexibility to perform Monte Carlo simulation, data reconstruction, calibration and analysis with the same tool. Simulation, reconstruction or analysis *jobs* can be processed by splitting them in many identical *sub-jobs* that run in parallel on different computer nodes of the Grid, which is a worldwide distributed computing infrastructure of shared resources adopted by CERN to manage the enormous flow of data produced by the LHC. His nature is highly hierarchical: all data originate from CERN and are stored in a very large computing centre called Tier-0. Large regional computing centres called Tier-1 aim to ensure a safe storage of the data. Smaller centres, called Tier-2, are logically clustered around the Tier-1's. Thanks to the Grid the community of physicists is allowed to access data in almost real time from all over the world. The ALICE Collaboration has developed the AliEn (ALICE Environment) framework to handle reconstruction and analysis activities as well as to provide a user interface and catalogue for the data. Indeed, AliEn provides a global file system for data storage and an interface to execute the *jobs* on the Grid.

Simulation in the AliRoot framework

One of the main purposes of the analysis framework is to simulate the physics events as well as the resulting detector response: simulations play a very important role in evaluating the performance of the experimental setup. Thanks to external event generators (HIJING [53], DPMJET [54] and PYTHIA [55]) whom AliRoot is interfaced to, it is possible to simulate the collision events and the associated particles.
Particles are transported through the detector via GEANT3 [56] which allows to simulate the detector response generating *hits*. Information on their position, time, energy deposit, etc., are assigned to each hit. Combining the detector and the electronic response information, a digital output is produced for each hit and stored as a *summable digit*. Once noise and realistic thresholds are applied, the final product is translated in

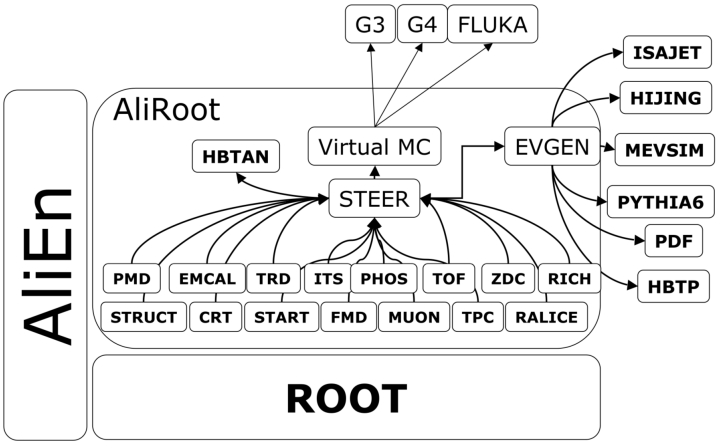

Figure 2.11: Schematic representation of the structure of the ALICE offline framework, AliRoot [51].

a comparable-to-real-raw-data format.

Reconstruction

The event reconstruction consists of different steps: primary vertex reconstruction, cluster finding, track and secondary vertex reconstruction. The tracking algorithm is schematically summarized in Figure 2.12.

The first step is a local reconstruction: clusterization is performed separately for each detector. A hit produced by a particle crossing the active volume (or by a shower in the calorimeters) corresponds to an energy deposit. Single elements are combined to better reduce the effect of the random noise. Groups of adjacent firing detector elements are known as *clusters* and are characterized by position, signal amplitudes and times, shapes and their associated errors. Clusters are used as input for track reconstruction operations.

The second step is the reconstruction of the interaction vertex position. Using hits on the first two layers of the ITS (SPD), the algorithm builds a set of track segments (*tracklets*), connecting the clusters of the two layers within an azimuthal acceptance window. The point in the space minimising the distance from all the tracklets is then computed and

the outliers are removed. The resulting space point corresponds to the primary vertex. In pp collisions it is not unusual to get only one tracklet: because of the reconstruction of the 3D position of the primary vertex requires at least two tracklets, in this case the z position of the primary vertex can be still computed using as a constraint the beam line position in the transverse plane.

The third step is the tracking phase. Track finding and reconstruction are implemented simultaneously with a Kalman filter algorithm [57] which allows one to predict the subsequent steps, to combine the prediction with the measurements of the next track parametrisation, known as *state vector*, and to repeat prediction and filtering steps as many times as measurements of the state vector are performed. Starting from a track *seed* built using the SPD primary vertex and pairs of TPC clusters in adjacent pad rows, the first track candidate is identified. Track seeds are projected inward. Track candidates are updated at each propagation step with the nearest TPC cluster until the inner radius of the TPC is reached. To decide which cluster is to be next associated to the track, a geometrical *window* is defined around the point where the track is expected to be according to the actual parameters. The size of the window depends on the uncertainty on the track position. At this point a preliminary particle identification based on TPC $\mathrm{d}E/\mathrm{d}x$ is performed to be used to calculate the energy loss correction in the next steps. Out from the TPC, the track is prolonged to the ITS. From the inner detector the tracks are propagated outwards: clusters found during the previous step are used until the tracks arrive at the outermost radius of the TPC. From here the tracks are prolonged to TRD (where eventually other clusters are added), TOF, HMPID, EMCAL and PHOS (which provide PID information but don't update the track parameters). It is then possible to go ahead with the track length calculation.

As the last step, reconstructed tracks are re-fitted inward to best determine track parameters and the convariance matrix. Finally, they are propagated to their Distance of Closest Approach (DCA) to the SPD vertex. Once all the tracks have been reconstructed, they are used to find vertices coming from secondary interactions.

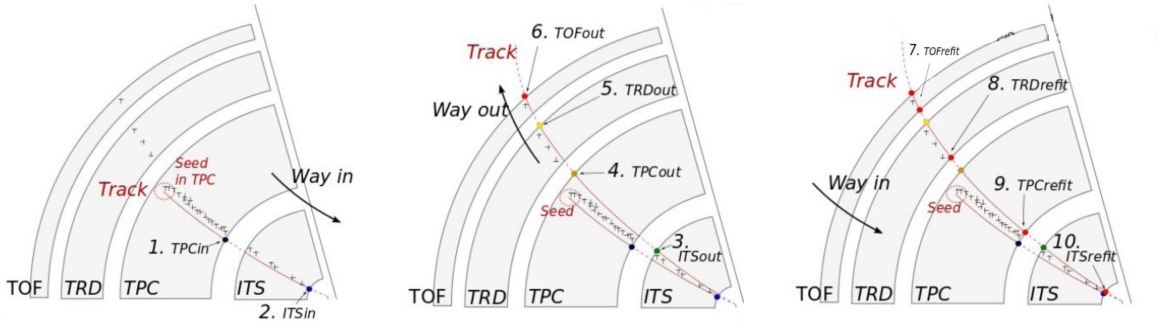

Figure 2.12: Tracking procedure performed with ITS, TPC, TRD and TOF. Using the Kalman Filter algorithm, tracks start being propagated inward (1, 2). The found tracks are then propagated outward and matched to tracklets of the TRD, TOF clusters and signals in EMCal, PHOS and HMPID (3, 4, 5, 6). Information is updated at each step. The final step of the procedure is the inward refitting which allows the track reconstruction (7, 8, 9, 10). At each step flags are associated with the track that can be used to access tracking information at the analysis level.

Calibration

The quality of the reconstructed data critically depends on the quality of the calibration used in the reconstruction. Calibration is needed in all the steps of the reconstruction chain. Objects obtained after these procedures are stored in an Offline Condition Database (OCDB). Online calibration procedures are performed via *Shuttle*, while a more refined calibration is executed offline via automatic calibration passes (CPass0, CPass1) or via *manual analysis*. Once full data set are available, the Offline Analysis Data Base (OADB) objects are produced asynchronously with respect to reconstruction pass that are needed at the analysis level. Among others, they include splines to parametrise the expected TPC $\mathrm{d}E/\mathrm{d}x$ for various particle species, centrality/multiplicity percentiles from various estimators, event plane flattening corrections. Further information about calibration procedures can be found in [58].

As final product of the reconstruction and calibration procedures/passes, the data are provided to users in the format of Event Summary Data (ESD) or, after a further skim-

ming, as Analysis Object Data (AOD), These contain further information on full events, including primaary vertex, tracks, reconstructed weak decay topologies, and more. ESDs or AODs are the input for the analysis framework. The analysis presented in this thesis has been carried on with AliRoot framework together with a custom analysis code, and run on the Grid.

Chapter 3

Hadronic resonances as probes of the system evolution

The process $A + B \rightarrow O \rightarrow C + D$ represents two initial particles colliding to form an unstable intermediate state, which then decays to the final state. Under the condition that the transition from $A + B$ to $C + D$ can proceed exclusively via the intermediate state, which indicates the *resonance*, the cross-section for the process is given by the Breit-Wigner formula:

$$\sigma_{i\rightarrow 0\rightarrow f} = \frac{\pi}{k^2} \frac{\Gamma_i \Gamma_f}{(E - E_0)^2 + \Gamma^2/4} \tag{3.1}$$

where Γ_i and Γ_f are the partial width of the resonance to decay to the initial $(A + B)$ and to the final $(C + D)$ states, respectively; Γ is the full width of the resonance, E is the centre-of-mass energy of the system, E_0 is the characteristic rest mass energy of the resonance, k is the wave-number of the incoming projectile in the centre-of-mass frame.

Resonances are particles with higher mass than the corresponding ground state particle with the same quark content. Hadronic resonances decay strongly, with a short lifetime $\tau \sim$ of few to few tenths of fm/c. The natural width is inversely proportional to the lifetime and it is given by

$$\Gamma = \frac{\hbar}{\tau} \tag{3.2}$$

.

After being produced, broad states can be measured by reconstructing their decay products (*daughters*) in a detector. The study of hadronic resonance production plays a pivotal role both in elementary and in heavy-ion collisions: resonances and their decay products strongly interact throughout the hadronic phase, thus if one wants to experimentally verify the existence and duration of that phase, the study of their production and absorption rates represents a useful tool. With their properties (mass, width, yield and momentum distribution), resonances provide information about the different stages of the system evolution expansion [59]. In order to extract the essential properties of the fireball produced after the interaction, a vast variety of macroscopic and microscopic models have been developed for hadronic and nuclear collisions [60]. In the following section, we focus and briefly introduce the statistical-thermal model and the Ultra-relativistic Quantum Molecular Dynamics (UrQMD) model, as they are commonly employed to investigate resonance production in heavy-ion collisions.

3.1 Particle production in heavy-ion collisions

The idea of using a statistical approach to solve multi-particle production problems in high energy collisions arose in 1950, when Enrico Fermi [61] suggested that particles originated from an excited region evenly occupy all available phase space states. Even if far from the original models, it is acknowledged that *thermal models* can be used to predict particle yields (and ratios) once given the chemical freeze-out temperature T_{ch} [62]. As previously explained, in ultra-relativistic heavy ion collisions, the knowledge of the critical energy density ϵ_c required for deconfinement as well as the equation of state (EoS) of strongly interacting matter are of particular importance. Knowing the value of ϵ_c allows us to establish the necessary initial conditions to possibly create the QGP, whereas the EoS is required as an input to describe the space-time evolution of the fireball after the collision. Below T_C, quarks and gluons are confined within hadrons, thus the EoS is well parameterized by a hadron resonance gas. Above T_C, the system is in the QGP phase. If QGP formation is assumed in the initial state of the

collisions, it is expected that the thermal nature of the partonic medium is preserved during hadronization. Consequently, the particle yields measured in the final state should resemble a thermal population. Equilibrium is preserved if the final state is reached within the hadronic phase [63].

The partition function $Z(T,V)$ is the basic quantity required to compute the thermal composition of particle yields produced at hadronization. In the Grand Canonical (GC) ensemble,

$$Z^{GC}(T,V,\mu_Q) = Tr[e^{-\beta(H-\sum_i \mu_{Q_i} Q_i)}], \tag{3.3}$$

where H is the Hamiltonian of the system (usually taken such as to describe a hadron resonance gas), $\beta = \frac{1}{T}$ is the inverse temperature, Q_i are the conserved charges and μ_{Q_i} are the chemical potentials that guarantee that the charges Q_i are conserved on the average in the whole system. GC formalism can be used because measurements refer only to a small portion of the system. Quantities like energy, baryon number, charge and isospin are conserved on average. The GC partition function of a hadron resonance gas can then be written as a sum of partition functions $ln\, Z_i$ of all hadrons and resonances

$$ln\, Z_i(T,V,\vec{\mu}) = \frac{V g_i}{2\pi^2} \int_0^\infty \pm p^2 dp ln[1 \pm \lambda_i exp(-\beta\epsilon_i)] \tag{3.4}$$

Here, for particle i of strangeness S_i, baryon number B_i, electric charge Q_i, spin-isospin degeneracy factor g_i, the chemical potentials are $\vec{\mu} = (\mu_B, \mu_S, \mu_Q)$ and $\epsilon_i = \sqrt{p^2 + m_i^2}$. The upper sign (+) is used for fermions, the lower (-) for bosons; $\lambda_i(T,\vec{\mu}) = exp(\frac{B_i\mu_B + S_i\mu_S + Q_i\mu_Q}{T})$ is the fugacity. Expanding the logarithm and performing the momentum integration in Eq. 3.4:

$$ln\, Z_i(T,V,\vec{\mu}) = \frac{VTg_i}{2\pi^2} \sum_{k=1}^{\infty} \frac{(\pm 1)^{k+1}}{k^2} \lambda_i^k m_i^2 K_2(\frac{km_i}{T}), \tag{3.5}$$

where K_2 is the modified Bessel function, (+) is used for bosons, (-) is used for fermions. From Eq. 3.5 the density of particle i is obtained:

$$n_i(T,\vec{\mu}) = \frac{\langle N_i \rangle}{V} = \frac{Tg_i}{2\pi^2} \sum_{k=1}^{\infty} \frac{(\pm 1)^{k+1}}{k} \lambda_i^k m_i^2 K_2(\frac{km_i}{T}) \tag{3.6}$$

$\langle N_i \rangle$, the average number of particles i in volume V and temperature T is, from Eq. 3.6:

$$\langle N_i \rangle(T, \vec{\mu}) \;=\; \langle N_i \rangle^{th}(T, \vec{\mu}) + \sum_j \Gamma_{j \to i} \langle N_j \rangle^{th,R}(T, \vec{\mu}) \tag{3.7}$$

In Eq. 3.7 two contributions can be recognized: the first defines the thermal average number of particles i, whereas the second defines the contribution to the yield of the species i coming from resonances decay. This term is a sum of all resonances which decay into particle i, each with $\Gamma_{j \to i}$ as decay branching ratio. Equation 3.7 also outlines the crucial dependencies of the observed particle yields on the temperature, volume and the three chemical potentials. In order to take into account the repulsion at short distances, the interaction of hadrons should be included in the partition function: after the implementation of excluded volume corrections [64], a shift of the baryon-chemical potential occurs. Note that the temperature in formulas above is the chemical freeze-out temperature (T_{ch}).

After hadronization hadrons keep rescattering with each other, subject to expansion flow, until the matter becomes so dilute that the average distance between hadrons exceeds the range of the strong interaction.
The Ultra-relativistic Quantum Molecular Dynamics (UrQMD) model [65] allows one to simulate the hadronic phase: hadron-hadron collisions are performed stochastically. Providing a large set of coupled partial integro-differential equations for the time evolution of the various phase space densities of particle species, UrQMD can be considered a Monte Carlo attempt of answering to a microscopic transport theory based on the covariant propagation of all hadrons on classical trajectories combined to stochastic binary scatterings, color string formation and resonance decays. A UrQMD collision term contains 55 different baryon species and 32 different meson species. According to UrQMD, particles interact if their distance satisfies:

$$d \leq d_0 = \sqrt{\frac{\sigma_{tot}}{\pi}} \tag{3.8}$$

where d is the relative distance between the two colliding particles and σ_{tot} the total cross section which depends on the centre-of-mass energy and on the species and quantum

numbers of the incoming particles. It has to be noted that at the point of closest approach, d is purely transverse respect to the relative velocity vector of the particles. The algorithm goes on according to Eq. 3.8: each particle is followed at the beginning of each time step. Because of the 4-dimensional curved trajectories in Minkowsky-space, at the beginning of each time step, d can be defined as:

$$d = \sqrt{\left(\frac{(q_n - q_m)^\nu (p_m + p_n)_\nu}{(p_n + p_m)^2} (p_n + p_m)^\mu - (q_n - q_m)^\mu \right)^2} \tag{3.9}$$

where q_ν and p_ν are the 4-vectors for the positions and momenta of the particles, respectively. The cross section of the two colliding particles does not depend on the reference frame of the nucleus-nucleus collision, while the dependence of the collision time on the reference frame of the reaction cannot be avoided. In the recent years UrQMD *hybrid* transport models [66] have been developed and employed aiming to describe the hadronic phase with a microscopic transport treatment based on the (re-)scattering of hadrons according to measured or calculated cross sections. They combine the advantages of a hadronic transport model with an intermediate hydrodynamical stage for the hot and dense phase of a heavy ion collision [67]. In [68] for instance, UrQMD is used to simulate how the hadronic interactions affect the final state observables. Results are for central collisions of Au-Au at $\sqrt{s_{NN}} = 200$ GeV (as at RHIC). In Figure 3.1 the hierarchy of resonance lifetimes is shown: the fraction of observable/reconstructible resonances which have decayed until a time t_D is reported as function of time. As expected, the short lived resonances decay at an earlier time ($\approx 1 - 10$ fm/c)whereas the ϕ meson decays at a very late time ($\tau \sim 40$ fm/c). These resonances have different lifetimes, but they also decay into different particles. The probability of the daughter particle rescattering depends on the time of the resonance decay and on the rescattering cross section of the daughter particles, which is different, for example, for pions, kaons and protons. Not all resonances decay at the same time, thus the detection probability for the different resonances will depend on their lifetime.

Generally, applications of this model in elementary pp and heavy-ion collisions can be useful in order to understand the medium effect during the evolution and expansion

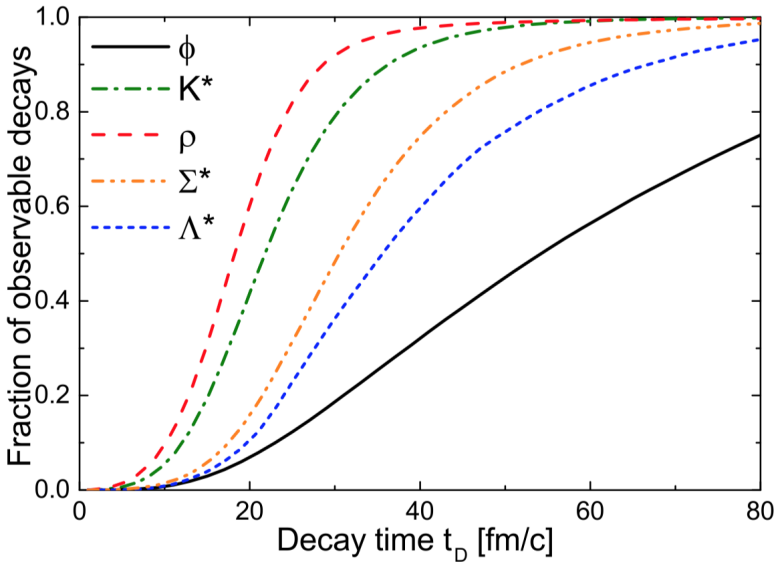

Figure 3.1: Fraction of observable resonances which have decayed until a time t_0 in Au–Au collisions at $\sqrt{s_{NN}} = 200$ GeV, from a hybrid UrQMD simulation [68].

of the fireball.

3.2 Resonance measurements in ALICE

As explained above, resonances can decay inside the hadronic medium, therefore the measured yields are the result of the effects of the interactions in the extended hadronic phase created in heavy-ion collisions. Since resonance lifetimes are of the same order of magnitude as the time span between the chemical (T_{ch}) and kinetic (T_{kin}) freeze-out, typically estimated to be about 10 fm/c for central collisions, they are good probes to investigate the properties of the hadronic medium in the time lapse between T_{ch} and T_{kin}. If the hadronic phase lasts long enough, the decay daughters of very short-lived resonances experience its full evolution: on one side, the rescattering via elastic collisions could modify or destroy their correlations, hence resulting in a lower yield of the reconstructible resonances. On the other hand, depending on the density and on

the time scale of the hadronic medium, hadrons could interact pseudo-elastically to form resonances: this mechanism feeds the system with more particles, thus it increases the resonance yields [69]. Several hadronic resonances have been measured using the ALICE detector in different collision systems and at different energies. In Table 3.1, the main properties (mass, decay width, valence quark content, decay mode and corresponding branching ratio) of the resonances whose production is (or has been in the recent years) measured are listed. For instance, it has been shown recently that the yields of $\mathrm{K}^*(892)^0$ are suppressed in central Pb-Pb collisions with respect to pp and peripheral Pb-Pb collisions, while the longer lived $\phi(1020)$ meson is not suppressed [70]. In Figure 3.2 K^{*0}/K^- and ϕ/K^- ratios as a function of $\langle dN_{ch}/d\eta \rangle^{1/3}$ measured at mid-rapidity in pp collisions at $\sqrt{s} = 2.76$ TeV and 7 TeV, and Pb-Pb collisions at $\sqrt{s_{\mathrm{NN}}} = 2.76$ TeV are reported [70]. The predictions from a GC thermal model with a chemical freeze-out temperature of 156 MeV are also shown. The observed suppression of the $\mathrm{K}^{*0}/\mathrm{K}^-$ is understood as due to the rescattering of the decay products in the hadronic medium dominating over regeneration. The ϕ/K^- ratio does not exhibit suppression for central collisions, nor any significant trend with centrality. This feature suggests that the ϕ, which has a lifetime of one order of magnitude larger than that of K^{*0}, might decay predominantly outside the hadronic medium.

3.3 The $\mathrm{f}_0(980)$ resonance

The channel with the vacuum quantum numbers $J^{PC}I^G = 0^{++}0^+$ has several resonances, whose structure has been under discussion for a long time. From the experimental point of view, because of their large decay widths which imply a significant overlap between the true signal and the remaining background, the identification of the scalar mesons is a long-standing puzzle. Furthermore, different decay channels sometimes open up within a short mass interval (e.g., at the $K\bar{K}$ thresholds), producing cusps in the line shapes of the near-by resonances [71]. $\mathrm{f}_0(980)$ represents a highly contested example of a scalar meson.

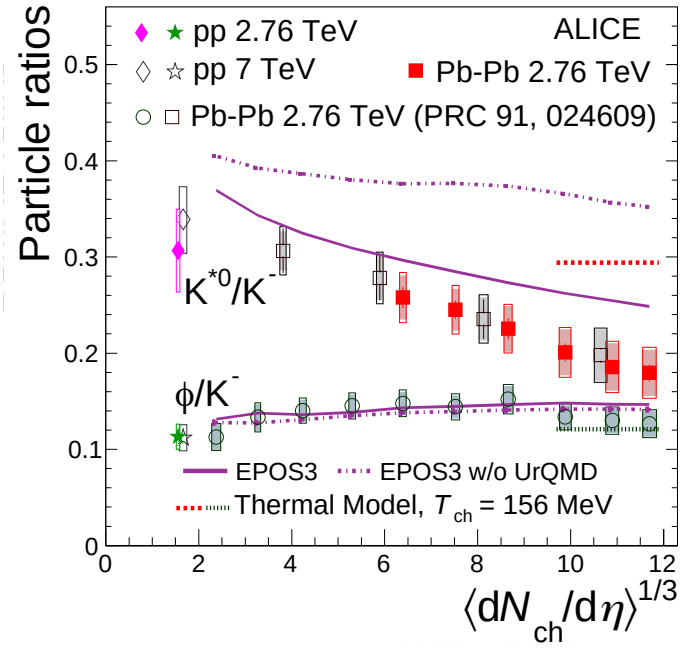

Figure 3.2: K^{*0}/K^{-} and ϕ/K^{-} ratios as a function of $\langle dN_{ch}/d\eta\rangle^{1/3}$ measured at mid-rapidity in pp collisions at $\sqrt{s} = 2.76$ TeV and 7 TeV, and Pb-Pb collisions at $\sqrt{s_{\rm NN}} = 2.76$ TeV. Bars represent the statistical uncertainties, empty boxes represent the total systematic uncertainties, and shaded boxes represent the systematic uncertainties that are uncorrelated between centrality classes. The expectations from a thermal model calculation with chemical freeze-out temperature of $\mathrm{T}_{ch} = 156$ MeV for the most central collisions are shown [70].

Resonance	**m[MeV]**	**Γ[MeV]**	**Composition**	**Decay mode**	**BR[%]**
$\rho(770)^0$	775.26 ± 0.25	149.10 ± 0.80	$(u\bar{u}+d\bar{d})/\sqrt{2}$	$\pi^+\pi^-$	100
$K^*(892)^0$	895.81 ± 0.19	47.40 ± 0.60	$d\bar{s}$	$K^+\pi^-$	66.60
$\phi(1020)$	1019.46 ± 0.02	4.27 ± 0.03	$s\bar{s}$	K^+K^-	48.90
$\Delta(1232)^{++}$	1232.00 ± 2.00	118.00 ± 4.00	uuu	π^-p	99.40
$\Sigma(1385)^+$	1382.80 ± 0.35	36.00 ± 0.70	uus	$\Lambda\pi^+$	87.00
$\Lambda(1520)$	1519.53 ± 0.19	15.64 ± 0.29	uds	K^-p	22.50
$\Xi(1530)^0$	1531.80 ± 0.32	9.10 ± 0.50	uss	$\Xi^-\pi^+$	66.70

Table 3.1: Hadronic resonances with their mass, decay width, valence quark content, decay mode exploited for the measurements with ALICE and corresponding branching ratio (BR) [7].

Decay modes	**Fraction** $[\Gamma_i/Gamma]$
$\pi^+\pi^-$	Dominant
$K\bar{K}$	Seen
$\gamma\gamma$	Seen

Table 3.2: $f_0(980)$ decay modes as in [7].

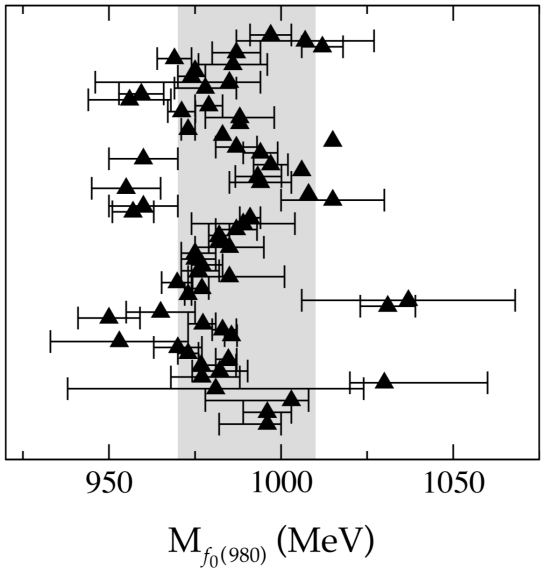

Figure 3.3: Values of the $f_0(980)$ masses from the currently quoted mass estimates (see [71]). The newest measurements appear at the bottom, the oldest on the top.

The Particle Data Group only provides ranges where $f_0(980)$ mass and width estimates have been identified. More specifically, the mass value and the full width range reported are, respectively:

$$m = 990 \pm 20 \text{ MeV} \tag{3.10}$$

$$\Gamma = \text{ from 10 to 100 MeV} \tag{3.11}$$

In Fig. 3.3 the values of $f_0(980)$ masses are shown. In Table 3.2 the different decay modes with their fraction (Γ_i/Γ) are listed.

3.4 $f_0(980)$ nature: resonance or multi-quark state?

Despite a long history of experimental and theoretical studies, the nature of the short-lived $f_0(980)$ resonance is far from being understood: up to now there is no agreement about its quark structure. By assuming a simple excited quark plus anti-quark configuration with a mixture of strange and light components, $f_0(980)$ belonging to the scalar

meson nonet, which is shown in Figure 3.4, is controversial. In the $q\bar{q}$ model, the mixing between the two $I = 0$ light scalar mesons, $f_0(500)$ and $f_0(980)$, is parametrized by a normal 2×2 rotation matrix characterized by the angle α. Thus, the flavor structure of these scalar mesons would generically be

$$|f_0(980)\rangle = cos(\alpha)\,|s\bar{s}\rangle + \frac{1}{\sqrt{2}} sin(\alpha)(|u\bar{u}\rangle + |d\bar{d}\rangle) \tag{3.12}$$

$$|f_0(500)\rangle = -sin(\alpha)\,|s\bar{s}\rangle + \frac{1}{\sqrt{2}} cos(\alpha)(|u\bar{u}\rangle + |d\bar{d}\rangle) \tag{3.13}$$

In this configuration the scalar meson nonet does not follow the same mass ordering as the vector meson nonet [72]. Furthermore, in the mass range below 2 GeV, in which theoretically one expects non-$q\bar{q}$ scalar objects like *glueballs* and *multiquark states*, there are too many 0^{++} mesons observed to be explained as $q\bar{q}$ states [73]. Multiquarks have been justified to coexist with $q\bar{q}$ states in the energy region around 1 GeV because they can couple to $0^{++}$by avoiding penalty due to orbital excitation [74]. Scalar mesons are strongly affected by their coupling to open hadron channels. The fact that the $f_0(980)$ couples to both $\pi\pi$ and KK channels means that virtual hadron loop contributions are important. As a consequence, conventional $q\bar{q}$ states are expected to mix with four-quark $qq\bar{q}\bar{q}$ states to yield physical mesons[1].

Some bag model calculations [74] in which the light scalar mesons are good candidates for tightly bound $(q)^2(\bar{q})^2$ systems, allow to view $f_0(980)$ as a closely bound 4-quarks structure. Additional arguments have been added by N.N. Achasov in favour of the 4-quark nature of $f_0(980)$ meson on the basis of the interpretation of the experimental data on the decays $\phi \to \gamma\pi^0\pi^0, \gamma\pi^0\eta$ [76]: the four-quark structure of $f_0(980)$ would avoid the underestimation of the partial width obtained in the case of a pure $q\bar{q}$ component. Therefore diquark-antidiquark bound states naturally reproduce the SU(3)

[1] A color singlet four-quark state can be obtained in two different coupling schemes: $[(qq)(\bar{q}\bar{q})]$ or $[(q\bar{q})(q\bar{q})]$. In the first case the singlet color states are obtained from the $[(q \bigotimes q)_6(\bar{q} \bigotimes \bar{q})_{\bar{6}}]$ (the subindex is standing for the color state) and $[(q \bigotimes q)_{\bar{3}}(\bar{q} \bigotimes \bar{q})_3]$ couplings, whereas in the second case the total singlet color states are driven by $[(q \bigotimes \bar{q})_1(q \bigotimes \bar{q})_1] = (MM)$ which is interpreted as a molecule of mesons, and $[(q \bigotimes \bar{q})_8(q \bigotimes \bar{q})_8] = (QQ)$ which is interpreted as a compact component that is not factorizable into singlet color meson-meson channels.

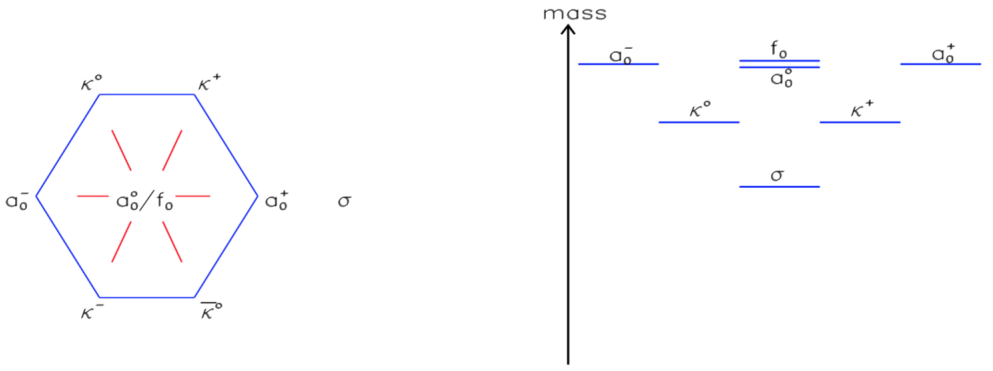

Figure 3.4: The light scalar meson nonet (left) and its mass hierarchy (right) [75].

nonet structure with the correct mass ordering [77]. Unfortunately, the tetraquark interpretation raises new questions about the radial excitations of the 2-quark states. A $K\bar{K}$ molecule configuration is also possible due to the $f_0(980)$ meson lying relatively close to the $K\bar{K}$ mass threshold, at 987 MeV/c^2. Although explaining the degeneracy of $f_0(980)$ with the $K\bar{K}$ threshold, it would lead most likely to incomplete multiplets [77]. A crucial test of the scalar mesons structure would be the study of two-photon decay widths of neutral scalars, which is dominated by the $q\bar{q}$ component of the wave function (the four-quark component is known to give a small contribution) and which is still lacking. To conclude, the inverted mass spectrum of the light scalar nonet and the nature of the $f_0(980)$ is still an open topic. The final answer could only be obtained from precise experimental data that would allow to discriminate between the predictions of different theoretical models.

3.5 Existing measurements of $f_0(980)$ production

The OPAL Collaboration [78] measured the inclusive production of $f_0(980)$ by using a sample of 4.3 million hadronic Z^0 decays recorded at LEP 1 [79] between 1990 and 1995. The study, published in [80], exploits the two decay channels $f_0 \to \pi^+\pi^-$ and $f_0 \to K^+K^-$. Mass spectra were fitted simultaneously with $f_2(1270)$ and $\phi(1020)$ resonances,

to a sum of contributions given by:

$$f(m_{\pi^+\pi^-}) = a_{f_0}^{\pi^+\pi^-}|A_{f_0}(m_{\pi\pi})|^2 + a_{f_2}BW_{f_2} + a_{bgd}^{\pi^+\pi^-}B_{\pi^+\pi^-} \tag{3.14}$$

$$f(m_{K^+K^-}) = a_{f_0}^{K^+K^-}|A_{f_0}(m_{KK})|^2 + a_{\phi}BW_{\phi} + a_{bgd}^{K^+K^-}B_{K^+K^-} \tag{3.15}$$

In Eq. (3.14) and (3.15), the a terms represent the intensities to be fitted, A_{f_0} is the amplitude for $f_0(980)$, BW are the Breit-Wigner functions and $B_{\pi^+\pi^-}, B_{K^+K^-}$ are the background functions. The a_{f_0} coefficients are related by

$$a_{f_0}^{K^+K^-} = 0.75\frac{e_{K^+K^-}}{e_{\pi^+\pi^-}}a_{f_0}^{\pi^+\pi-} \tag{3.16}$$

where $e_{K^+K^-}/e_{\pi^+\pi^-}$ is the ratio of the reconstruction efficiencies and the factor 0.75 comes from Clebsch-Gordan coefficients[2]. The fit strategy adopted in the study uses the Flatté parametrisation [81] which is a slightly modified relativistic version of the Breit-Wigner distribution first introduced for the description of the $\pi\eta$ invariant-mass distribution near the KK threshold where the $a_0(980)$ scalar-isovector resonance is located. The Flatté parametrisation has been usually employed to describe differential mass distributions resulting from S-wave resonance-like structures, located near a threshold. There are also some other examples of hadronic resonances, located near thresholds, that can be reasonably described in terms of the Flatté distribution [82]. The Flatté parametrization of the amplitude includes three free parameters which should be determined from the experimental mass spectrum. These are the nominal mass of the resonance, the inelastic width at threshold and the coupling constant for the channel of the heavy particles. In particular, the coupled-channel amplitudes for $f_0(980)$ decay via $\pi^+\pi^-$ and K^+K^- were taken to be:

$$A_{f_0}(m_{\pi^+\pi^-}) = \frac{m_0\sqrt{\Gamma_{\pi\pi}}}{m_0^2 - m_{\pi\pi}^2 - im_0(\Gamma_{\pi\pi} + \Gamma_{KK})} \tag{3.17}$$

$$A_{f_0}(m_{K^+K^-}) = \frac{m_0\sqrt{\Gamma_{KK}}}{m_0^2 - m_{KK}^2 - im_0(\Gamma_{\pi\pi} + \Gamma_{KK})} \tag{3.18}$$

[2]The Clebsch–Gordan (CG) coefficients enter in angular momentum coupling, appearing as the expansion coefficients of total angular momentum eigenstates in an uncoupled tensor product basis.

where m_0 is the resonance mass, and the partial widths Γ are related to the coupling constants g via

$$\Gamma_{\pi\pi} = g_\pi \sqrt{\frac{m^2_{\pi\pi}}{4} - m^2_\pi} \qquad\qquad \Gamma_{KK} = g_K \sqrt{\frac{m^2_{KK}}{4} - m^2_K}$$

Being Γ_{KK} imaginary below KK threshold, it leads to a distortion of the $\pi\pi$ mass spectrum from a simple Breit-Wigner shape. The intrinsic properties of the $f_0(980)$ show no significant differences from those of the $f_2(1270)$ and $\phi(1020)$ mesons. $f_0(980)$ features are consistent with the $f_2(1270)$, being a $q\bar{q}$ meson in the ^{3}P state composed mainly of $u\bar{u}$ and $d\bar{d}$. All measured characteristics of $f_0(980)$ production in the Z^0 decay data of OPAL are consistent with its interpretation as a conventional scalar meson, because no evidence has been found for enhanced $f_0(980)$ production at low multiplicities or at large rapidity gap, nor significant differences are seen between the data and the Monte Carlo in the relative production rates [80]. In Figure 3.5 an example of the sum of the fitted mass spectra indicating clearly the signals due to the three resonances is reported. The mass ranges of the fits were 0.82 to 1.50 GeV/c for $\pi^+\pi^-$ and from threshold to 1.18 GeV for K^+K^-, chosen to avoid the ρ^0 peak region in $\pi^+\pi^-$ and the region of its reflection in K^+K^-.

Further $f_0(980)$ measurements via its hadronic decay channel in minimum bias pp and peripheral Au-Au collisions at $\sqrt{s} = 200$ GeV were performed using the STAR detector at RHIC. The study [83] is the first direct measurement at mid-rapidity in heavy-ion collisions and has been performed by invariant mass analysis of opposite-charge $\pi\pi$ pairs in a given event. The resulting invariant mass distribution has been then compared to a background distribution obtained as the geometric mean of the invariant mass distributions of $\pi^+\pi^+$ and $\pi^-\pi^-$ pairs from the same event (like-sign background). Then, the distributions have been normalized to each other at $M_{\pi\pi} \leq 1.5$ GeV/c^2. Resonances in the invariant mass range under study have been fitted using the sum of several components, the so-called *cocktail* (Figure 3.6). The K^0_S was fit to a gaussian. The $\omega(782)$ and $K^*(892)^0$ functions were obtained from the HIJING [53] event generator, with the kaon

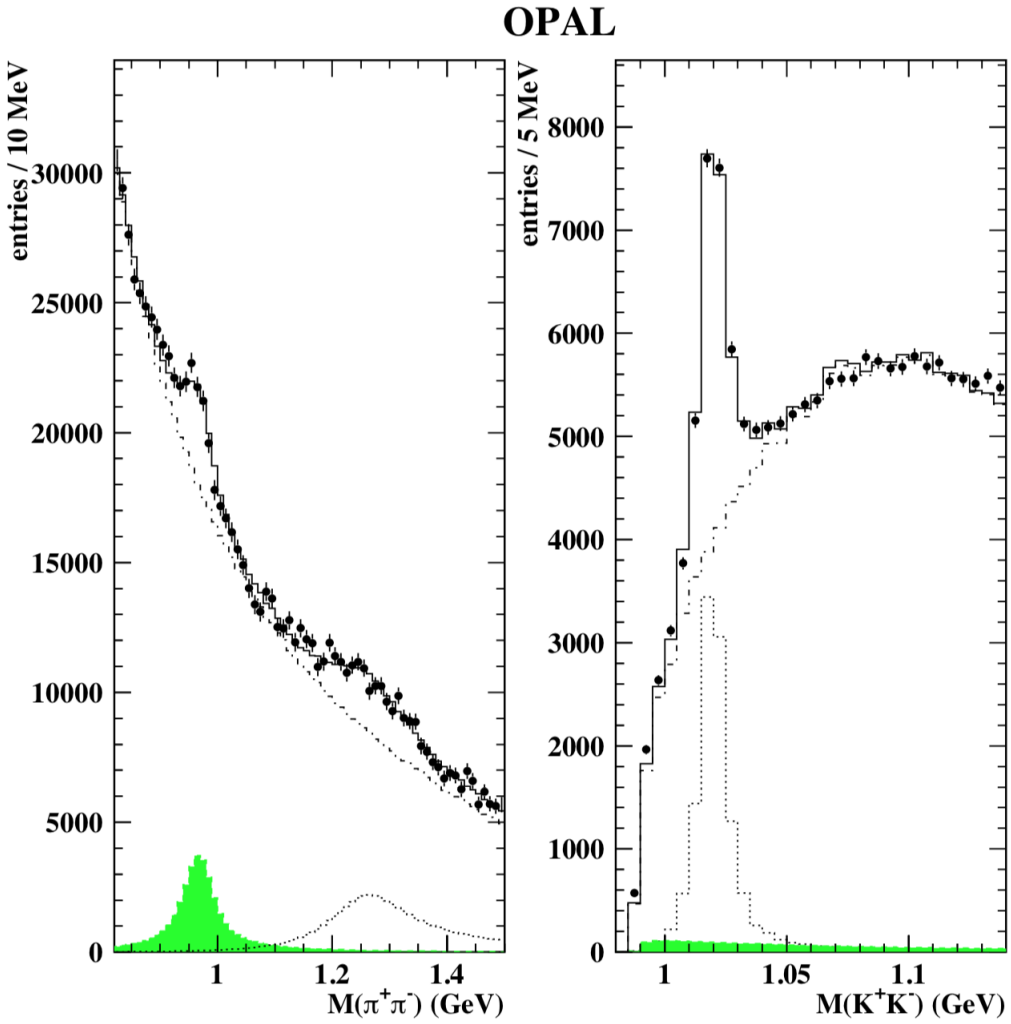

Figure 3.5: Sum of the fitted mass spectra of $\pi^+\pi^-$ (with like-sign spectra subtracted) and K^+K^- from OPAL analysis. The points show the data, and the solid histograms give the results of the fits. The shaded histograms show the $f_0(980)$ contributions, the dotted histograms give the $f_2(1270)$ and $\phi(1020)$ contributions, and the dot-dash histograms show the fitted backgrounds [80].

being misidentified as a pion in the case of the K^{*0}. The $\rho^0(770)$, the $f_0(980)$ and the $f_2(1270)$ were fit to the relativistic Breit-Wigner function times the Boltzmann factor PS $= (M_{\pi\pi}/\sqrt{M_{\pi\pi}^2 + p_{\mathrm{T}}^2}) \cdot exp(-\sqrt{M_{\pi\pi}^2 + p_{\mathrm{T}}^2})/T)$ that represents the phase space available for the decay. Here, T is the temperature at which the resonance is emitted [84]. In Figure 3.6 the sum of all the contributions in the hadronic *cocktail* is reported. The p_T-dependent yield distributions at mid-rapidity measured by STAR in minimum bias and in peripheral Au-Au collisions are shown in figure 7.

Recent contributions to $f_0(980)$ study have been proposed by the LHCb Collaboration in the context of the measurement of the hadronic decay $\bar{B}^0 \to J/\psi\pi^+\pi^-$. In [85], LHCb uses for this measurement data collected in pp collisions corresponding to a sample of 3 fb^{-1} of integrated luminosity, one third at 7 TeV center-of-mass energy and the remaining at 8 TeV. The invariant mass of the $\pi^+\pi^-$ pair has been analysed to determine the fractions of the resonant and non-resonant components, out of which six interfering $\pi^+\pi^-$ states were found to be necessary to give a good description of the invariant mass range under study. As shown in Figure 3.8, data are considered to be best described by adding coherently $\rho(770)$, $f_0(500)$, $f_2(1270)$, $\rho(1450)$, $\omega(782)$ and $\rho(1700)$ resonances, with the largest component being the $\rho(770)$. Furthermore, there is no evidence for $f_0(980)$ resonance production. It has then been found that $f_0(980)$ production is much smaller than what predicted for tetraquarks. In addition, an upper limit for the mixing angle of 17°at 90% C.L. between the $f_0(980)$ and the $f_0(500)$ that would correspond to a substantial $s\bar{s}$ content in $f_0(980)$ has been extracted.

Measurements performed by WA102 (CERN) [86] and CLAS (Jefferson Lab) [87] Collaborations, using the Partial Wave Analysis (PWA) of the $\pi^+\pi^-$ system, allowed to access $f_0(980)$ signal after a decomposition of the invariant mass spectrum into particles with different quantum numbers.
In the next chapter the analysis performed in proton-proton collisions will provide a feasibility study and a reference for the measurements in high-multuplicity events (p-Pb,

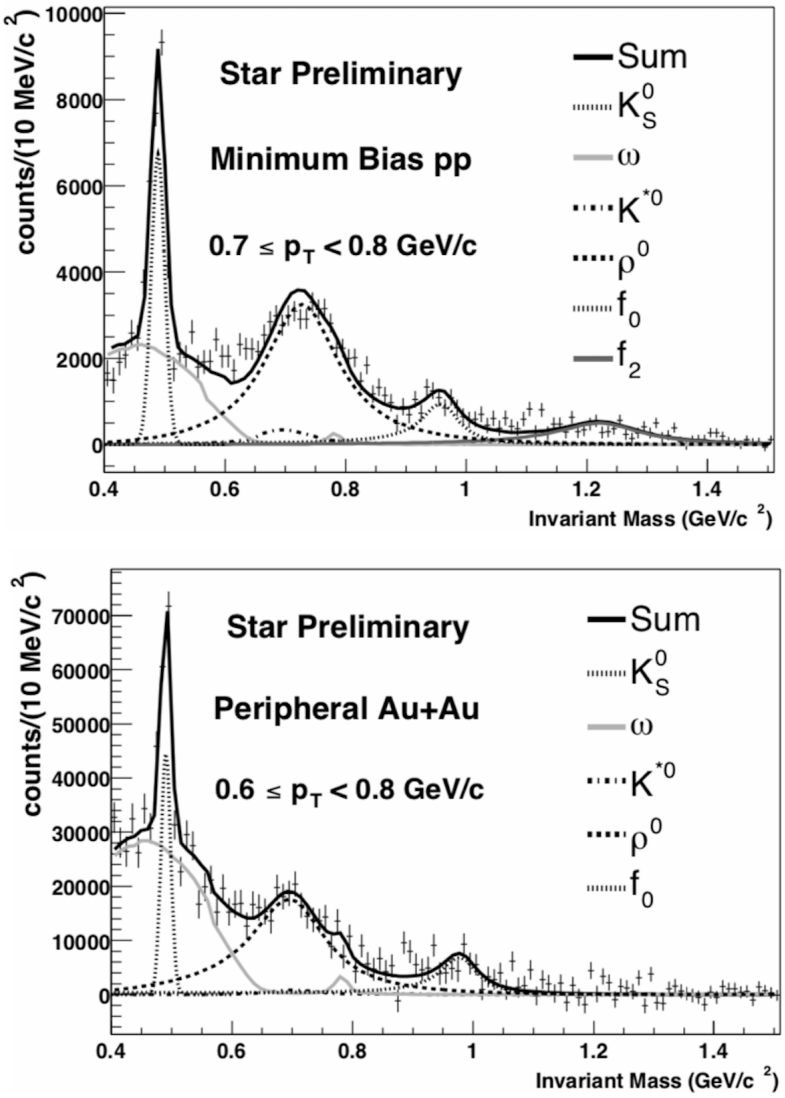

Figure 3.6: The $\pi^+\pi^-$ invariant mass distributions after the subtraction of the like-sign background distributions for minimum bias pp (top) and peripheral Au-Au (bottom) interactions at $\sqrt{s} = 200$ GeV [83]. Curves represent the components of the hadronic *cocktail* used to perform the fit.

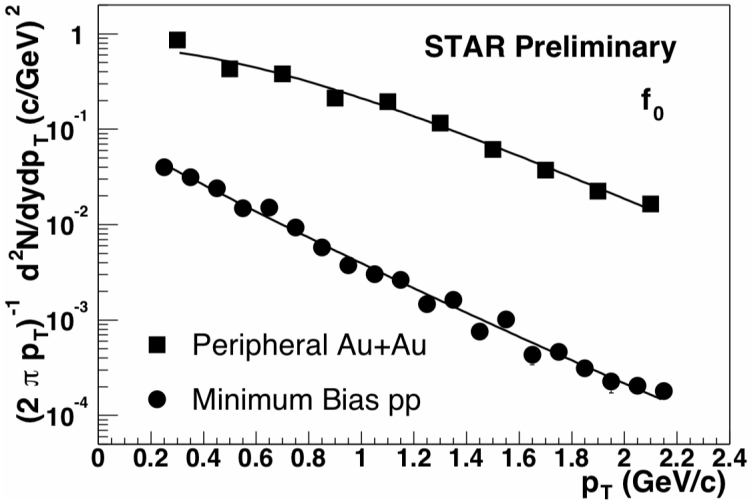

Figure 3.7: The yield as a function of p_{T} distributions at mid-rapidity from f_0 produced in minimum bias pp and peripheral Au-Au collisions $\sqrt{s} = 200$ GeV [83].

Pb-Pb).

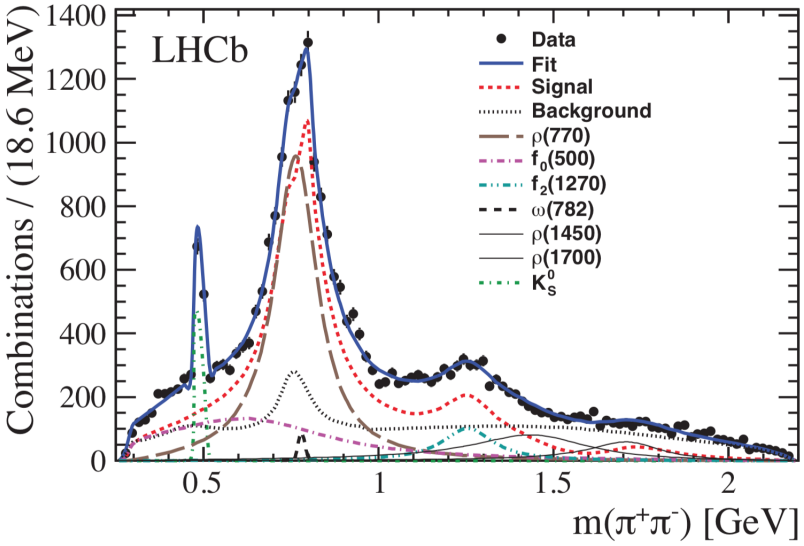

Figure 3.8: Fit projection of $m_{\pi\pi}$ showing the different resonant components in the invariant mass range of interest [85].

Chapter 4

Measurement of $f_0(980)$ production in pp collisions at $\sqrt{s} = 5.02$ TeV

The analysis steps followed to measure the production of the $f_0(980) \rightarrow \pi^+\pi^-$ with the ALICE detector in inelastic pp collisions at $\sqrt{s} = 5.02$ TeV are presented in this chapter. The yields are measured at mid-rapidity ($|y| < 0.5$) in the transverse momentum (p_{T}) range 0.5 - 9.0 GeV/c. The signal extraction is particularly challenging due to the large background and the proximity to other resonance signals. The procedure followed in this work is discussed in detail. The analysis represents the first attempt to perform this measurement with ALICE in inclusive production and it demonstrates the feasibility of the measurement in pp collisions over a wide transverse momentum range. These results are a baseline for other collision systems such as p-Pb and Pb-Pb. In the following, $f_0(980)$ will be denoted as f_0 for brevity.

4.1 Data sample

The analysis is based on a dataset of pp collisions collected in 2015 at the centre-of-mass energy of 5.02 TeV. Data were collected with a minimum bias trigger[1] defined by the

[1] In order to detect inelastic events a minimum bias trigger is necessary. Experimentally, such a sample would be contaminated by for instance diffractive events in pp.

logical *OR* between the signals of V0A and V0C. For this analysis a sample of 1.285×10^8 pp events collected in 2015 has been used. A sample of 1.1×10^8 pp events in which the ITS, TPC, TOF and T0 detector performance were established as optimal by offline data quality assurance analyses has been processed.

4.2 Event selection

Events are selected offline to have a reconstructed primary vertex. The primary vertex position is determined in the SPD or, separately, from tracks reconstructed in the whole central barrel. The rejection of events with the primary vertex outside the fiducial region of 10 cm in the beam direction from the nominal collision point ($|v_z| < 10$ cm) is applied. In Figure 4.1 the v_z distribution of the accepted events is reported. The green continuous line represents the result of a gaussian fit of the distribution. It shows that the vertex is centered around 0.3 cm along the z axis, in average.

Due to the high interaction rate during the 2015 data taking, the sample includes a fraction of pileup events, namely interactions occurring during the same bunch crossing of the triggered event but with vertices that are displaced with respect to the vertex of the main interaction. In the sample used here, the probability to have pile up events per bunch crossing was found to be low: the mean number of interactions per bunch crossing was $0.003 < \mu < 0.05$. A selection criterion based on the correlation between the number of hits in the first layer of the SPD and the number of tracklets reconstructed in the ITS, used to estimate the vertex position, has been applied. In particular events are rejected if there are

- more than 3 hits in SPD for events with less than 20 tracklets,
- more than 4 hits in SPD for events with a number of tracklets between 20 and 50,
- more than 5 hits in SPD for events with more than 50 tracklets.

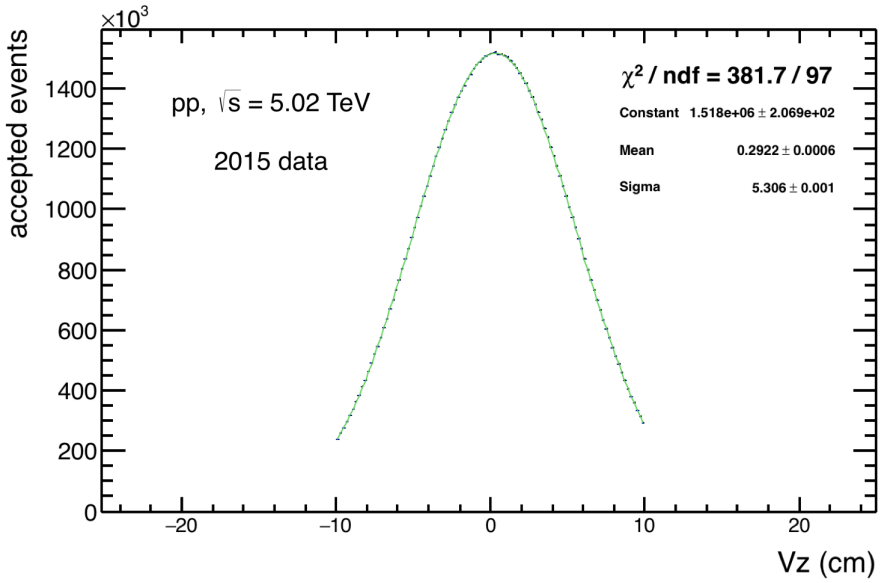

Figure 4.1: Vertex position distribution along the beam axis (z) for events after all selections described in the text. The green continuous line represents a Gaussian fit of the distribution.

After all selections, the total number of events is reduced to 9.5×10^7, that is $\sim 86\%$ of the initial sample.

4.3 Track selection

The f_0 resonance is studied by reconstructing its hadronic decay into oppositely charged pions (dominant decay channel, [7]). Its short lifetime causes the f_0 to decay early after production, thus making the produced π^+ and π^- indistinguishable from the charged primary particles produced in the "bulk".

In order to use the fiducial region in which ALICE performs full tracking and provides the best possible PID, only tracks with pseudorapidity in $|\eta| < 0.8$ and $p_{\mathrm{T}} < 0.15$ GeV/c have been accepted. In order to ensure a good quality of the reconstruction, tracks are required to cross at least 70 out of 159 TPC readout rows (see 2.3.2) and to have two

measured points in the ITS (out of which at least one is in the SPD). The χ^2 per TPC cluster is required to be less than 4 and the χ^2 per ITS cluster is required to be less than 36. Additional cuts to help in discriminating between good and fake tracklets concern the distance of closest approach (DCA), which is the minimum distance between two track trajectories, ideally zero if the two tracks come from the same interaction point. In order to suppress the contribution of secondary particles, it is required that the component of the DCA which is parallel to the beam axis satisfies $\mathrm{DCA}_z \leq 2.0$ cm, while the transverse component satisfies $\mathrm{DCA}_{xy} \leq 0.0105 + 0.0350\ p_{\mathrm{T}}{}^{1.1}$ GeV/c. The latter is parameterised as a function of p_{T} to take into account the deflection of the trajectories in the magnetic field.

4.4 Particle identification

PID is used to identify candidate f_0 daughters. It is performed combining the information of the specific energy loss ($\mathrm{d}E/\mathrm{d}x$) in the TPC and the time of flight measurement from the TOF. The energy loss is described by the Bethe-Bloch formula [88]

$$\left\langle \frac{dE}{dx} \right\rangle \propto \frac{z^2}{\beta^2} log\Big(\frac{2\gamma^2\beta^2 m_e}{I_0}\Big) \tag{4.1}$$

where β is the particle velocity, γ the Lorentz factor, m_e the electron mass, I_0 the minimum energy loss and z the charge of the incident particle in units of the elementary charge. In the case of the ALICE TPC, the specific energy loss as a function of the particle's velocity can be empirically parametrized by the function:

$$f(\beta\gamma) = \frac{P_1}{\beta^{P_4}}\Big(P_2 - \beta^{P_4} - ln(P_3 + \frac{1}{(\beta\gamma)^{P_5}})\Big) \tag{4.2}$$

where P_{1-5} are fit parameters. At low momenta ($p_{\mathrm{T}} \leq 1$ GeV/c) PID can be performed track-by-track while at higher momenta, in the relativistic rise region, the $\mathrm{d}E/\mathrm{d}x$ exhibits a nearly constant separation for the different particle species over a wide momentum range. It is still possible to extract the relative contributions of different particle

species via multi-Gaussian fits [89]. For this analysis, a fiducial selection around the expected signal is defined by an interval usually expressed in terms of number of σ, where σ is the expected $\mathrm{d}E/\mathrm{d}x$ resolution (5.5%).

TOF provides PID in the intermediate momentum range (see 2.2.1), based on the measurement of the time of flight of the particles. A PID strategy that exploits TOF is based on the discriminating variable N_{TOF}, which is defined as

$$N_{\sigma,i}^{TOF} = \frac{t_{TOF} - t_0 - t_{exp,i}}{\sigma_{PID,TOF}} \tag{4.3}$$

where i indicates the particle species, t_{TOF} the measured TOF hit time, t_0 the interaction time, $t_{exp,i}$ the expected time of flight computed during the central tracking procedure. The total resolution is

$$\sigma_{PID,TOF} = \sqrt{\sigma_{TOF}^2 + \sigma_{t_0}^2 + \sigma_{t_{exp,i}}^2} \tag{4.4}$$

The simplest PID estimator for a given mass hypothesis m_i is then constructed, for both the detectors, as a $n\sigma$ quantity:

$$n\sigma_{i,j}^{\sigma_{PID}} = \frac{X_j - X_{i,j}^{exp}}{\sigma_{i,j}^{PID}} \tag{4.5}$$

where X_j is the observable measured in the detector i, $X_{i,j}^{exp}$ is the expected value in the mass hypothesis j and $\sigma_{i,j}^{PID}$ is the resolution on the measurement.

Aiming at rejecting as much as possible the background while not compromising the efficiency, the particle identification strategy chosen for the analysis presented in this thesis is based on the following:

- if the TOF information is available, it is required that $n\sigma_{TOF} < 3$ and $n\sigma_{TPC} < 5$,
- otherwise identification is done only in the TPC, with a cut of $n\sigma_{TPC} < 2$.

The additional 5σ cut on the TPC signal is applied on top of TOF PID in order to reduce the contribution of the mismatched tracks, namely the tracks wrongly associated to TOF hits. The TPC and TOF response distributions for pions are reported in Figure 4.2 for

the tracks selected with all the cuts described, from the full dataset used for the f_0 analysis.
Only resonance candidates produced at midrapidity are selected with a reconstructed pair rapidity cut $|y| < 0.5$.

4.5 Signal extraction

In order to obtain the signal invariant mass (M_{inv}) distribution from the combination of primary identified pion pairs, a careful study of the background has been performed. M_{inv} distributions are functions of the resonance p_{T} which has been measured in the range 0.5 - 9.0 GeV/c. The range has been divided in nine intervals chosen to balance the statistics in each bin, resulting in:

$$p_{\mathrm{T}}[\ ] = \{0.5, 1.0, 1.5, 2.0, 2.5, 3.0, 4.0, 5.0, 7.0, 9.0\}$$

The signal has been extracted in all p_{T} bins. In this chapter results are reported for the intermediate p_{T} bin, $1.5 \leq p_{\mathrm{T}} \leq 2.0$ GeV/c, as exemplary of the procedure. The large background from correlated pion pairs from resonance decays in the invariant mass (M_{inv}) window under study, as well as the combinatorics from uncorrelated pairs, make the signal extraction particularly challenging.

The Unlike-Sign Pairs distribution (henceforth referred to as USP) contains all correlated pion pairs as well as the uncorrelated opposite-charged pion pairs from the same event. Two different techniques have been used in order to estimate the background aiming to subtract its distribution from the USP.

The Like-Sign Background (henceforth referred to as LSB) is composed by pairs of pions with the same charge from the same event. $\pi^+\pi^+$ and $\pi^-\pi^-$ pairs are built separately and then combined into a geometric mean, according to the expressions:

$$LSB = 2\sqrt{y_{++}y_{--}}, \qquad \delta LSB = \sqrt{\frac{y_{++}^2(\delta y_{--})^2 + y_{--}^2(\delta y_{++})^2}{y_{++}y_{--}}} \tag{4.6}$$

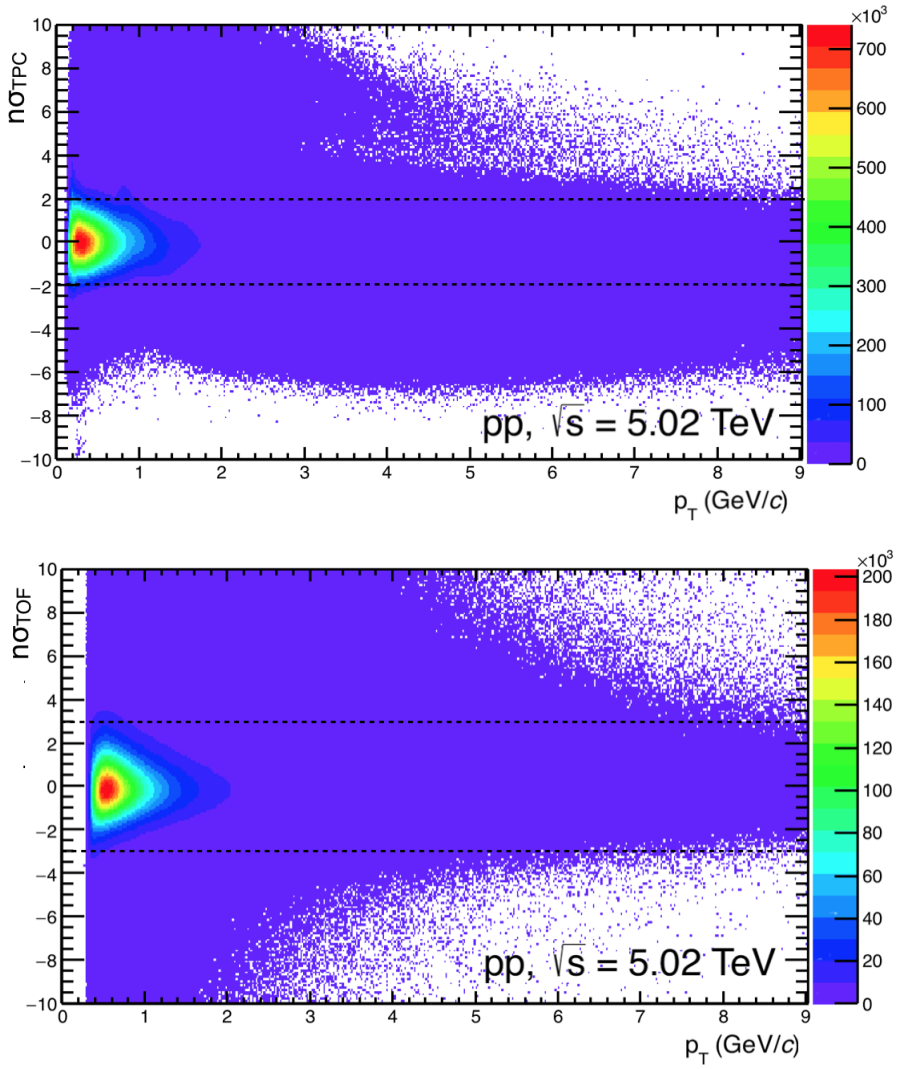

Figure 4.2: TPC (top) and TOF (bottom) response in terms of $n\sigma_{PID}$ as function of the particle momentum at the inner radius of the TPC and as function of the particle momentum at the vertex, respectively. The black dashed lines mark a 2σ selection for the TPC and a 3σ for the TOF which correspond to the PID strategy chosen to perform the analysis.

where $y_{\pm\pm}$ are the entries in each M_{inv} bin for the pion pairs distributions and $\delta y_{\pm\pm}$ are their statistical errors. LSB pairs are estimated from the same set of events as the USP, thus no normalization is needed before background subtraction. The major assumption of this method is that the USP distribution contains the signal, while the LSB does not contain any resonance. Combining all possible pairs with the same sign of electric charge (like-sign), the correlation of resonance under study is completely excluded as the assumption.

The Mixed Event unlike-sign Background (henceforth referred to as MEB) is composed by uncorrelated unlike-sign pion pairs, from different events. Aiming at reproducing satisfactorily the kinematic properties of the combinatorial background, when applying this method only pairs from events which have similar topology and multiplicity are combined. After being selected by applying the criteria listed below:

- difference in the z coordinate of the primary vertex position, $\Delta z_{vtx} \leq 1.0$ cm
- difference in multiplicity, $\Delta m \leq 5$

a maximum of 5 events at the time have been considered for the mixing. The resulting M_{inv} distribution, which reflects the statistics of the mixed events used in the estimate of the MEB, has been then normalized to the integral of the USP distribution before background subtraction. The normalization range 1.15 GeV/c^2 $\leq$ M$_{inv}$ $\leq$ 1.20 GeV/c^2 was chosen, being it sufficiently far from the f$_0$ signal peak.

In order to provide a further check on the background estimation, a Mixed Event Like-sign background (henceforth referred to as MEL) composed by uncorrelated like-sign $\pi^+\pi^+$ and $\pi^-\pi^-$ from mixed events, separately built and then combined according to the geometric mean, has been obtained to be compared with LSB and MEB. As in MEB case, the normalization range 1.15 GeV/c^2 $\leq$ Minv $\leq$ 1.20 GeV/c^2 was chosen. In Figure 4.3 USP, LSB, normalized MEB (nMEB) and MEL (nMEL) distributions are shown.

The ratio between $\pi^-\pi^-$ and $\pi^+\pi^+$ like-sign pairs distributions, reported in Figure 4.4, shows that there is a difference of 1-2% between the positively and negatively charged

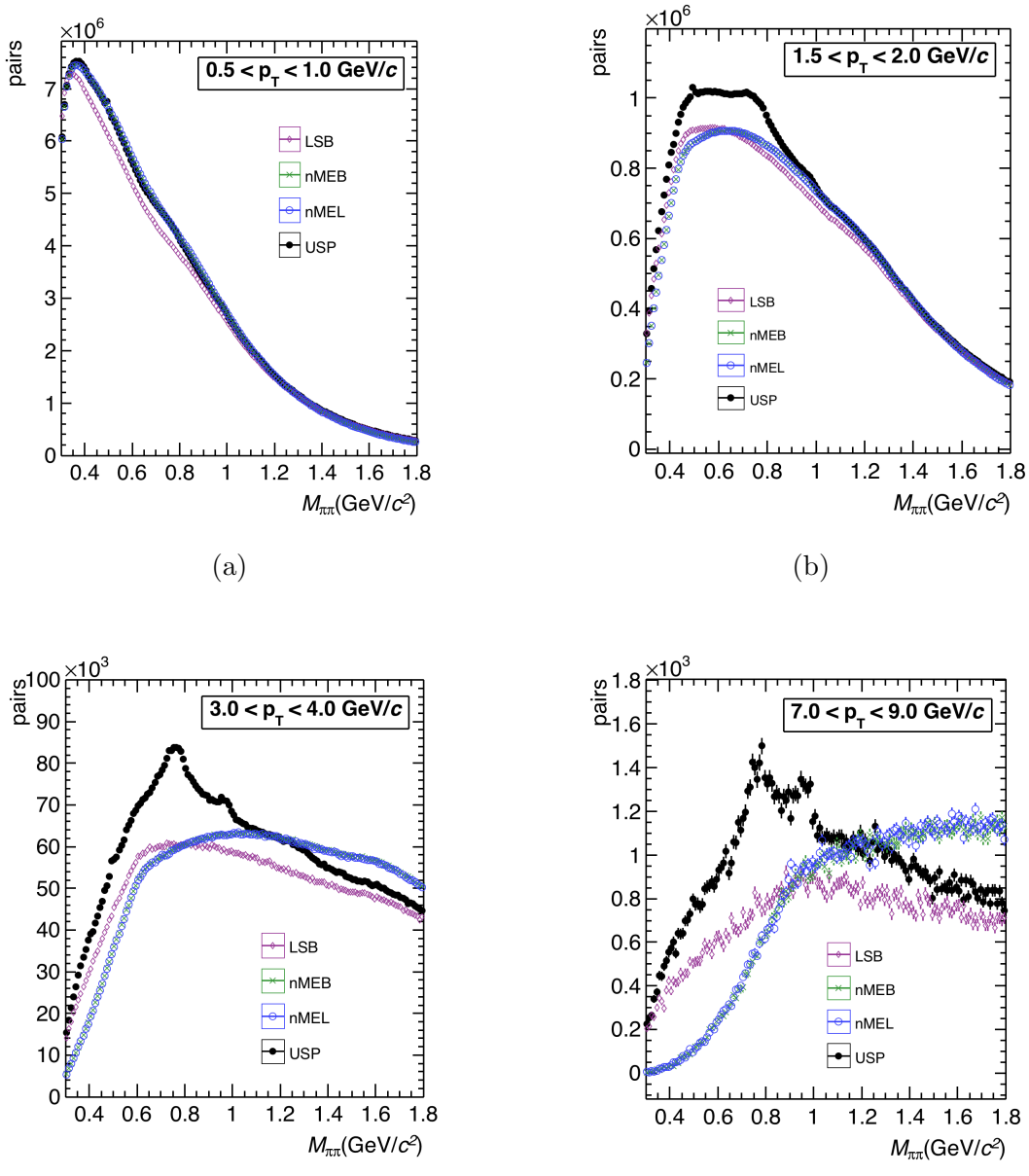

Figure 4.3: Unlike-sign charged particle pairs distribution, USP, (black) compared to like-sign, LSB, (magenta), normalized mixed event unlike-sign, nMEB, (green) and normalized mixed event like-sign, nMEL, (blue) background distributions for $\pi^+\pi^-$ with $0.5 \leq p_{\mathrm{T}} \leq 1.0$ GeV/c (a), $1.5 \leq p_{\mathrm{T}} \leq 2.0$ GeV/c (b), $3.0 \leq p_{\mathrm{T}} \leq 4.0$ GeV/c (c), $7.0 \leq p_{\mathrm{T}} \leq 9.0$ GeV/c (d). nMEB and nMEL are normalized in the 1.15-1.20 GeV/c^2 invariant mass range, while the LSB is not normalized.

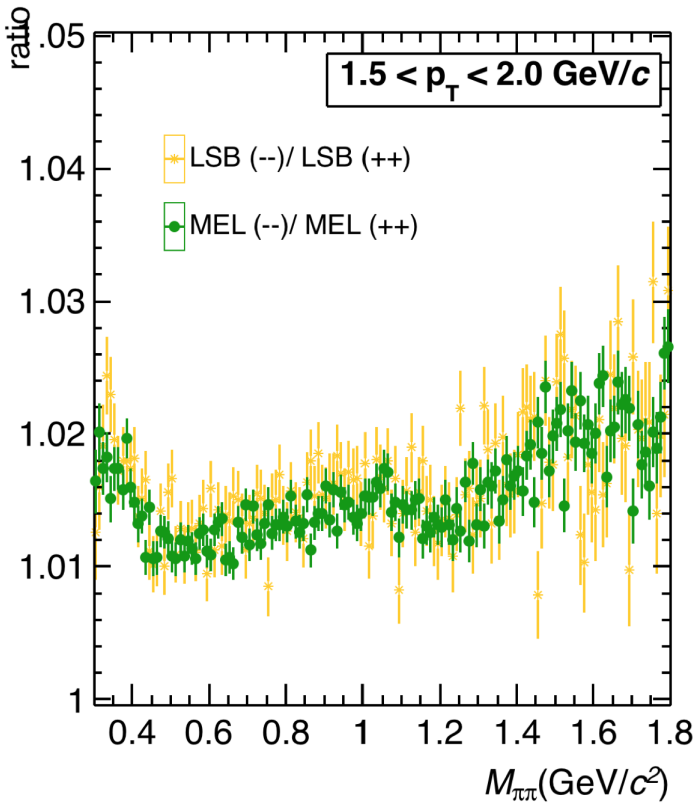

Figure 4.4: Like-sign pairs distribution ratio in $1.5 \leq p_{\mathrm{T}} \leq 2.0$ GeV/c transverse momentum range. Same-event (orange) and mixed-event (green) ratios are consistent.

pairs. This difference is the same in same-event and mixed-event background distributions as it is related to a different reconstruction efficiency for positive and negative tracks. This ratio exhibits the same trend in all the p_{T} bins under study.

In the invariant mass range $0.3 \leq M_{\pi\pi}$ 1.8 GeV/c^2 there are several contributions from mesons decaying in $\pi^+\pi^-$ (or mis-reconstructed pairs) which cannot be considered negligible. A list of the main contributions to the correlated background is provided below:

1. $\rho^0(770) \rightarrow \pi^+\pi^-$
2. $\omega(782) \rightarrow \pi^0\pi^+\pi^-$
3. $\omega(782) \rightarrow \pi^+\pi^-$
4. $f_2(1270) \rightarrow \pi^+\pi^-$
5. $K^0_S \rightarrow \pi^+\pi^-$
6. $K^*(892)^0 \rightarrow K^{\pm}\pi^{\mp}$
7. $\eta \rightarrow \pi^0\pi^+\pi^-$
8. $\eta' \rightarrow \eta\pi^+\pi^-$
9. $\phi \rightarrow K^+K^-$

Note that (6) and (9) appear in this list because in some cases the charged kaons in the final state may be misidentified as pions in which the charged kaons in the final state are mis-identified as pions. Such a complex background makes difficult to identify a *safe* normalization range where USP only corresponds to uncorrelated pion pairs. For this reason, in this analysis LSB has been chosen as the main strategy to estimate the background. $\pi^+\pi^-$ signal after LSB, nMEB and nMEL subtraction, for the intermediate $1.5 \leq p_{\mathrm{T}} \leq 2.0$ GeV/c, are shown in Figure 4.5. Contributions from other resonances in the invariant mass range under study are explicitly indicated.

After background subtraction, the resulting distribution, exhibiting the characteristic peak of the resonance signal on top of a residual background, has been fitted in order to extract the raw yield in each transverse momentum interval.

4.6 Invariant mass fit

The fit of the signal distribution has been performed with the Roofit [90] package. The f_0 peak is shaped with a relativistic Breit-Wigner function, while the residual combinatorial background has been described with an exponential function, bg($\mathrm{M}_{\pi\pi}$), for the regions at the left- and right-hand side of the peak. Due to the overlap of the tail of the f_0 distribution with the wide $\mathrm{f}_2(1270)$ meson, which decays in the same channel, a relativistic Breit-Wigner has been included to take into account the $\mathrm{f}_2(1270)$ contribution correctly. The total fit function is the sum of the two relativistic Breit-Wigner functions and bg($\mathrm{M}_{\pi\pi}$):

$$f(M_{\pi\pi}) = \frac{M_{\pi\pi}\Gamma_{f_0}M_{f_0}}{(M_{\pi\pi}^2 - M_0^2)^2 + M_0^2\Gamma_{f_0}^2} + \frac{M_{\pi\pi}\Gamma_{f_2}M_{f_2}}{(M_{\pi\pi}^2 - M_0^2)^2 + M_0^2\Gamma_{f_2}^2} + bg(M_{\pi\pi}) \qquad (4.7)$$

The fit range, $0.86 \leq \mathrm{M}_0 \leq 1.50$ GeV/c^2, has been chosen as a compromise between keeping the overlap with the $\rho^0(770)$ peak to the minimum and constraining the fit of the background on the left-hand side of the f_0 peak.

A first attempt to perform the fit leaving the f_0 width and mass parameter free provided unstable results. Thus, just the mass M_{f_0} was left free within the fit range

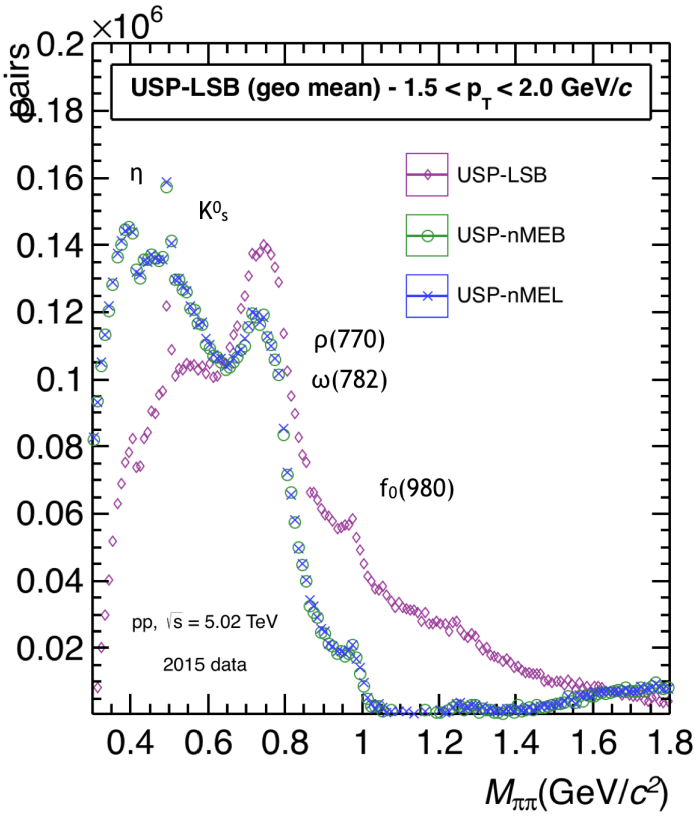

Figure 4.5: $\pi^+\pi^-$ signal after LSB (magenta), nMEB (green) and nMEL (blue) subtractions, for the intermediate $1.5 \leq p_{\mathrm{T}} \leq 2.0$ GeV/c. Signal peaks of other mesons in the invariant mass range under study are explicitly labeled. The normalization range used for MEB is 1.15 GeV/$c^2 \leq$ Minv $\leq$ 1.20 GeV/c^2.

and resulted in the values reported in Figure 4.8. The average value of about 970 MeV is compatible with the lower limit on the resonance mass reported by the PDG. The most recent literature (see [7] and references therein) seems to favour a width of around $\Gamma = 50$ MeV or lower. The fit was stabilized for all p_{T}'s by fixing Γ_{f_0} to this value. Because the PDG [7] reports more precisely on f_0 mass value than on Γ_{f_0}, also a different strategy has been performed. f_0 mass has been fixed as $\mathrm{M}_{f_0} = 990$ MeV and the width has been extracted, as reported in Figure 4.9. For $p_{\mathrm{T}} > 1.5$ GeV/c the width is between 30 and 35 MeV/c^2, whereas at lower p_{T} it reaches 40-50 MeV/c^2. In Chapter 5 the different configurations will be included in the estimate of the systematic uncertainty associated with the fit.

The resonance parameters for $\mathrm{f}_2(1270)$ have been fixed to the values reported by the PDG [7]: $\mathrm{M}_{f_2} = 1275.5$ MeV, $\Gamma_{f_2} = 186.7$ MeV. Exponents of the function used to fit the residual background have been constrained within a range optimised for each p_T bin. The fit result relative to the intermediate 1.5-2.0 GeV/c transverse momentum bin is reported in Figure 4.6. In Figure 4.7, the fit is shown in a larger invariant mass range, to illustrate that the extrapolation of the exponential function still describes the background beyond the fitting range and far from the f_0 peak.

Eventually, the *default* fit strategy chosen was the one with free mass and fixed Γ values. It allowed to extract the raw yield which is reported in Figure 4.10.

4.7 Efficiency $\times$ acceptance

The Monte Carlo (MC) events used to compute the efficiency times acceptance correction were generated using PYTHIA8 with Monash 2013 tune [91] simulating the detector conditions of the data taking period of interest. The particle transport in the detector is taken care of by GEANT3 [92]. Since the event generator does not provide $f_0(980)$ signals, an *ad hoc* MC simulating the pp sample at 5.02 TeV with injected $f_0(980)$, $f_2(1270)$ and $\Lambda(1520)$ signals has been adopted. The simulation reproduced the conditions of the detector during the data taking. Resonances are injected with a flat distribution in p_{T}.

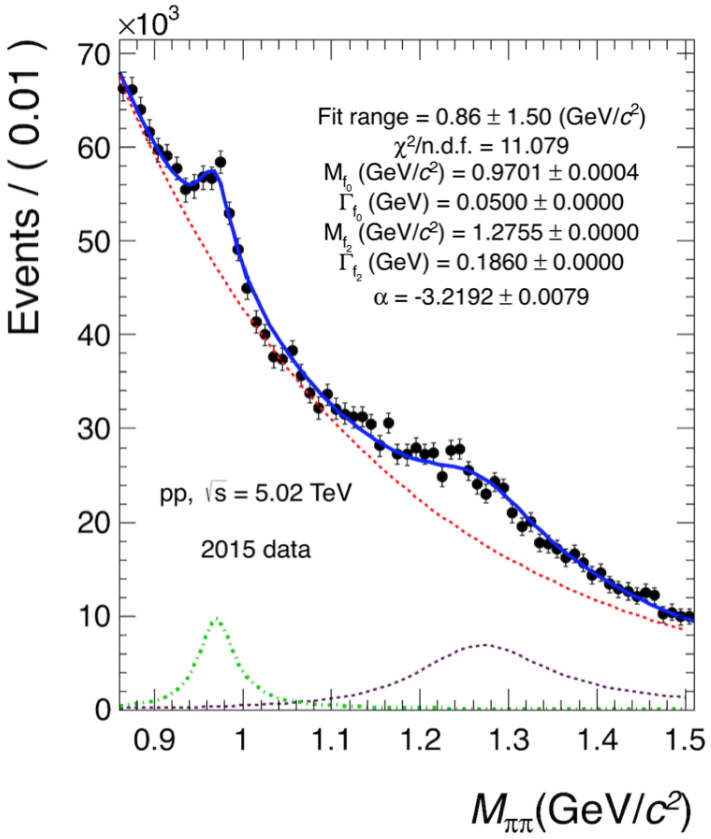

Figure 4.6: f_0 signal in $1.5 \leq p_T \leq 2.0$ GeV/c (dashed green), resulting after the LSB subtraction. The signal is fitted with a relativistic Breit-Wigner function. The $f_2(1270)$ signal is also fitted with a relativistic Breit-Wigner (dashed purple) while the residual background is shaped via an exponential function (red dashed line). The solid blue line represents the total fit function. The values of the fitted parameters are reported.

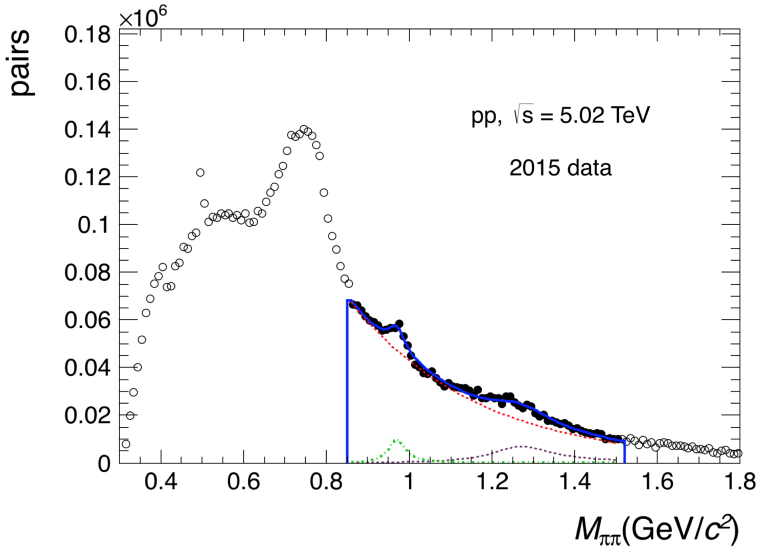

Figure 4.7: Fit to the $f_0(980)$ + $f_2(1270)$ signals and exponential background (same as Figure 4.6) in a widened invariant mass range that shows the presence of the lower mass resonances.

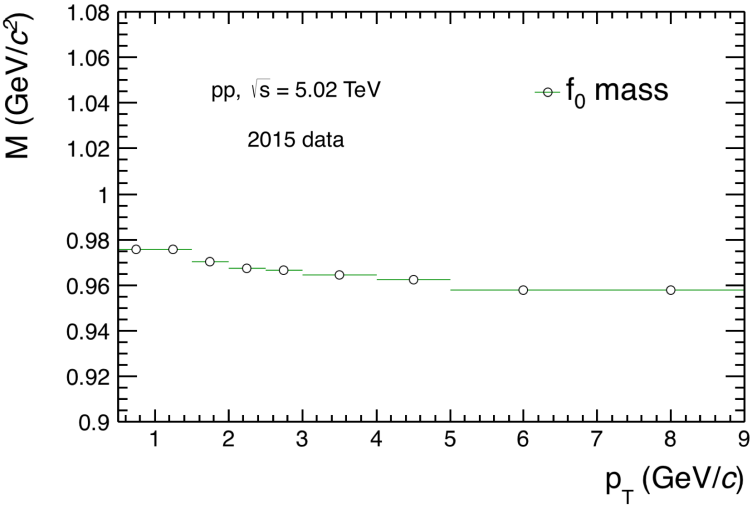

Figure 4.8: $f_0(980)$ mass obtained from the fit. Only the statistical error is reported. The black dashed line indicates the PDG value for the $f_0(980)$ mass.

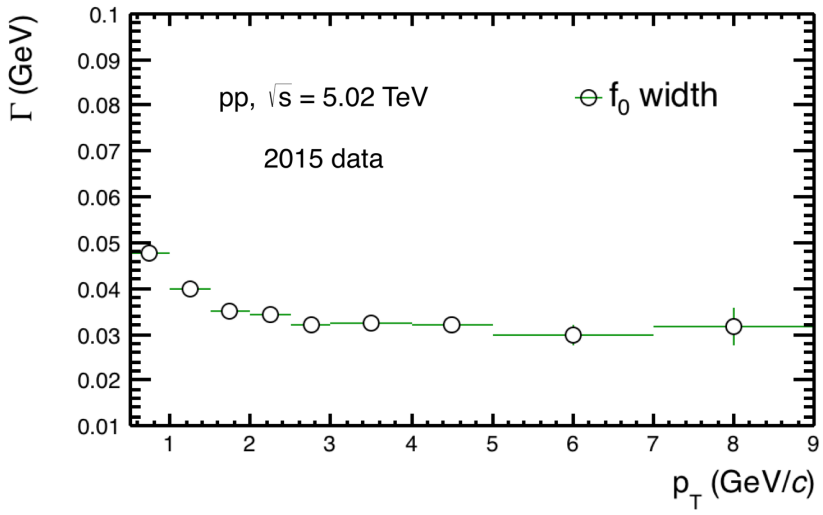

Figure 4.9: $f_0(980)$ width obtained from the fit. Only the statistical error is reported. On the y-axis Γ_{PDG} range values are displayed.

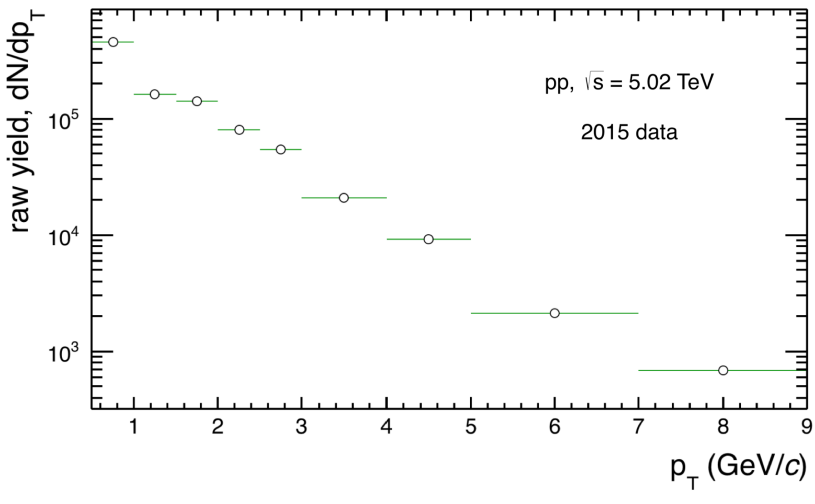

4

Figure 4.10: $f_0(980)$ raw yield obtained from the fit. Only the statistical error is shown.

The MC sample consists of 4.5×10^6 events. Tracking algorithms, even if optimised, are not fully efficient in the reconstruction of particle trajectories, indeed there are some inefficiencies which unavoidably affect the reconstruction. Since MC simulations reproduce the full geometry and data taking conditions of the detectors, they allow to correct the measurements for finite efficiency and acceptance.

The efficiency $\times$ acceptance, which is the p_{T}-dependent correction due to the reconstruction efficiency ($\epsilon(p_{\mathrm{T}})$) and the detector acceptance (Acc) can be defined as:

$$(Acc \times \epsilon)(p_{\mathrm{T}}) = \frac{N_{rec}(p_{\mathrm{T}}^{rec})}{N_{gen}(p_{\mathrm{T}}^{gen})} \tag{4.8}$$

where p_{T}^{rec} and p_{T}^{gen} are the p_{T} measured by the tracking algorithm and the p_{T} generated by the event generator, respectively. Both numerator and denominator are considered in $|y| < 0.5$. N_{rec} is the number of tracks identified as daughters using the PDG code [7] and satisfying the selection criteria (e.g. geometrical acceptance, quality cuts, PID, etc.), while N_{gen} is the number of generated particles of interest. Although the MC sample used for the analysis does not provide realistic absolute values for N_{rec} and N_{gen}, the ratio is authentic and can be used to evaluate $(Acc \times \epsilon)(p_{\mathrm{T}})$. In Figure 4.11 efficiency $\times$ acceptance used to correct the raw spectra is reported. Note that the contribution is strongly p_{T}-dependent. In order to verify weather there is any dependency of the reconstruction efficiency from the invariant mass and to evaluate the corresponding correction, a check on the MC production has been performed considering the ratio between the invariant mass distributions of the f_0 reconstructed and the generated ones. The distribution is symmetric on the left- and the right-side of the f_0 peak. No corrections to the reconstruction efficiency from the invariant mass have therefore been considered. Results are reported in Figure 4.12.

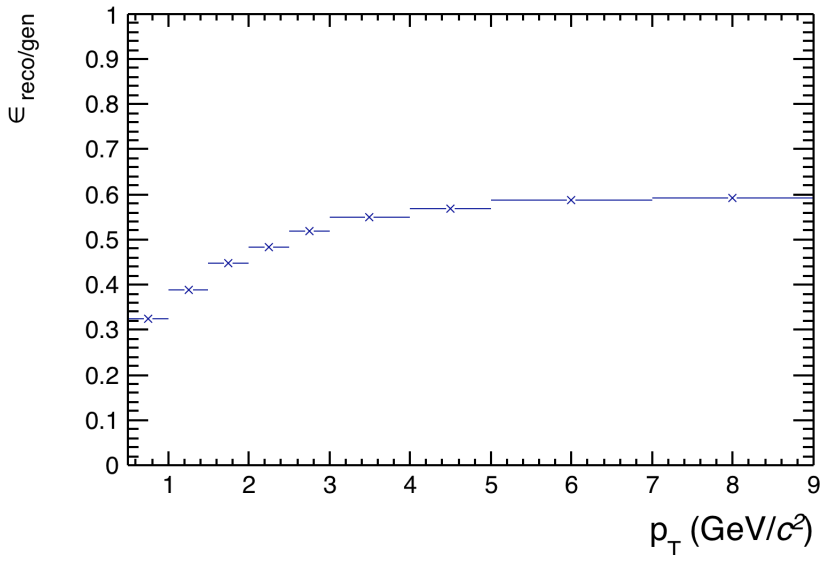

Figure 4.11: $f_0 \to \pi^+\pi^-$ efficiency $\times$ acceptance as estimated from a PYTHIA8 simulation of the 2015 pp data set used for the analysis.

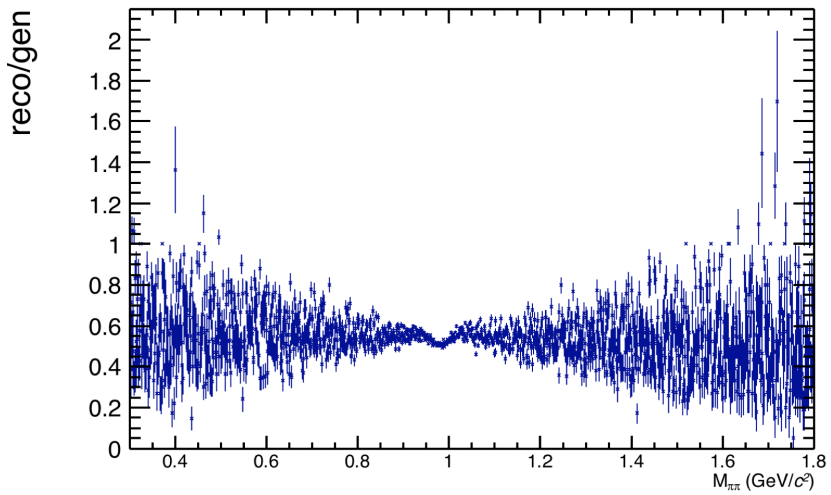

Figure 4.12: Ratio between the invariant mass distributions of the f_0 reconstructed and the generated, respectively, as estimated from a PYTHIA8 simulation anchored to 2015 pp data.

Chapter 5

Systematics and results

5.1 Systematic uncertainties

In order to evaluate if and how much the measurement of the f_0 yield is affected by systematic uncertainties, several checks have been performed by varying the *default* analysis steps. After comparison with the central value of the spectrum, the differences are kept into account to quantify the systematic uncertainties, as described in the following. Sources of systematic uncertainties considered in this work are:

- Material budget and hadronic interaction cross section in the material
- Global tracking
- Particle Identification
- Background subtraction
- Fitting functions
- Fit parameters and choice of the fit range

Material budget and hadronic interaction cross section. Particles which cross the experimental apparatus suffer the effect of the material budget, which is known with

an uncertainty of about ± 4.5% [41]. Monte Carlo (MC) samples reproduce the amount of material only to this extent causing an impact on the reconstruction. The systematic uncertainty has been evaluated for primary tracks by comparing the efficiencies determined in MC productions where material budget was increased and decreased within the above-mentioned limits. Since f_0 decays into two pions which are independently tracked, the systematic associated to the material budget for each of the two charged pions obtained for previous analyses (see [93]) have been linearly summed taking into account the phase space of the f_0 decay. The resulting contribution is about 1% for $0.5 < p_{\mathrm{T}} < 1.5$ GeV/c and negligible above that.
Similarly, the contribution associated with the partial knowledge of the hadronic cross section in the material has been evaluated starting from the single-track uncertainty for pions from [94]. It results in about 2.4 % for $0.5 < p_{\mathrm{T}} < 1.5$ GeV/c and it is negligible above that. In Figure 5.1 the single track contributions are shown.

Global tracking. A contribution to the systematics comes from the fact that the matching efficiency between ITS hits and TPC tracks as reproduced in MC does not perfectly match the one in the data. The uncertainty is the ratio between the matching efficiency observed on data and the one from MC samples. From previous analyses, this was estimated to contribute to the systematic uncertainty for the single track with a 1% for $0.5 < p_{\mathrm{T}} < 2$ GeV/c, 2% for $2 < p_{\mathrm{T}} < 7$ GeV/c, 1% for $7 < p_{\mathrm{T}} < 10$ GeV/c. As for the previous contributions, the uncertainty for the two pions have been added linearly.

Particle Identification. The procedure to evaluate the systematics introduced by the choice of the PID strategy is explained in detail as exemplary. The conditions requested to identify the f_0 candidate daughters for the *default* PID configuration used for the analysis presented in this thesis, were two: a coincidence of $|n\sigma_{TOF}| < 3$ and $|n\sigma_{TPC}| < 5$, when TOF information available, and a $|n\sigma_{TPC}| < 2$ otherwise. The following three different PID configurations have been chosen as alternatives:.

- a coincidence of $|n\sigma_{TOF}| < 4$ and $|n\sigma_{TPC}| < 5$ when TOF information available,

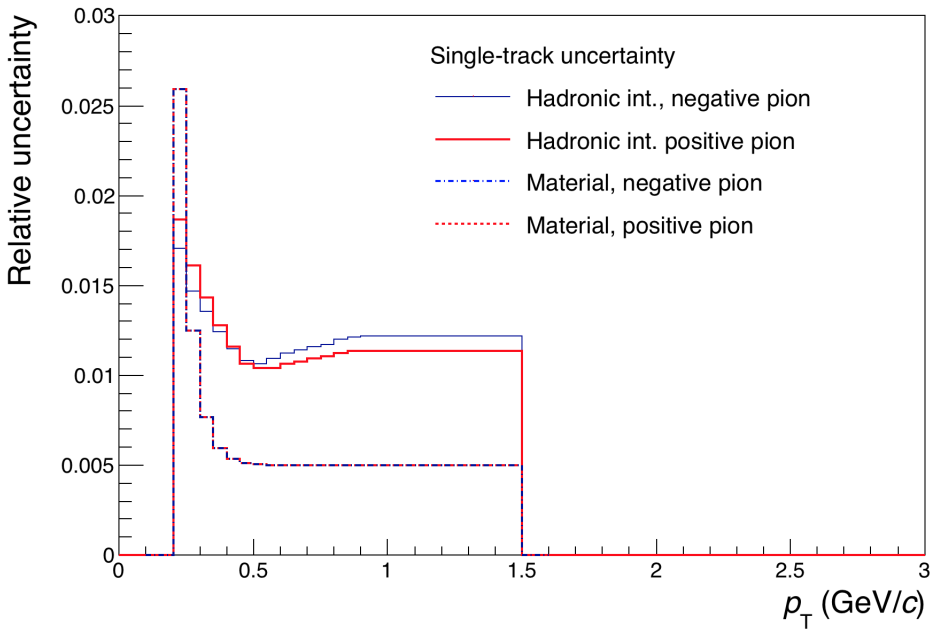

Figure 5.1: Single track systematic uncertainties of positive and negative pions associated with the knowledge of the material budget of the ALICE detector and the hadronic interaction cross section in the material. Values are inherited from the analysis in pp 7 TeV published in [94].

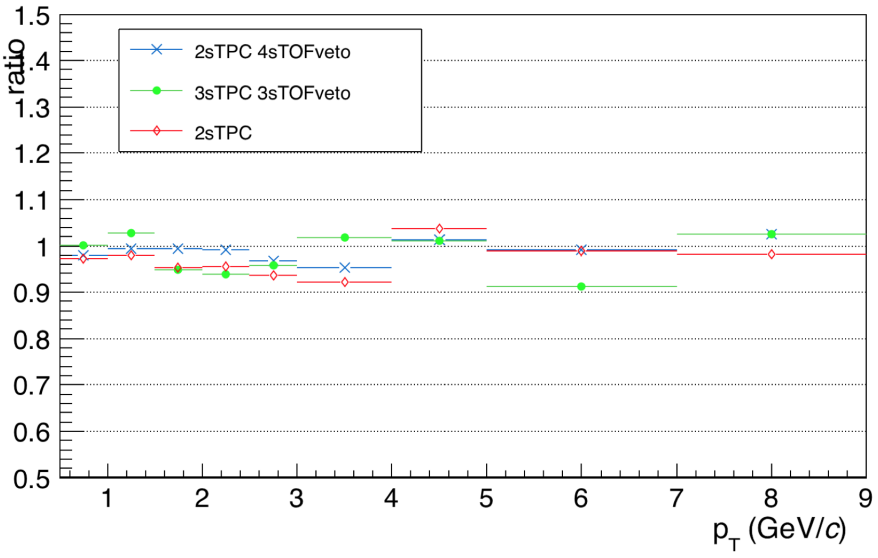

Figure 5.2: Systematic uncertainties due to the variation of the PID strategy. Ratios obtained dividing the corrected spectra from alternative strategies relative to the *default* are explicitly labeled.

$|n\sigma_{TPC}| < 2$ otherwise

- a coincidence of $|n\sigma_{TOF}| < 3$ and $|n\sigma_{TPC}| < 5$ when TOF information available, $|n\sigma_{TPC}| < 3$ otherwise
- $|n\sigma_{TPC}| < 2$

The analysis has been repeated with different PID cuts in all its steps, then the three f_0 raw spectra extracted after the fitting procedure, have been corrected for the corresponding efficiency $\times$ acceptance. In Figure 5.2, the ratio between the yields obtained with each of the *non-default* and *default* PID strategies is shown. The systematic uncertainty is assigned as the maximum relative deviation with respect to the *default*. It results below 5% at low p_{T} up to about 9 % at high p_{T}.

Background subtraction. Concerning the procedure used to extract the signal from the distribution of the USP, the background from like-sign pairs has been chosen as

the golden standard for the final analysis. Because of the fact that the LSB was not needed to be normalized to the USP distribution, the analysis presented in this thesis is not affected by any systematic uncertainties due to the normalisation of the background before subtraction from correlated $\pi^+\pi^-$ pairs. On the other hand, the $f_0(980)$ signal extraction has been found to be very challenging because of the large background from other resonance decays in the invariant mass window under study, so the choice of LSB might itself represent a source of systematics and alternative strategies for the estimation of the background should rightfully be considered. MEB is one of these options, however it is very sensitive to the normalisation, as shown in the previous chapter. A more detailed study of the background components is considered out of scope in terms of this work, but, as also explained in the following, the complexity of the invariant mass spectrum of the region of interest significantly affects the estimates of the systematic uncertainties and opens to the next step of the analysis.

Fit function. The f_0 peak was shaped with a relativistic Breit-Wigner. Systematic uncertainty checks have been performed fitting the signal with two different distributions, a non relativistic Breit-Wigner and a Voigtian. After having attempted different fitting configurations, for the final analysis the mass parameter of the Breit-Wigner was fixed to 970 MeV and the width was left free in the range $10 < \Gamma < 100$ MeV. On the other hand, the fit was also performed with a Voigtian distribution, which is a convolution of a Gaussian and a Breit-Wigner and has a third parameter dependency: σ, which is the invariant mass resolution. Its value was fixed to $\sigma = 0.003$ GeV/c^2, from MC simulations. In Figure 5.3, the ratio between the yields obtained with each of the *non-default* and *default* fitting function is reported. The systematic uncertainty on the choice of the function used to perform the signal fit is within 2% - 5%.

Fit parameters and choice of the range. During the fitting procedure the choice of a specific set of constraints on the parameters and range variations can introduce systematic effects. It has been verified, as previously explained, that the fit is very sensitive to the constraints imposed on the mass and width of the resonance. The

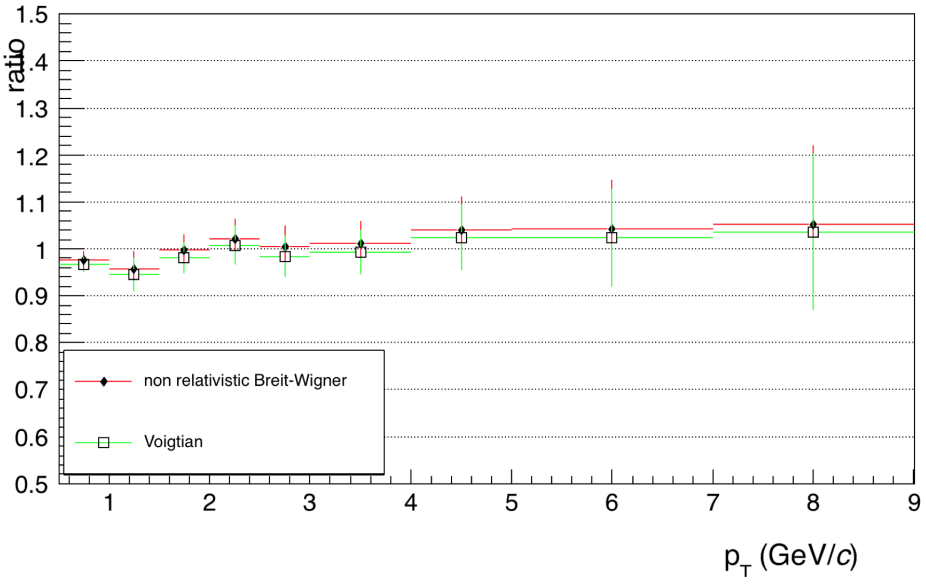

Figure 5.3: Systematic uncertainties due to the variation of the signal fit function using a Breit-Wigner (red) and a Voigtian (green).

following configurations have been used to perform the fit with the relativistic Breit-Wigner and check on the systematics:

- mass and full width fixed: m = 0.97 GeV/c^2 and Γ = 0.03 GeV/c^2 (see Chapter 4).
- mass fixed, m = 0.97 GeV/c^2 , and full width free to vary in the range $0.01 < \Gamma < 0.1$ GeV/c^2 .
- mass fixed, m = 0.97 GeV/c^2 , and full width free to vary in the range $0.01 < \Gamma < 0.01$ GeV/c^2 .
- mass free to vary in the range $0.96 < m < 1.0$ GeV/c^2 and full width fixed (Γ = 0.03 GeV/c^2).

In Figure 5.4, the ratio between the yields obtained with each of the *non-default* relative to *default* fitting parameters configuration is reported. The systematic uncertainty is

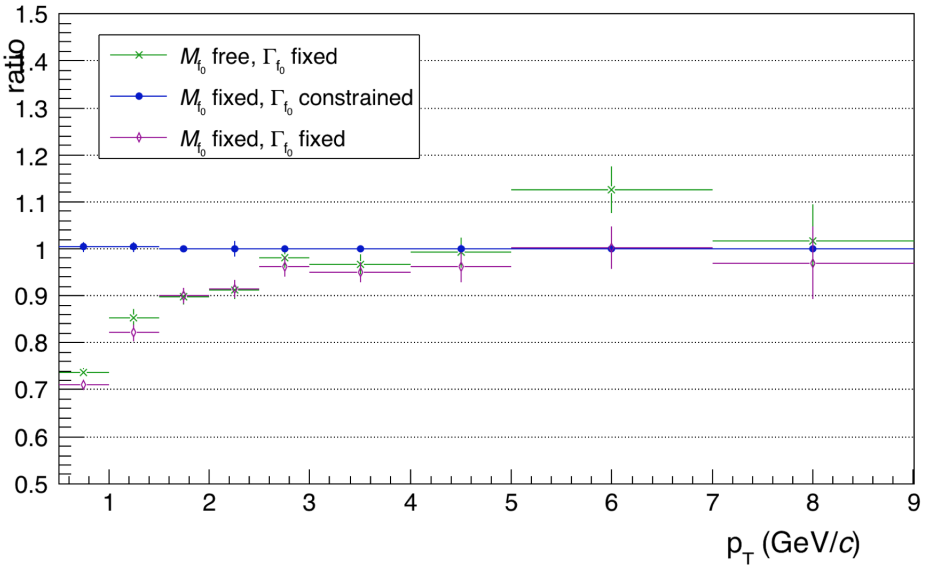

Figure 5.4: Ratios of f0 yields obtained with variations of the fit parameters. Ratios obtained dividing the alternative strategies for the *default* are explicitly labeled.

strongly p_{T}-dependent up to 3 GeV/c from 30% to 10%. Default fit range is 0.86 $<$ $M_{\pi\pi}$ $<$ 1.50 GeV/c^2 . As shown in Figure 5.5, sligthly varying the fit range, first to 0.84-1.48 GeV/c^2 and second to first to 0.88-1.52 GeV/c^2, a systematic uncertainty between up to 20% is introduced. More specifically, getting closer to the $\rho(770)^0$ peak, the systematic uncertainty significantly goes up. These two features suggest to consider the need of including, as it was done for the $f_2(1270)$ peak, the $\rho(770)^0$ in to the fitting procedure. The contribution due to the fit range is the dominant one for the majority of the $\mathrm{p_T}$ bins, as shown in Figure 5.6. Systematics in Figure 5.6 correspond to the total systematic uncertainty which is between up to 30% for the two lowest $\mathrm{p_T}$ bins and about 20% from $\mathrm{p_T}$ = 1.5 GeV/c.

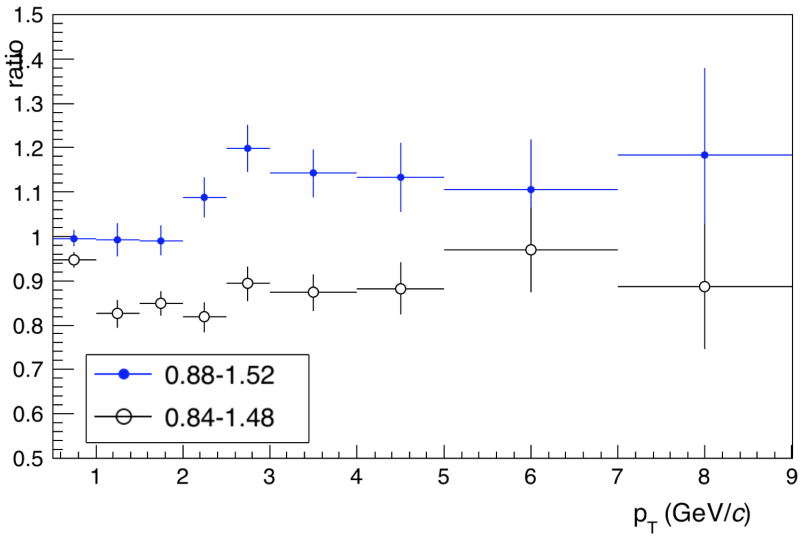

Figure 5.5: Systematic uncertainties due to the variation of the fit range. The default fit range is 0.86< $M_{\pi\pi}$ < 1.50 GeV.

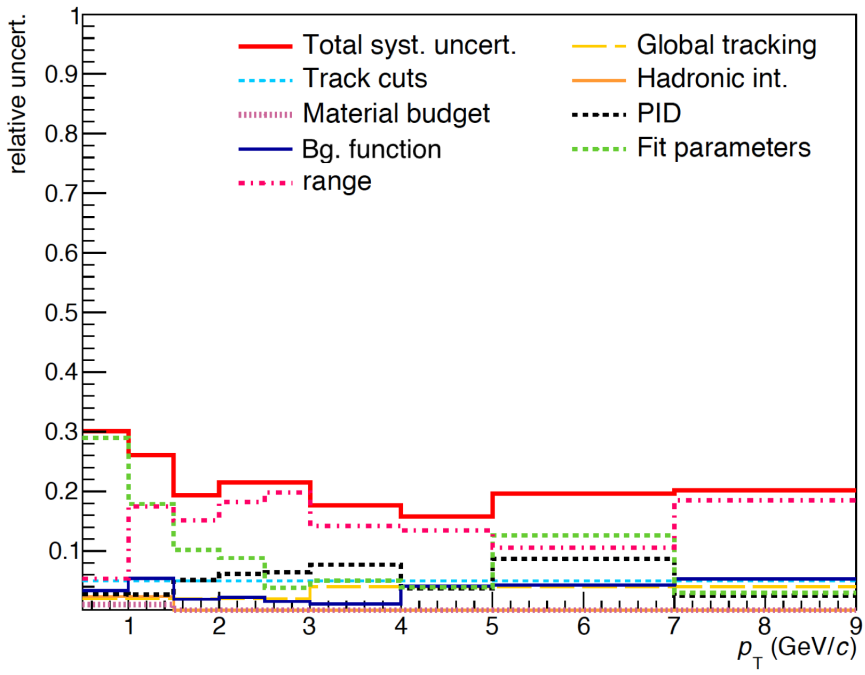

Figure 5.6: Summary of the systematic uncertainty on the yield.

5.2 $f_0(980)$ transverse momentum spectra

The production spectrum of the $f_0(980)$ has been obtained as:

$$\frac{dN_{f_0}}{dp_T} = \frac{1}{2}\frac{1}{N_{evt}}\frac{1}{\Delta y \Delta p_{\mathrm{T}}}\frac{N_{f_0(p_{\mathrm{T}})}}{(Acc \times \epsilon_r ec)(p_{\mathrm{T}}) \cdot B.R.} f_{norm} \tag{5.1}$$

After the corrections for efficiency reconstruction and detector acceptance $(Acc \times \epsilon)(p_{\mathrm{T}})$, (see Chapter 4), the raw yield in each p_{T} bin $(N_{f_0}(p_T))$ has been normalised dividing it by the number of the total accepted events (N_{evt}). A correction for the branching ratio (B.R.) has also to be taken into account and since the PDG [7] reports a dominant decay of f_0 into $\pi\pi$, here a B.R. = 100% has been assumed. It has to be noted that in order to normalize the yield to the number of inelastic pp collisions, an inelastic normalization factor (f_{norm}) is needed to correct for vertex and trigger efficiency for pp. This factor converts the particle yield normalized to the number of triggered events to a yield normalized to the number of inelastic events. The inelastic normalization factor is the ratio of the V0 visible cross section to the inelastic cross section. For pp collisions at the centre-of-mass energy of 5.02 TeV, $f_{norm} = 0.7574 \pm 0.0190$ [95, 96]. In order to extrapolate the yield in the low momentum region not available for the direct measurements, a Levy-Tsallis fit has been performed according to [97]:

$$\frac{1}{p_T}\frac{dN}{dp_T dy} = \frac{dN}{dy}\frac{(n-1)(n-2)}{nT[nT + m(n-2)]}\Big(1 + \frac{\sqrt{p_T^2 + m^2} - m}{nT}\Big)^{-n} \tag{5.2}$$

with T, n and the dN/dy as fit parameters and m the mass of the particle under study. The transverse momentum spectrum is fitted between 0 to 9.0 GeV/c, namely in the range of available data points, as shown in Figure 5.7. The integrated yield is calculated by integrating the spectrum in the measured range and the fitted function in the extrapolation range. Since the measurement goes down to $p_T = 0.5$ GeV/c, the extrapolation of the spectrum constitute a source of systematic uncertainty for the final result. This will be addressed in future phases of the analysis by using different functions to extrapolate the low p_T. The contribution coming from systematic uncertainties associated to the measured spectrum is propagated to dN/dy by refitting the data while randomly sam-

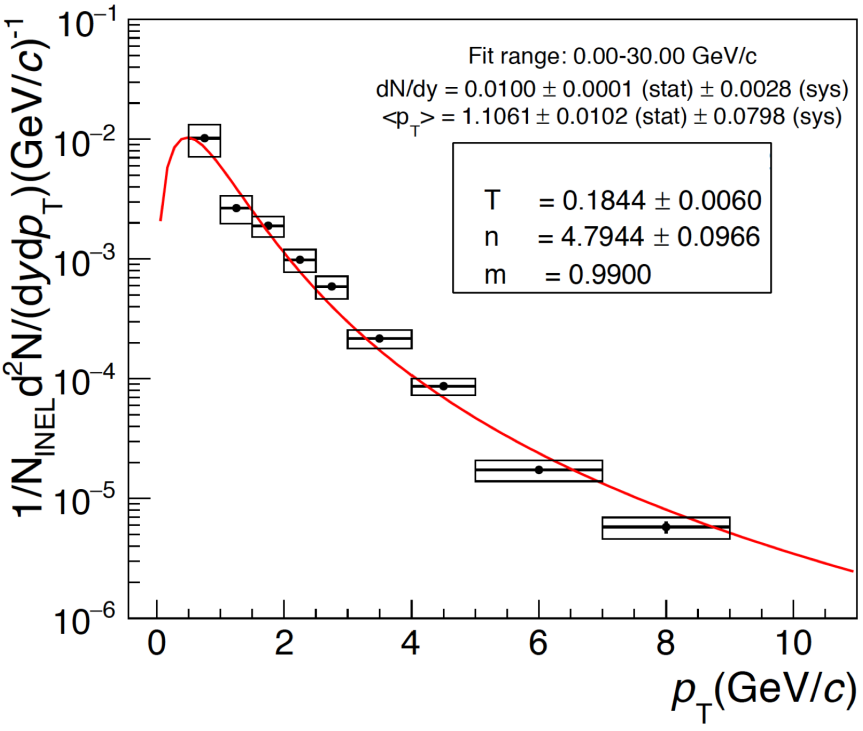

Figure 5.7: Production spectrum of the $f_0(980)$ measured with ALICE at mid-rapidity ($|y| < 0.5$) in pp collisions at $\sqrt{s} = 5.02$ TeV. The spectrum is fitted with a Levy–Tsallis function.

pling the range of each measured point within its systematic uncertainty. The results of the yield and average momentum are the following:

$$\frac{dN}{dy} = 0.0100 \pm 0.0001 \text{ (stat.)} \pm 0.0028 \text{ (sys.)}$$
$$\langle p_{\mathrm{T}} \rangle = 1.11 \pm 0.01 \text{ (stat.)} \pm 0.08 \text{ (sys.)}$$

As soon as pion, kaon, proton, K^* and ϕ spectra, in pp collisions at $\sqrt{s} = 5.02$ TeV measured by the ALICE collaboration will be available, the f_0 production will be compared with production yields of other resonances and stable hadrons and with the theoretical models.

Conclusions

The aim of this thesis project was to study the $f_0(980) \rightarrow \pi^+\pi^-$ production in pp collisions at $\sqrt{s} = 5.02$ TeV. The highlight of the work can be summarised with the results obtained for the p_{T}-integrated yield and average momentum of the $f_0(980)$, which are:

$$\frac{dN}{dy} = 0.0100 \pm 0.0001 \text{ (stat.) } \pm 0.0028 \text{ (sys.)}$$
$$\langle p_{\mathrm{T}} \rangle = 1.11 \pm 0.01 \text{ (stat.) } \pm 0.08 \text{ (sys.)}$$

As extensively discussed in this work, the study of the shape of the background suggests a complex scenario which opens to the next step of the analysis. In particular, the $\rho(770)^0$ peak should be included into the fitting procedures in order to describe more accurately the $\pi\pi$ invariant mass spectrum of the region of interest. As already noted, a more detailed study of the background components with a resonance *cocktail* was considered out of scope in terms of this work, but it seems to be unavoidable. Improvements in the signal extraction procedure are foreseen in order to reduce systematic uncertainties, that are presently dominating the precision on the measurement. In the near future, the analysis presented here will be extended to a four-times larger sample of pp collisions at $\sqrt{s} = 5.02$ TeV collected by ALICE at the end of 2017. The results for f_0 will then be compared to the production of other light-flavor hadrons and resonances, as well to models. In a longer term, the study will be extended to high multiplicity events (p-Pb, Pb-Pb). Theoretical input will be functional to better understand the observables of interest in other collision systems.

Bibliography

[1] R. K. Ellis, W. J. Stirling, and B. R. Webber, *QCD and collider physics*. Cambridge University Press, 2003.

[2] J. Letessier and J. Rafelski, *Hadrons and Quark Gluon Plasma; new ed.* Cambridge University Press, 2005.

[3] F. Halzen and A. D. Martin, *Quarks and Leptons: an introductory course in Modern Particle Physics* . New York, Usa: Wiley (1984), 1984.

[4] P. Skands, "Introduction to QCD," in *Proceedings, Theoretical Advanced Study Institute in Elementary Particle Physics: Searching for New Physics at Small and Large Scales (TASI 2012): Boulder, Colorado, June 4-29, 2012*, pp. 341–420, 2013.

[5] D. J. Gross and F. Wilczek, "Ultraviolet Behavior of Nonabelian Gauge Theories," *Phys. Rev. Lett.*, vol. 30, pp. 1343–1346, 1973.

[6] F. Wilczek, "Nobel Lecture: Asymptotic freedom: From paradox to paradigm," *Proc. Nat. Acad. Sci.*, vol. 102, pp. 8403–8413, 2005. [Rev. Mod. Phys.77,857(2005)].

[7] e. a. Patrignani, "Review of Particle Physics," *Chin. Phys.*, vol. C40, no. 10, p. 100001, 2016.

[8] K. G. Wilson, "Confinement of quarks," *Phys. Rev. D*, vol. 10, pp. 2445–2459, Oct 1974.

[9] L. J. Hashimoto S. and S. Sharpe, "Lattice quantum chromodynamics - review on, particle data group," 2015.

[10] S. Durr *et al.*, "Ab-Initio Determination of Light Hadron Masses," *Science*, vol. 322, pp. 1224–1227, 2008.

[11] P. Braun-Munzinger, V. Koch, T. Schäfer, and J. Stachel, "Properties of hot and dense matter from relativistic heavy ion collisions," *Phys. Rept.*, vol. 621, pp. 76–126, 2016.

[12] A. Bazavov, T. Bhattacharya, C. DeTar, H.-T. Ding, S. Gottlieb, R. Gupta, P. Hegde, U. M. Heller, F. Karsch, E. Laermann, L. Levkova, S. Mukherjee, P. Petreczky, C. Schmidt, C. Schroeder, R. A. Soltz, W. Soeldner, R. Sugar, M. Wagner, and P. Vranas, "Equation of state in $(2 + 1)$-flavor qcd," *Phys. Rev. D*, vol. 90, p. 094503, Nov 2014.

[13] U. W. Heinz, "Towards the Little Bang Standard Model," *J. Phys. Conf. Ser.*, vol. 455, p. 012044, 2013.

[14] J. D. Bjorken, "Highly Relativistic Nucleus-Nucleus Collisions: The Central Rapidity Region," *Phys. Rev.*, vol. D27, pp. 140–151, 1983.

[15] E. Wang and X.-N. Wang, "Jet tomography of hot and cold nuclear matter," *Phys. Rev. Lett.*, vol. 89, p. 162301, Oct 2002.

[16] A. et al., "Production of charged pions, kaons and protons at large transverse momenta in pp and Pb–Pb collisions at $\sqrt{s_{NN}} = 2.76$ TeV," *Phys. Lett.*, vol. B736, pp. 196–207, 2014.

[17] J. e. a. Adam, "Measurement of jet quenching with semi-inclusive hadron-jet distributions in central Pb-Pb collisions at $\sqrt{s_{\mathrm{NN}}} = 2.76$ TeV," *JHEP*, vol. 09, p. 170, 2015.

[18] T. Matsui and H. Satz, "J/ψ Suppression by Quark-Gluon Plasma Formation," *Phys. Lett.*, vol. B178, pp. 416–422, 1986.

[19] M. e. a. Abreu, "Evidence for deconfinement of quarks and gluons from the J/psi suppression pattern measured in Pb-Pb collisions at the CERN-SPS," *Physics Letters B*, vol. 477, pp. 28–36, 2000. NA50.

[20] J. Rafelski and B. Muller, "Strangeness Production in the Quark - Gluon Plasma," *Phys. Rev. Lett.*, vol. 48, p. 1066, 1982. [Erratum: Phys. Rev. Lett.56,2334(1986)].

[21] M. L. Miller, K. Reygers, S. J. Sanders, and P. Steinberg, "Glauber modeling in high energy nuclear collisions," *Ann. Rev. Nucl. Part. Sci.*, vol. 57, pp. 205–243, 2007.

[22] A. et al., "Enhanced production of multi-strange hadrons in high-multiplicity proton-proton collisions," *Nature Phys.*, vol. 13, pp. 535–539, 2017.

[23] A. et al., "Observation of Long-Range Elliptic Azimuthal Anisotropies in $\sqrt{s}$ =13 and 2.76 TeV *pp* Collisions with the ATLAS Detector," *Phys. Rev. Lett.*, vol. 116, no. 17, p. 172301, 2016.

[24] K. et al., "Observation of Long-Range Near-Side Angular Correlations in Proton-Proton Collisions at the LHC," *JHEP*, vol. 09, p. 091, 2010.

[25] K. et al., "Measurement of long-range near-side two-particle angular correlations in pp collisions at $\sqrt{s}$ =13 TeV," *Phys. Rev. Lett.*, vol. 116, no. 17, p. 172302, 2016.

[26] A. et al., "Long-range angular correlations on the near and away side in p-Pb collisions at $\sqrt{s_{NN}} = 5.02$ TeV," *Phys. Lett.*, vol. B719, pp. 29–41, 2013.

[27] A. et al., "Harmonic decomposition of two-particle angular correlations in Pb-Pb collisions at $\sqrt{s_{NN}} = 2.76$ TeV," *Phys. Lett.*, vol. B708, pp. 249–264, 2012.

[28] A. et al., "Multiplicity dependence of the average transverse momentum in pp, p-Pb, and Pb-Pb collisions at the LHC," *Phys. Lett.*, vol. B727, pp. 371–380, 2013.

[29] A. et al., "J/*psi* production as a function of charged particle multiplicity in pp collisions at s =7 tev," *Physics Letters B*, vol. 712, no. 3, pp. 165 – 175, 2012.

[30] L. R. Evans and P. Bryant, "LHC Machine," *JINST*, vol. 3, p. S08001. 164 p, 2008. This report is an abridged version of the LHC Design Report (CERN-2004-003).

[31] "ALICE: Technical proposal for a large ion collider experiment at the CERN LHC," 1995.

[32] *ATLAS: technical proposal for a general-purpose pp experiment at the Large Hadron Collider at CERN*. LHC Tech. Proposal, Geneva: CERN, 1994.

[33] *Technical proposal*. LHC Tech. Proposal, Geneva: CERN, 1994. Cover title : CMS, the Compact Muon Solenoid : technical proposal.

[34] *LHCb : Technical Proposal*. Tech. Proposal, Geneva: CERN, 1998.

[35] "The accelerator complex," Jan 2012.

[36] "LHC Commissioning with beam,"

[37] M. Solfaroli Camillocci, "LHC Performance Workshop 2018,"

[38] M. E. Beddo *et al.*, "STAR: Conceptual design report for the Solenoidal Tracker at RHIC," 1992.

[39] J. C. Gregory *et al.*, "PHENIX: Preliminary conceptual design report," 1992.

[40] T. W. Ludlam, "RHIC and Quark Matter: a proposed heavy ion collider at Brookhaven National Laboratory," in *Quark Matter '84. Proceedings.*, p. 0240, 1984.

[41] K. e. a. Aamodt, "The ALICE experiment at the CERN LHC," *JINST*, vol. 3, 2008.

[42] D. Miskowiec, "Performance of the alice experiment during the lhc run 1," vol. 2014-1, p. 65 p., 2014.

[43] B. Abelev *et al.*, "Upgrade of the ALICE Experiment: Letter Of Intent," *J. Phys.*, vol. G41, 2014.

[44] "CERN Document Server,"

[45] B. e. a. Abelev, "Technical Design Report for the Upgrade of the ALICE Inner Tracking System," Tech. Rep. CERN-LHCC-2013-024. ALICE-TDR-017, Nov 2013.

[46] W. R. Leo, *Techniques for Nuclear and Particle Physics Experiments: A How to Approach*. 1994.

[47] C. Lippmann, "Upgrade of the ALICE Time Projection Chamber," 2014.

[48] A. Akindinov *et al.*, "Performance of the ALICE Time-Of-Flight detector at the LHC," *Eur. Phys. J. Plus*, vol. 128, p. 44, 2013.

[49] E. Abbas *et al.*, "Performance of the ALICE VZERO system," *JINST*, vol. 8, p. P10016, 2013.

[50] J. e. a. Adam, "Determination of the event collision time with the ALICE detector at the LHC," *Eur. Phys. J. Plus*, vol. 132, no. 2, p. 99, 2017.

[51] P. Cortese, F. Carminati, C. W. Fabjan, L. Riccati, and H. de Groot, *ALICE computing: Technical Design Report*. Technical Design Report ALICE, Geneva: CERN, 2005. Submitted on 15 Jun 2005.

[52] R. Brun and F. Rademakers, "ROOT: An object oriented data analysis framework," *Nucl. Instrum. Meth.*, vol. A389, pp. 81–86, 1997.

[53] X.-N. Wang and M. Gyulassy, "HIJING: A Monte Carlo model for multiple jet production in p p, p A and A A collisions," *Phys. Rev.*, vol. D44, pp. 3501–3516, 1991.

[54] S. Roesler, R. Engel, and J. Ranft, "The Monte Carlo event generator DPMJET-III," in *Advanced Monte Carlo for radiation physics, particle transport simulation*

and applications. Proceedings, Conference, MC2000, Lisbon, Portugal, October 23-26, 2000, 2000.

[55] T. Sjostrand, S. Mrenna, and P. Z. Skands, "PYTHIA 6.4 Physics and Manual," *JHEP*, vol. 05, p. 026, 2006.

[56] S. Agostinelli *et al.*, "GEANT4: A Simulation toolkit," *Nucl. Instrum. Meth.*, vol. A506, pp. 250–303, 2003.

[57] R. Fruhwirth, "Application of Kalman filtering to track and vertex fitting," *Nucl. Instrum. Meth.*, vol. A262, pp. 444–450, 1987.

[58] B. B. Abelev *et al.*, "Performance of the ALICE Experiment at the CERN LHC," *Int. J. Mod. Phys.*, vol. A29, 2014.

[59] C. Markert and A. Collaboration, "Hadronic resonance production in alice," *Journal of Physics: Conference Series*, vol. 878, no. 1, p. 012003, 2017.

[60] M. Bleicher *et al.*, "Relativistic hadron hadron collisions in the ultrarelativistic quantum molecular dynamics model," *J. Phys.*, vol. G25, pp. 1859–1896, 1999.

[61] E. Fermi, "High energy nuclear events," *Progress of Theoretical Physics*, vol. 5, no. 4, pp. 570–583, 1950.

[62] A. Andronic, P. Braun-Munzinger, K. Redlich, and J. Stachel, "Decoding the phase structure of QCD via particle production at high energy," 2017.

[63] P. Braun-Munzinger, K. Redlich, and J. Stachel, "Particle production in heavy ion collisions," 2003.

[64] J. Cleymans and H. Satz, "Thermal hadron production in high-energy heavy ion collisions," *Z. Phys.*, vol. C57, pp. 135–148, 1993.

[65] S. A. Bass *et al.*, "Microscopic models for ultrarelativistic heavy ion collisions," *Prog. Part. Nucl. Phys.*, vol. 41, pp. 255–369, 1998. [Prog. Part. Nucl. Phys.41,225(1998)].

[66] H. Petersen, J. Steinheimer, G. Burau, M. Bleicher, and H. Stöcker, "Fully integrated transport approach to heavy ion reactions with an intermediate hydrodynamic stage," *Phys. Rev. C*, vol. 78, p. 044901, Oct 2008.

[67] Steinheimer, J. and Bleicher, M., "Hadron resonance production and final state hadronic interactions with urqmd at lhc," *EPJ Web of Conferences*, vol. 97, p. 00026, 2015.

[68] Steinheimer, J., Vovchenko, V., Aichelin, J., Bleicher, M., and Stöcker, H., "Final state hadronic rescattering with urqmd," *EPJ Web Conf.*, vol. 171, p. 05003, 2018.

[69] C. Markert, "Resonance production in heavy ion collisions," *J. Phys.*, vol. G31, pp. S897–S902, 2005.

[70] J. Adam *et al.*, "$K^*(892)^0$ and $\phi(1020)$ meson production at high transverse momentum in pp and Pb-Pb collisions at $\sqrt{s_{NN}} = 2.76$ TeV," *Phys. Rev.*, vol. C95, no. 6, p. 064606, 2017.

[71] "Note on scalar mesons below 2GeV,"

[72] I. Bediaga, F. S. Navarra, and M. Nielsen, "The Structure of f0(980) from charmed mesons decays," *Phys. Lett.*, vol. B579, pp. 59–66, 2004.

[73] J. Vijande, A. Valcarce, F. Fernandez, and B. Silvestre-Brac, "Nature of the light scalar mesons," *Phys. Rev.*, vol. D72, p. 034025, 2005.

[74] R. L. Jaffe, "Multi-Quark Hadrons. 1. The Phenomenology of (2 Quark 2 anti-Quark) Mesons," *Phys. Rev.*, vol. D15, p. 267, 1977.

[75] S. L. Olsen, "News from BESIII," *PoS*, vol. BORMIO2017, p. 038, 2017.

[76] N. N. Achasov, "Analysis of nature of phi —¿ gamma pi eta and phi —¿ gamma pi0 pi0 decays," *AIP Conf. Proc.*, vol. 619, pp. 112–121, 2002. [,112(2001)].

[77] G. 't Hooft, G. Isidori, L. Maiani, A. Polosa, and V. Riquer, "A theory of scalar mesons," *Physics Letters B*, vol. 662, no. 5, pp. 424 – 430, 2008.

[78] K. Ahmet *et al.*, "The OPAL detector at LEP," *Nucl. Instrum. Meth.*, vol. A305, pp. 275–319, 1991.

[79] "LEP Design Report: Vol.2. The LEP Main Ring," 1984.

[80] K. Ackerstaff *et al.*, "Production of f(0)(980), f(2)(1270) and phi(1020) in hadronic Z0 decay," *Eur. Phys. J.*, vol. C4, pp. 19–28, 1998.

[81] S. M. Flatté, "Coupled-channel analysis of the $\pi\eta$ and KKsystems near KK threshold," *Physics Letters B*, vol. 63, pp. 224–227, July 1976.

[82] V. Baru, J. Haidenbauer, C. Hanhart, Y. Kalashnikova, and A. Kudryavtsev, "Evidence that the a0(980) and f0(980) are not elementary particles," *Physics Letters B*, vol. 586, no. 1, pp. 53 – 61, 2004.

[83] P. Fachini, "rho(770)0 and f(0)(980) production in Au+Au and pp collisions at S(NN)**(1/2) = 200-GeV," *J. Phys.*, vol. G30, pp. S565–S570, 2004.

[84] E. Shuryak and G. Brown, "Matter-induced modification of resonances at rhic freeze-out," *Nuclear Physics A*, vol. 717, no. 3, pp. 322 – 335, 2003.

[85] R. e. a. Aaij, "Measurement of the resonant and CP components in $\overline{B}^0 \to J/\psi\pi^+\pi^-$ decays," *Phys. Rev.*, vol. D90, no. 1, p. 012003, 2014.

[86] D. Barberis *et al.*, "A Partial wave analysis of the centrally produced pi+ pi- system in p p interactions at 450-GeV/c," *Phys. Lett.*, vol. B453, pp. 316–324, 1999.

[87] M. e. a. Battaglieri, "Measurement of direct $f_0(980)$ photoproduction on the proton," *Phys. Rev. Lett.*, vol. 102, p. 102001, Mar 2009.

[88] C. Grupen and B. Schwartz, *Particle detectors*. 2008.

[89] B. B. Abelev *et al.*, "Performance of the ALICE Experiment at the CERN LHC," *Int. J. Mod. Phys.*, vol. A29, p. 1430044, 2014.

[90] W. Verkerke and D. P. Kirkby, "The RooFit toolkit for data modeling," *eConf*, vol. C0303241, p. MOLT007, 2003. [,186(2003)].

[91] P. Skands, S. Carrazza, and J. Rojo, "Tuning PYTHIA 8.1: the Monash 2013 Tune," *Eur. Phys. J.*, vol. C74, no. 8, p. 3024, 2014.

[92] R. Brun, F. Bruyant, F. Carminati, S. Giani, M. Maire, A. McPherson, G. Patrick, and L. Urban, "GEANT Detector Description and Simulation Tool," 1994.

[93] S. Acharya *et al.*, "Transverse momentum spectra and nuclear modification factors of charged particles in pp, p-Pb and Pb-Pb collisions at the LHC," 2018.

[94] J. e. a. Adam, "Measurement of pion, kaon and proton production in proton–proton collisions at $\sqrt{s} = 7$ tev," *The European Physical Journal C*, vol. 75, p. 226, May 2015.

[95] C. Loizides, J. Kamin, and D. d'Enterria, "Precision Monte Carlo Glauber predictions at present and future nuclear colliders," 2017.

[96] "ALICE luminosity determination for pp collisions at $\sqrt{s} = 5$ TeV," Jul 2016.

[97] C. Tsallis, "Possible Generalization of Boltzmann-Gibbs Statistics," *J. Statist. Phys.*, vol. 52, pp. 479–487, 1988.